Syracuse University

SURFACE

Dissertations - ALL

SURFACE

January 2015

Mechanics, shape, and programmability in soft matter systems: From fluid membranes to spring and droplet networks

Tao Zhang
Syracuse University

Follow this and additional works at: https://surface.syr.edu/etd

Part of the Physical Sciences and Mathematics Commons

Recommended Citation

Zhang, Tao, "Mechanics, shape, and programmability in soft matter systems: From fluid membranes to spring and droplet networks" (2015). *Dissertations - ALL*. 337.
https://surface.syr.edu/etd/337

This Dissertation is brought to you for free and open access by the SURFACE at SURFACE. It has been accepted for inclusion in Dissertations - ALL by an authorized administrator of SURFACE. For more information, please contact surface@syr.edu.

Abstract

This thesis analyzes three different soft matter systems—membranes, polymers, and droplets—to answer questions about shape, mechanics, and programmability. For membranes, my collaborators and I have developed a theoretical model of endocytosis in yeast. Endocytosis is the process by which a cell membrane deforms to surround extracellular material to draw it into the cell. Endocytosis in yeast involves clathrin, actin, and Bar proteins. Our model breaks up the process into three stages: (i) initiation, where clathrin interacts with the cell membrane via adaptor proteins, (ii) elongation, where the membrane is then further deformed by polymerizing actin filaments, followed by (iii) pinch-off. Our results suggest that the pinch-off mechanism may be assisted by a pearling-like instability. In addition, we potentially rule out two of the three competing models for the organization of the actin filament network during the elongation stage. For polymers, the actin cytoskeleton network at the leading edge of the cell becomes anisotropic with filament alignment favoring the direction of motion of the cell. To begin to capture the mechanics of this anisotropic filament network, my collaborators and I have constructed an effective medium (mean field) theory of an anisotropic, disordered spring network. We find that increasing the anisotropy increases the filament density required for a nonzero shear modulus (rigidity). We also conduct numerical simulations and find good agreement with the effective medium theory. We then extend our analysis to include the mechanics of coupled disordered spring networks to study force transmission between the actin cytoskeletal network and DNA via the lamin filament network and potentially begin to establish a microscopic basis for the mechanical regulation of transcription via the actin cytoskeleton. For droplets, we study numerically a collection of aqueous droplets joined by single lipid bilayers to form a cohesive, tissue-like material. The droplets in these droplet networks can be programmed with different osmolarity gradients. These osmolarity gradients generate internal stresses via local flows and the network then folds into designed structures. In other words, global change is driven by local osmolarity gradients. Using molecular dynamics simulations, we study the formation of shapes ranging from rings to spirals to tetrahedra and determining the optimal range of parameters for such structures. By adding an osmotic interaction with a dynamic environment, a folding-unfolding process can also be realized. This latter result is a step towards osmotic robotics.

Mechanics, shape, and programmability in soft matter systems: From fluid membranes to spring and droplet networks

by

Tao Zhang

B.S., USTC, 2010

Dissertation
Submitted in partial fulfillment of the requirements for the degree of
Doctor of Philosophy in Physics

Syracuse University
August 2015

Copyright © Tao Zhang 2015
All Rights Reserved

Acknowledgements

I would like to express my most sincere gratitude to my advisor Prof. Jen Schwarz for her continuous support of my Ph.D. study. I would also like to sincerely thank Prof. Mark Bowick who has essentially served as a co-advisor over the past several years even though it was never formalized in writing. Their kindly guidance helped me in my research and the construction of this thesis. I also appreciate the help from all the other professors with whom I have studied and worked with. A special thanks goes to Prof. Moumita Das, who has significant contribution on Chapter 3 and taught me a lot about using Mathematica. Another thanks goes to Prof. Rastko Sknepnek for his valuable contribution to Chapter 2 and help on improving my coding skills. I owe my gratitude to Prof. M. C. Marchetti for her useful comments on Chapter 5 and Prof. J. Guven for helpful discussion on Chapter 2. I also want to thank David Quint, whose initial simulation code led to the work in Chapter 3, Prof. Xiaoming Mao and Dr. D. Zeb Rocklin for helpful discussion on Chapter 4, and Duanduan Wan, whose work enriches Chapter 5. I would like to thank all of my thesis committee members for their valuable time. I acknowledge support from the Soft Matter Program at Syracuse University.

Dedicated to my parents, relatives and friends.

Contents

Abstract **i**

Acknowledgements **iv**

List of Figures **viii**

List of Tables **xii**

1 Introduction **1**
- 1.1 Fluid membranes . . . 2
- 1.2 Polymers and disordered spring networks . . . 6
- 1.3 Droplet networks . . . 13
  - 1.3.1 Bayley group's experiment . . . 13

2 Endocytosis in yeast **16**
- 2.1 Motivation . . . 16
- 2.2 Model and methods . . . 19
  - 2.2.1 Initiation stage . . . 20
  - 2.2.2 Elongation stage . . . 20
- 2.3 Results . . . 23
  - 2.3.1 Initiation stage with clathrin . . . 23
  - 2.3.2 Elongation stage via actin polymerization . . . 27
  - 2.3.3 Pinch-off stage via the pearling instability . . . 31
- 2.4 Discussion and conclusion . . . 34

3 Mechanics of anisotropic spring networks **36**
- 3.1 Motivation . . . 36
- 3.2 Model . . . 37
- 3.3 Methods and Analysis . . . 38
  - 3.3.1 Constraint counting argument and the rigidity threshold . . . 38
  - 3.3.2 Effective Medium Theory . . . 39
  - 3.3.3 Numerical Simulations . . . 42
- 3.4 Results . . . 43
- 3.5 Discussion . . . 50

4 Coupled spring networks **53**
4.1 Introduction . . . 53
4.2 Model and Methods . . . 56
4.3 Results . . . 57
    4.3.1 Decoupled limit . . . 57
    4.3.2 One coupled limit . . . 59
4.4 Discussion . . . 60

5 Shape-shifting droplet networks **62**
5.1 Motivation . . . 62
5.2 Model . . . 63
5.3 Methods and results . . . 65
    5.3.1 Rings . . . 65
    5.3.2 Spirals . . . 70
    5.3.3 Tetrahedra . . . 70
    5.3.4 Reversible Folding . . . 71
5.4 Discussion . . . 74

A Effective medium theory **75**

B Conjugate gradient method **78**
B.1 The quadratic Form . . . 78
B.2 Line search methods . . . 79
    B.2.1 Steepest descent method . . . 79
    B.2.2 Conjugate gradient method . . . 79

C Metropolis Monte Carlo method **82**

D Details of variational calculation for initiation stage in the Monge representation **83**

E Pearling instability analysis **87**

Bibliography **90**

List of Figures

1.1 Roadmap for the thesis. 2
1.2 Biological roadmap 3
1.3 Schematic of the lipid bilayer, with hydrophilic heads exposed and hydrophobic tails sequestered 3
1.4 Schematic for the membrane curvature, showing the principal curvature radii R_1 and R_2. 4
1.5 Schematic of endocytosis in mammalian cells. Figure taken from website: www.abcam.com from an article by Dr. Tony Jackson. 6
1.6 Structure of an actin filament showing the barbed (or plus) and pointed (or minus) ends [14] 6
1.7 Schematic of a disordered spring network. 7
1.8 Elastic constants C_{11} (bulk modulus) and C_{44} (shear modulus) averaged over three configurations for a 440 atom triangular network. Both constants are in units of the spring constant and the lattice spacing. The straight lines denote the effective-medium theory results. Figure taken from Ref. [18]. 9
1.9 Deformed configuration a compositely crosslinked semiflexible filament network with 2.7 percent strain. The bond occupation probability is $p = 0.64$, and angle-constraining crosslinker occupation probability is $p_{nc} = 0.15$. The purple lines denote semiflexible filaments, the red arcs denote angle-constraining crosslinkers, the black circles represent nodes where all crossing filaments are free to rotate around that node, while the grey circles denote nodes where some of the crossing filaments are free to rotate around that node. The absence of a black or grey circle denotes a node where no free rotations are possible. The filament bending stiffness relative to stretching stiffness $\kappa_c/\alpha = 10^{-6}$ and the stiffness of angular crosslinkers relative to stretching stiffness $\kappa_{nc}/\alpha = 10^{-6}$. [20] 10
1.10 The shear modulus G, normalized by its value for the corresponding undiluted network G_0, as a function of occupation probability $p = p_{ij}$. The data points are numerical results and the solid lines, the effective medium theory results [20]. 11
1.11 Schematic of cell crawling by extension of the lamellipodium via actin polymerization. [21] 12
1.12 A, Electron micrograph of a cell showing a dense branched network of integrated actin filaments. B, Smaller scale image of dendritic branches of actin filaments. [22] 12
1.13 Structure of LINC complexes. ABD: Actin-binding domain; INM: Inner Nuclear Membrane; ONM: Outer Nuclear Membrane. [25] 13

1.14 Schematic image showing droplets of different aqueous solutions printed into a solution of lipids in oil. The droplets acquire a lipid monolayer and form bilayers with droplets in the developing network. [32] 14
1.15 Photographs of a rectangular network folding into a circle over 3 hours. The orange and blue droplets initially contained 250 mM KCl and 16 mM KCl, respectively. Scale bar, 250 mm [32] 15
1.16 (A) Photographs of a flowershaped network folding spontaneously into a hollow sphere. The orange and blue droplets initially contained 80 mM KCl and 8 mM KCl, respectively. The photographs cover a period of 8 hours. Scale bar, 200 mm. (B) Frames from a folding simulation of a network with a similar initial geometry to the network in (A). Blue and red represent the lowest and highest initial osmolarities, respectively, and white indicates the average of the two. [32] 15

2.1 An electron micrograph image of a deformed membrane during endocytosis in S. cerevisiae. The image is reprinted with permission from [39]. The scale bar is 100 nm. 17
2.2 Schematic for endocytosis in yeast using Proposal 1 for the actin filament organization: (a) Clathrin (purple) attaches to the membrane (black-/blue) via proteins Sla1 and Ent1/2 (not depicted here) and the protein Sla2 (green/brown) is recruited near the clathrin. (b) Actin (red) attaches to the membrane near the edge of the clathrin "bowl" via Sla2 and lengthens due to polymerization to initiate tube formation. (c) Actin continues to polymerize and lengthen the tube. (d) BAR proteins (orange) become prominent and surround part of the tube (and the actin). The grey arrows denote the direction of the actin force on the membrane. Note that potential additional actin filaments rooted in the surrounding cytoskeleton and extending towards the invagination site not been drawn. 18
2.3 (a) Schematic depicts Proposal 2, where the actin filaments are tethered to the rest of the cytoskeleton, as denoted by the two black Xs, and polymerize inward towards the invagination site. (b) Schematic represents Proposal 3, where there are two local anchoring regions such that two actin networks form to drive tube formation. The grey arrows, again, denote the direction of the actin force on the membrane. 18
2.4 (a) Cell membrane profile, or $z(x, y = 0)$, for the parameters stated in the text. The red (medium grey) denotes the clathrin-bound part of the membrane, while the blue (dark grey) denotes the bare membrane. (b) Top view of the two-component membrane model using simulated annealing Monte Carlo methods. (c) Side view of the same configuration. Both images have been rescaled accordingly for presentation purposes. (d) Comparison of the maximum depth (or depth) obtained from the numerical simulation (symbols) with the analytical solution (line) for the intiation stage. All the parameters, except for the varying C_{01}, are the same as the $\kappa_G = 0$ curve in Fig. 2.4a. 25

2.5 (a) Simulation results for Model 1 with total applied force $F_t = 10\ pN$. The total force is applied to only the yellow (light grey) part of the membrane (at the vertices). Red (medium grey) denotes the Sla1/Ent1/2 bound part of the membrane and blue (dark grey) denotes the bare membrane. (b) Same as (a) except with $F_t = 50\ pN$; (c) Comparison of the depth as a function of F_t for three different models with zero and nonzero turgor pressure, p. Again, the error bar is of order the symbol size. The arrow pointing downward denotes the value of F_{eq} for reference 31
2.6 The pearling instability for a cylindrical membrane with increasing surface tension going from left to right, or $\sigma R_o^2/\kappa = 0.267, 2.67$, and 4.15 respectively. The top and red part of the tube are fixed. 33

3.1 Schematic figure showing the randomly diluted anisotropic spring network with corresponding occupation probabilities p_x and p_y. 38
3.2 Plot of the phase diagram according to mean field constraint counting argument, with the inset showing the shear modulus G as a function of p_x and p_y obtained from the EMT in units of γ (set to unity) and the horizontal lattice spacing (set to unity). Different lattice realizations are also shown. 40
3.3 The shear modulus G as a function of p_y for different p_x as shown in the legend. The open symbols show data from the simulations and the filled symbols (joined by solid lines in the inset) represent the result from the effective medium theory. The inset shows the same data on a log-linear scale. The system size in the simulation is $N_x = N_y = 128$. 45
3.4 Shear modulus G (for shear applied via the x boundaries) as a function of p_y at fixed $p_x = 0.5$ and for different system sizes (as shown in legend). 46
3.5 The area bulk modulus K as a function of p_y for different p_x as shown in the legend in units of the bare spring constant γ (set to unity). The open symbols show data from the simulations and the filled symbols (joined by solid lines in the inset) represent the results from the effective medium theory. The system size in the simulation is set to $N_x = N_y = 128$ and the modulus is calculated from part of the network within a box in the center of the system with box size $N'_x = N'_y = 108$. 46
3.6 Area bulk modulus K as a function of p_y at fixed $p_x = 0.5$ and for different system sizes (as shown in legend). 47
3.7 The shear modulus G and bulk modulus K as a function of p_y at fixed $p_x = 1$. 48
3.8 The shear modulus G and bulk modulus K as a function of p_x at fixed $p_y = 1$. The inset shows the effective medium elastic constant α_m as a function of p_x at fixed $p_y = 1$. 49
3.9 Phase diagram with semiflexibility included. The black line denotes the nonrigid-rigid boundary in the absence of bending. 50

4.1 Schematic of the actin-LINC complex-lamin-chromatin (DNA+proteins) coupling. Figure from Ref. [129] 54
4.2 Schematic for potential mechanisms for the mechanical regulation of transcription. In (A) the cell is exposed to uniaxial stretch. In (B) various effects of that stretch are proposed. Figure from Ref. [129]. 55
4.3 Schematic of coupled network. 57

4.4 The shear modulus G as a function of $p_{1,ij} = p_1 = p_2 = p_3$ for small strain ($\epsilon = 5\%$) and $k_1 = 1.0$. The inset shows the same data on a log-linear scale. The system size in the simulation is $L_x = L_y = L_z = 16$. Note that G is measured in units of the spring constant and the lattice spacing. . . 58
4.5 Energy as a function of percent strain for different values of $p_{1,ij} = p_1 = p_2 = p_3$. Note that energy is measured in units of the spring constant and the lattice spacing. 59
4.6 G as a function of $p_{1,3}$ for different p_{2z}s. The strain is 4 percent and $L_x = L_y = L_z = 16$. 60
4.7 Energy as a function of strain for different p_{2z}s and several $p_{1,3}$s. 61

5.1 (Color online) (a)-(e) Buckling of a ring with $N = 38$ total droplets. The initial osmolarities of the two rows are $C_1 = 0.1$ (blue) and $C_2 = 1.0$ (red), respectively. Snapshots were generated using the Visual Molecular Dynamics (VMD) package [136] and rendered using the Tachyon ray tracer [137]. 65
5.2 (Color online) Plot of the ring buckling phase diagram as a function of top row osmolarity C_1 and total number of droplets N. The bottom row osmolarity is fixed at $C_2 = 1.0$. The symbols, obtained from simulation, should be compared with lines showing analytical results. 66
5.3 Schematic figure for the onset of ring formation. 67
5.4 Schematic figure for the onset of ring buckling. 68
5.5 (Color online) Typical initial (left) and final (right) configurations for the formation of spirals. 70
5.6 (Color online) (a) The radius of the spiral as a function of K_n for different K_ls. (b) The pitch of the spiral as a function of K_n for different K_ls. . . 71
5.7 (Color online) (a)-(d) Forming a tetrahedral shell ($C_1 = 1.0$ and $C_2 = 5.0$). The color represents osmolarity with blue/red representing low/high osmolarity with white intermediate. 72
5.8 (Color online) (a)-(c) Three snapshots from the reversible folding process. 72
5.9 (Color online) Reversibility dependence on the z coordinate of the horizontal plane and the osmolarity of the surrounding medium. 73

A.1 Showing the notation for constructing the effective medium theory. [18] . 75

B.1 The contour plot of a function, with the steps of the steepest descent method in green and of the conjugate gradient method in red. [145] 81

E.1 Left: Schematic denoting notation used. Right: Difference in energy between the perturbed and unperturbed cylinder as a function of wavenumber q for $\sigma R_o^2/\kappa = 2.67$, $L/R = 10$, and $a = 0.16$ nm. 87

Chapter 1

Introduction

Soft matter is the study of the matter that easily deforms via thermal fluctuations or external or internal driving. Given this rather inclusive definition, a vast range of systems falls under the soft matter purview—polymers, colloids, membranes, granular materials, droplets, liquid crystals—to name a few. This thesis is, in some sense, a microcosm of soft matter in that it analyzes three of these systems—membranes, polymers, and droplets—to answer questions about shape, mechanics, and programmability. Given its inclusiveness, I will use the introduction to give some background on the mathematical modeling for each system. Moreover, since much of the work here is inspired by biological and/or experimental systems, I will also briefly discuss the relevant biology and/or experiments.

As you continue through the introduction, here is (1) a list of questions to keep in mind, (2) a diagram that provides a topical roadmap, if you will, for the remainder of the thesis, and (3) a biological roadmap for the remainder of the thesis since we will refer to certain biological components from time to time and would not want to leave behind scientists who are not familiar with such entities. See Figures 1.1 and 1.2. As for the questions:

- How does the mechanical interaction between a fluid membrane and ultimately a polymer network change the shape of the membrane to ultimately allow it to pinch off in a way similar to a drop of water dripping from a faucet? Answering this question pertains to endocytosis, or how a cell membrane changes shape to ingest a macromolecule.
- What role does anisotropy play in the mechanics of polymer networks modeled as disordered spring networks? More specifically, how does anisotropy affect the rigidity transition in such networks as polymer density is increased, for example?

Answering this question concerns the actin cytoskeleton and the stiffness of broad, thin protrusions that emerge at the leading edge of a crawling cell.

- What does the mechanics of two coupled polymer networks look like? How much of the mechanics depends on the nature of the coupling? In particular, how is the rigid transition affected not only as a function of polymer density but as large strains are applied? Answering this question pertains to the potential role the actin cytoskeleton has in mechanically regulating transcription, the initial step in gene expression.
- How can one program the osmolarity of an ordered network composed of water droplets coated in surfactants to change the shape of the network? And how, by introducing osmotic interactions with the environment, can the droplet network reverse its change in shape? Answering the latter question, in particular, contributes to the beginning of osmotic robotics.

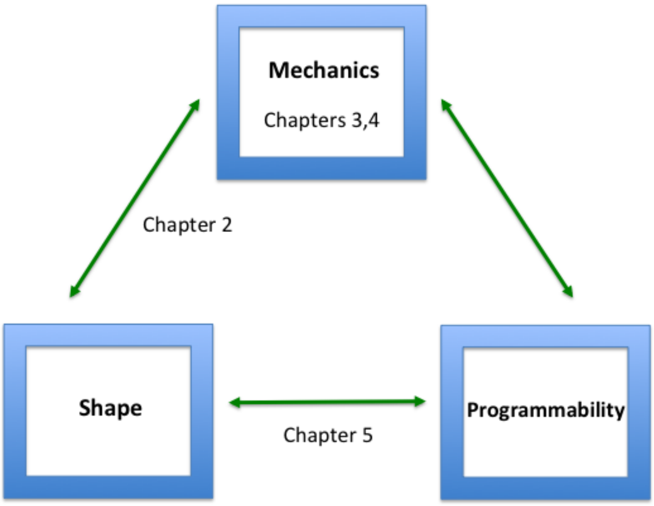

FIGURE 1.1: Roadmap for the thesis.

1.1 Fluid membranes

Lipids are amphiphilic molecules which consist of one part, called the head, which is hydrophilic, and another part, called the tail, which is hydrophobic. A collection of such molecules will self-assemble into a lipid bilayer as shown in Figure 1.3. A canonical

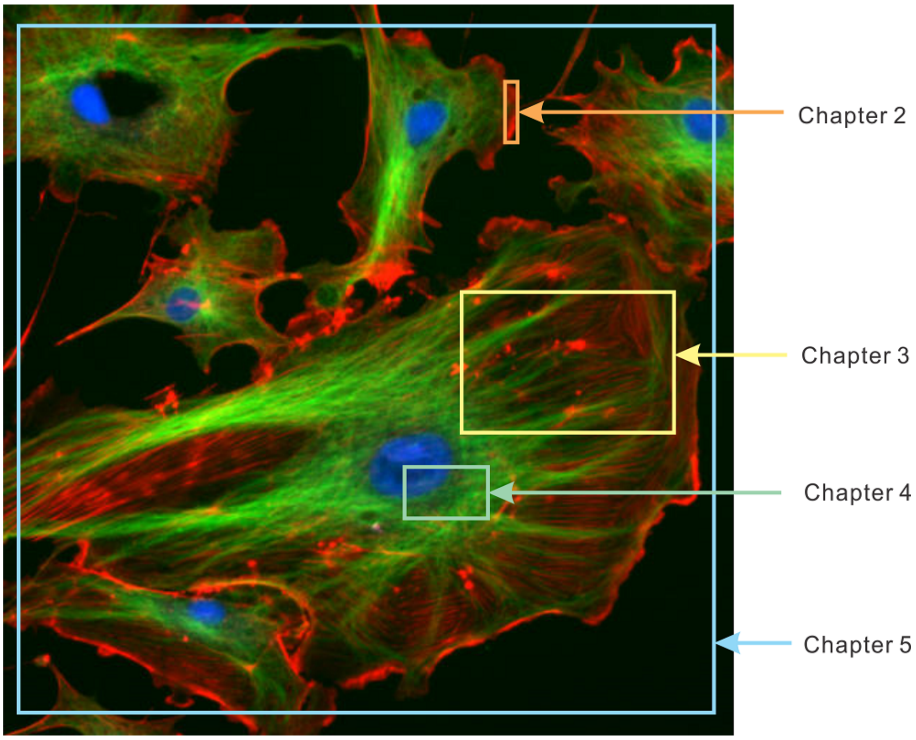

FIGURE 1.2: Biological roadmap

example of a fluid membrane is the cell membrane with phospholipids as its major component. To describe the energetics of a fluid membrane, a red blood cell membrane in particular, Canham [1] conjectured that energy is governed principally by membrane curvature such that

$$E_{FM} = \frac{1}{2}\kappa \int (\frac{1}{R_1^2} + \frac{1}{R_2^2})dS, \tag{1.1}$$

where R_1 and R_2 denote the principal curvature radii of the membrane surface (see Figure 1.4), κ denotes the bending rigidity, and dS represents an infinitesimal area. For specificity, this membrane energy represents the neutral surface of the physical membrane and approximately corresponds to the contact between the two leaflets of the lipid bilayer [2].

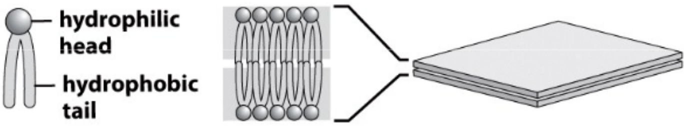

FIGURE 1.3: Schematic of the lipid bilayer, with hydrophilic heads exposed and hydrophobic tails sequestered

A more general form was given by Helfrich [3]. By introducing local Cartesian coordinates on the membrane, imposing that the z-axis be parallel to the surface normal vector at each point on the membrane, Helfrich defined the two principal curvatures as follows. Expressing the normal vector $\mathbf{n} = (n_x, n_y, n_z)$ as a function of coordinates x and y, the principal curvatures at each point are given by the eigenvalues of the matrix M whose entries are given by

$$\begin{pmatrix} \frac{\partial n_x}{\partial x} & \frac{\partial n_x}{\partial y} \\ \frac{\partial n_y}{\partial x} & \frac{\partial n_y}{\partial y} \end{pmatrix}$$

Due to the rotational symmetry of the membrane, only combinations of $\mathbf{n}$ that are independent of orientation of the $x-$ and $y-$ axis can appear in the E_{FM}. These combinations are $\frac{\partial n_x}{\partial x} + \frac{\partial n_y}{\partial y}$, $(\frac{\partial n_x}{\partial x} + \frac{\partial n_y}{\partial y})^2$, and $\frac{\partial n_x}{\partial x}\frac{\partial n_y}{\partial y} - \frac{\partial n_x}{\partial y}\frac{\partial n_y}{\partial x}$. The energy density (per unit area) e_{FM} then becomes

$$e_{FM} = \frac{1}{2}\kappa(\frac{\partial n_x}{\partial x} + \frac{\partial n_y}{\partial y} - C_0)^2 + \kappa_G(\frac{\partial n_x}{\partial x}\frac{\partial n_y}{\partial y} - \frac{\partial n_x}{\partial y}\frac{\partial n_y}{\partial x}), \tag{1.2}$$

where κ_G is the Gaussian rigidity and C_0 is the spontaneous curvature to account for potential asymmetry between the two monolayers constituting the bilayer.

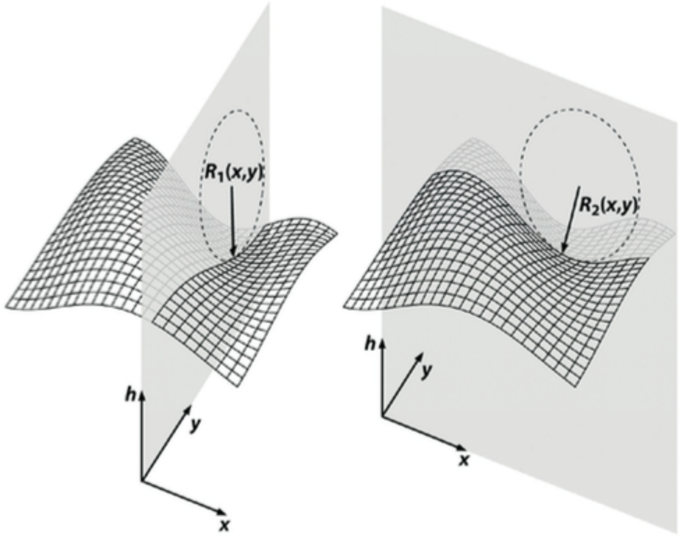

Figure 1.4: Schematic for the membrane curvature, showing the principal curvature radii R_1 and R_2.

Choosing the local coordinate systems such that the derivatives along its axes correspond to the smallest and largest curvatures of the membrane surface, the mixed derivatives vanish and the principal curvatures become $C_x = \frac{\partial n_x}{\partial x}$ and $C_y = \frac{\partial n_y}{\partial y}$ with

$$e_{FM} = 2\kappa(H - C_0)^2 + \kappa_G K_G, \tag{1.3}$$

where $H = \frac{c_x + c_y}{2}$ is the mean curvature and $K_G = c_x * c_y$ is the Gaussian curvature. Note then that κ has units of energy. It turns out that the second term in the energy density is topological in nature. The Gauss-Bonnet theorem states that

$$\int K_G dS = 4\pi(1-g), \tag{1.4}$$

where the integer g is the genus of the surface, i.e. the number of handles, and thereby characterizes the topology of the surface. If K_G is assumed to be constant, then this term does not change for a one-component membrane whose topology does not change, i.e. it is a constant. One can also add surface tension and pressure to the energy above as we will see in Chapter 2.

Endocytosis is the process by which extracellular agents are ingested by the cell as a result of the cell membrane surrounding and engulfing them [4]. To do so, the membrane changes shape and then pinches off to form a vesicle that encloses the now intracellular material. Fig. 1.5 presents a schematic of endocytosis in mammalian cells. Clathrin is one of the first proteins recruited to the endocytic site. The spontaneous curvature of individual clathrin molecules presumably helps initiate membrane deformation as they assemble to form a spherical cage. The pinch-off is driven by the motor protein dynamin, which actively contracts.

In yeast, dynamin is not present in endocytosis [5–7]. So how, then, does the membrane pinch-off? It turns out that actin filaments reshape the membrane, in addition, to clathrin. But these two proteins do not necessarily allow for pinch-off. So what about the mechanism for pinch-off? Is there any underlying instability, or is there a more engineered approach with the pinch-off occurring at some fixed distance from the top of the invagination? In chapter 2 we identify a possible mechanism that could assist in the pinch-off via a pearling-like instability, where surface tension competes with bending energy in cylindrical vesicles such that, for long enough cylinders, it is energetically favorable for the cylinder to break up into spheres.

We will also address how the actin reshapes the cell membrane. The interplay of mechanics and shape is not immediately obvious since there are currently several competing proposals put forth by the biologists as to how this interplay is achieved. Each of these proposals for endocytosis in yeast assumes its own respective organization for the actin filament network. Can any of these models be ruled out on the basis that they do not provide the forces required to deform the cell membrane that is consistent with observations? This question will be studied in Chapter 2.

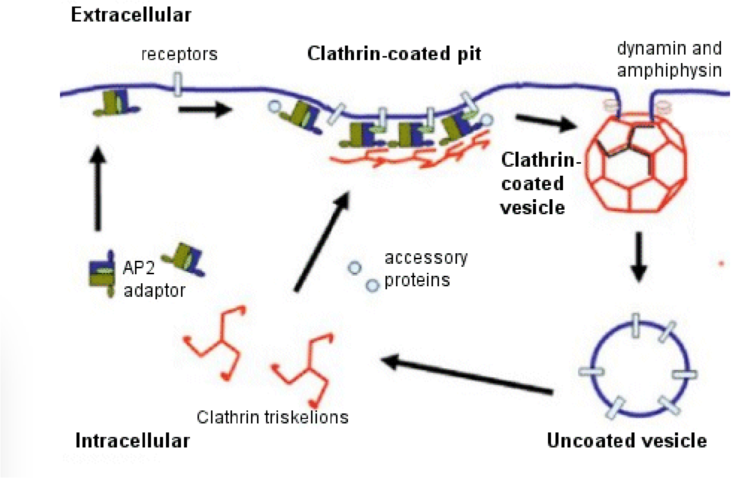
Extracellular
receptors
Clathrin-coated pit
dynamin and amphiphysin
Clathrin-coated vesicle
AP2 adaptor
accessory proteins
Clathrin triskelions
Intracellular
Uncoated vesicle

FIGURE 1.5: Schematic of endocytosis in mammalian cells. Figure taken from website: www.abcam.com from an article by Dr. Tony Jackson.

1.2 Polymers and disordered spring networks

Polymer chains abound in nature from DNA to cytoskeletal filaments to spider silk to latex from a rubber tree. See Figure 1.6 for a schematic image of an actin cytoskeletal filament [8, 9]. To characterize the mechanical properties of polymers, a lengthscale known as the persistence length l_p can be introduced [10–13]. For polymers much shorter than their persistence length, they act as rigid rods. For polymers much longer than their persistence length, they act as flexible filaments. And for polymers around the length of the persistence length, they are semiflexible. Energetically speaking, semiflexible polymers bend. However, in the presence of thermal fluctuations, polymers with no compliance in their contour length exhibit end-to-end fluctuations that act as a stretching contribution to the free energy. Flexible polymers are purely entropic, i.e. only stretch.

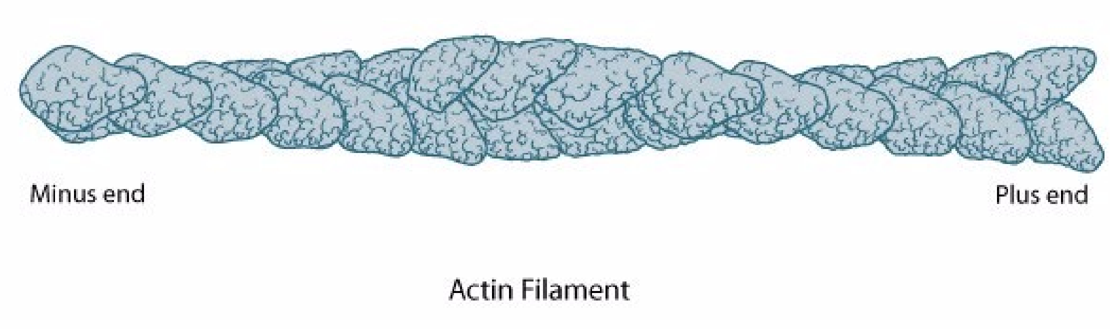
Minus end
Plus end
Actin Filament

FIGURE 1.6: Structure of an actin filament showing the barbed (or plus) and pointed (or minus) ends [14]

Many polymers cross-link together to form disordered networks as the case with the cytoskeleton and rubber tree latex in which there is no symmetry transformation going from one cross-link position in the network to another. See Figure 1.7 for a schematic. The cytoskeleton does so to form a semiflexible polymer network, while the rubber tree latex forms a flexible polymer network. To investigate the mechanics of such systems near a rigidity transition, continuum elasticity breaks down requiring a more microscopic description of the system. What do I mean by rigidity transition? The sol-gel (solution-to-gelation/fluid-to-solid) transition occuring in polymer networks as polymer concentration increases, for example. De Gennes, who some might say is the father of soft matter, conjectured that the sol-gel transition is analogous to a percolation transition and that the shear modulus near the gelation critical point behaves like conductivity in a network of random resistor. Feng and Sen [15], however, showed that this is not the case when considering only stretching between cross-links—that the rigidity percolation transition is in a different universality class than conductivity percolation.

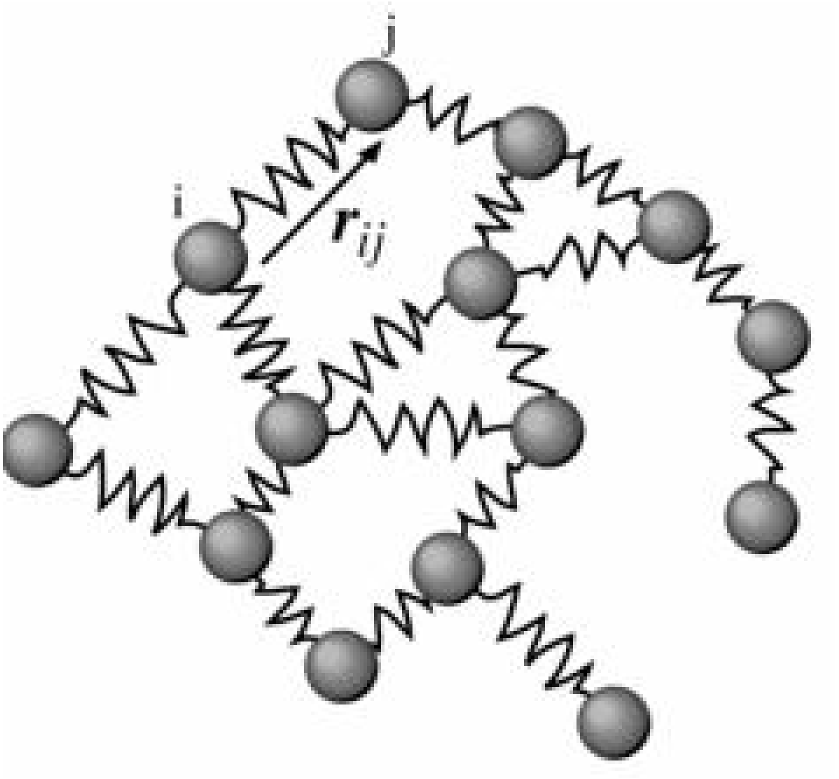

Figure 1.7: Schematic of a disordered spring network.

To bring the reader up to speed on rigidity transitions in disordered spring networks, I will briefly review the canonical example of a randomly diluted triangular lattice with linear springs between the cross-links. I do so because I will explore modifications of this system in Chapters 3 and 4 to understand how the modifications affect the transition. The energy of the system is given by

$$E = \frac{\alpha}{2} \sum_{\langle ij \rangle} p_{ij} \left(\mathbf{u}_{ij} . \mathbf{r}_{ij} \right)^2 , \tag{1.5}$$

where $\mathbf{r}_{ij}$ is the unit vector along bonds, and $\mathbf{u}_{ij} = \mathbf{u}_i - \mathbf{u}_j$, the strain on the bond ij.

Let's begin with why do we expect a rigidity transition in the first place? Maxwell answered this question back in 1864 [16]. For N cross-links in d dimensions and a mean number of springs per node denoted by z, the forces yield $zN/2$ constraints. Since each cross-link has d translational degrees of freedom, there are $(N-1)d$ total degrees of freedom (subtracting out the global degrees of freedom). When the total degrees of freedom match the force constraints, we arrive at the isostatic criterion, or $zN/2 = (N-1)d$. In the limit $N \to \infty$, $z_{iso} = 2d$. For $z < 2d$, the network is flexible, or solution-like, since there are not enough constraints to stabilize the degrees of freedom. For $z > 2d$, the network is rigid. Working in terms of the dilution probability $1-p$, the isostatic criterion translates to $p_r = 2d/Z$, where Z is the coordination number of the fully occupied lattice. It turns out that numerics yield a slightly smaller value of p_r due to spatial correlations in two dimensions [17]. The above counting does not take such correlations into account. The isostatic criterion is a necessary but not sufficient criterion for rigidity.

One can then compute the shear and bulk modulus of the system as a function of the dilution probability p to find that in the solution phase, both the shear and bulk modulus are zero as expected. See Figure 1.8 [18, 19]. Both mean field and numerical simulations reveal that the shear and bulk modulus increase linearly from zero for $p > p_r$ with a slope that is dictated by the mean field theory. Very close to the transition, the linear scaling breaks down indicating that the transition in two-dimensions is not completely governed by mean field theory, though it is a reasonable first-approximation. I will review one version of this mean field theory in Appendix A, which for historical reasons, is known as effective medium theory (EMT). I do so because I will be building upon this EMT in Chapter 3. As of today, there is no consensus as to how to proceed beyond mean field theory for reasons that go beyond the boundaries of this thesis.

The disordered linear spring network can be extended to include angular springs. See Figure 1.9 for a schematic. Angular springs can model the bending contribution for semiflexible polymers, for example. Recent work by Das and collaborators [20] developed an EMT with an energy

$$\begin{aligned} E &= \frac{\alpha}{2}\sum_{\langle ij\rangle} p_{ij}\left(\mathbf{u}_{ij}.\mathbf{r}_{ij}\right)^2 + \frac{\kappa_c}{2}\sum_{\langle \widehat{ijk}=\pi\rangle} p_{ij}p_{jk}((\mathbf{u}_{ji}+\mathbf{u}_{jk})\times\mathbf{r}_{ji})^2 \\ &+ \frac{\kappa_{nc}}{2}\sum_{\langle \widehat{ijk}=\pi/3\rangle} p_{ij}p_{jk}\, p_{nc}\, \Delta\theta_{ijk}{}^2 \end{aligned} \tag{1.6}$$

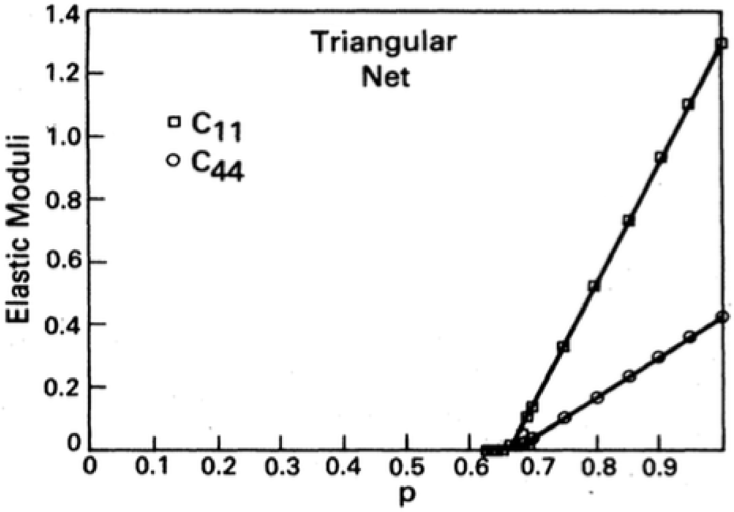

FIGURE 1.8: Elastic constants C_{11} (bulk modulus) and C_{44} (shear modulus) averaged over three configurations for a 440 atom triangular network. Both constants are in units of the spring constant and the lattice spacing. The straight lines denote the effective-medium theory results. Figure taken from Ref. [18].

where p_{ij} is the probability that a bond is occupied, $\sum_{\langle ij \rangle}$ represents sum over all bonds, $\sum_{\langle ijk \rangle}$ represents sum over pairs of bonds sharing a node, The first term in the deformation energy corresponds to the cost of extension or compression of the bonds, the second term to the penalty for the bending of filament segments made of pairs of adjacent collinear bonds, and the last term to the energy cost of change in the angles between crossing filaments that meet at 60° angle with p_{nc} the probability of having an angular spring between the two filaments.

For $\kappa_{nc} = 0$, they found that the EMT yielded a $p_r = 0.457$, which is in rather good agreement with the simulations. See Figure 1.10. Since the additional angular springs give rise to more constraints, the rigidity percolation threshold is lowered. The EMT captures the shape of the shear modulus for different ratios of stretching to bending but does match quantitatively. In addition to laying the groundwork for an EMT for angular springs—a quandary that began over 30 years ago—the authors explored the role of angle-constraining crosslinkers to find that the rigidity transition is pushed down to its lowest bound—the connectivity percolation threshold—a conjecture that had been made over 30 years ago. Since the actin cytoskeleton is cross-linked by more than 100 different cross-linking proteins, some of which are freely-rotating and some of which are not, these angle-constraining cross-links provide a mechanism for the actin cytoskeleton to become rigid at the lowest possible actin concentration. Given that there is only a finite amount of the actin in a cell, wise use of its resources is presumably a high priority.

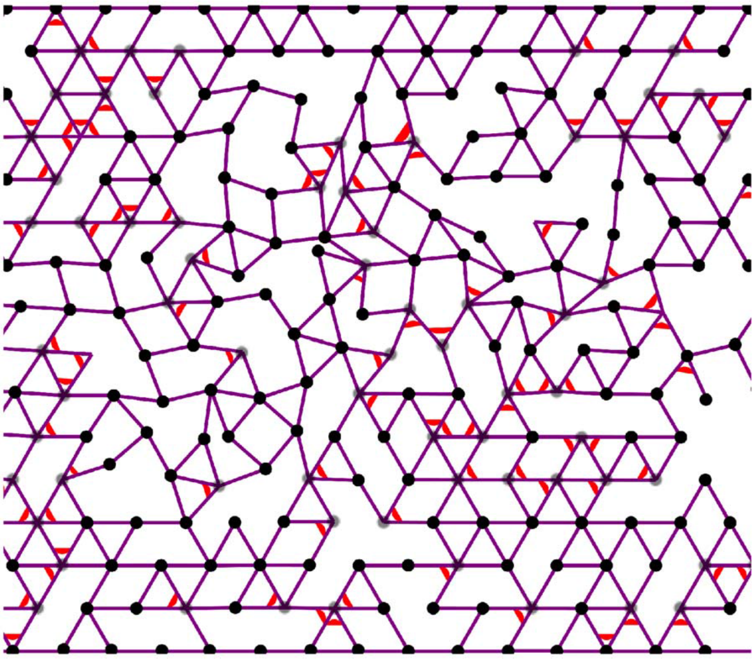

Figure 1.9: Deformed configuration a compositely crosslinked semiflexible filament network with 2.7 percent strain. The bond occupation probability is $p = 0.64$, and angle-constraining crosslinker occupation probability is $p_{nc} = 0.15$. The purple lines denote semiflexible filaments, the red arcs denote angle-constraining crosslinkers, the black circles represent nodes where all crossing filaments are free to rotate around that node, while the grey circles denote nodes where some of the crossing filaments are free to rotate around that node. The absence of a black or grey circle denotes a node where no free rotations are possible. The filament bending stiffness relative to stretching stiffness $\kappa_c/\alpha = 10^{-6}$ and the stiffness of angular crosslinkers relative to stretching stiffness $\kappa_{nc}/\alpha = 10^{-6}$. [20]

The actin cytoskeleton [9–13] is also the inspiration behind Chapters 3 and 4. As for Chapter 3, cell crawling is essential to a variety of biological processes such as the development of an organism, wound healing, cancer metastasis and immune response. Cell crawling is a highly dynamic phenomenon primarily driven by the actin networks beneath the cell membrane. The constant restructuring of the actin cytoskeleton is vital in enabling the cell to change its elastic properties rapidly, and this dynamic response is fundamental for movement. As Fig 1.11 shows, after determining its direction of motion, the cell extends a protrusion in this direction by actin polymerization at the leading edge. It then adheres its leading edge to the surface on which it is moving and de-adheres at the cell body and rear. Finally, it pulls the whole cell body forward by contractile forces generated at the cell body and rear of the cell.

The broad, thin protrusion at the leading edge of the cell is known as a *lamellipodium* [23]. Growth of the free barbed ends of branches produces the force that pushes the plasma membrane forward at the leading edge of motile cells [22, 24]. As Fig 1.12 shows, the

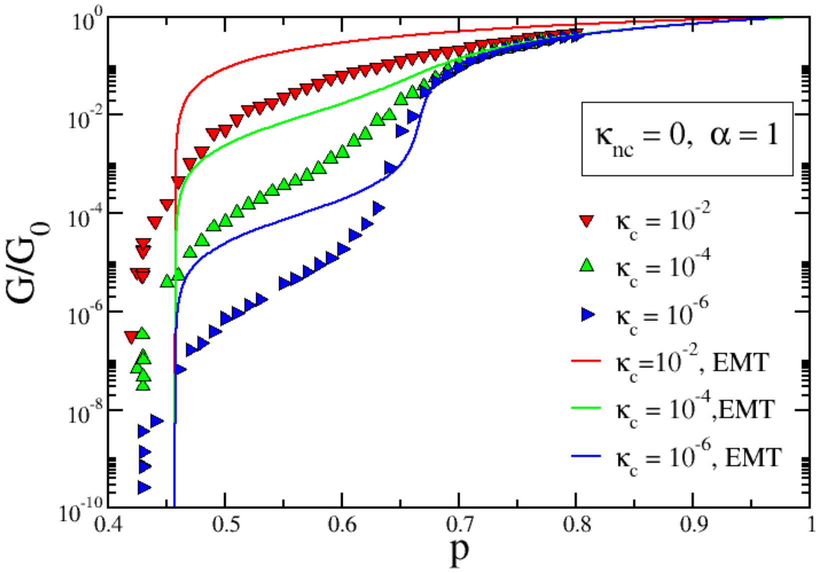

Figure 1.10: The shear modulus G, normalized by its value for the corresponding undiluted network G_0, as a function of occupation probability $p = p_{ij}$. The data points are numerical results and the solid lines, the effective medium theory results [20].

cytoskeleton in lamellipodia consists of rather oriented, cross-linked filaments, motivating me to extend the analytical framework of effective medium theory to disordered linear spring networks with anisotropy in Chapter 3. I should point out that most of the results in Chapter 3 deal with linear spring networks, i.e. no bending. This was because I thought it was important to understand the simpler "just stretching" case first before proceeding to include bending.

As for Chapter 4, a new role for the actin cytoskeleton has recently emerged, namely a role in the mechanical regulation of transcription by interacting with the DNA. As Figure 1.13 shows, cytoskeletal actin filaments bind to nesprin-1 and -2 located on the outer nuclear membrane. Nesprins interact across the perinuclear space through their C-terminal KASH domain with SUN proteins, which reside in the inner nuclear membrane. The SUN proteins can then bind to the lamin network located just inside the inner nuclear membrane. This complex of proteins connecting the nuclear lamina and the actin cytoskeleton is called LInkers of the Nucleoskeleton and Cytoskeleton (LINC) complexes [26, 27]. Lamins are intermediate filaments forming a filamentous network surrounding the DNA, RNA, and other proteins located at the core of the cell nucleus [28]. Therefore, through the sequence of actin filaments binding to nesprins binding to SUN proteins binding to lamins binding to DNA, there exists a means by which forces imposed on cytoskeletal actin are transmitted to the DNA.

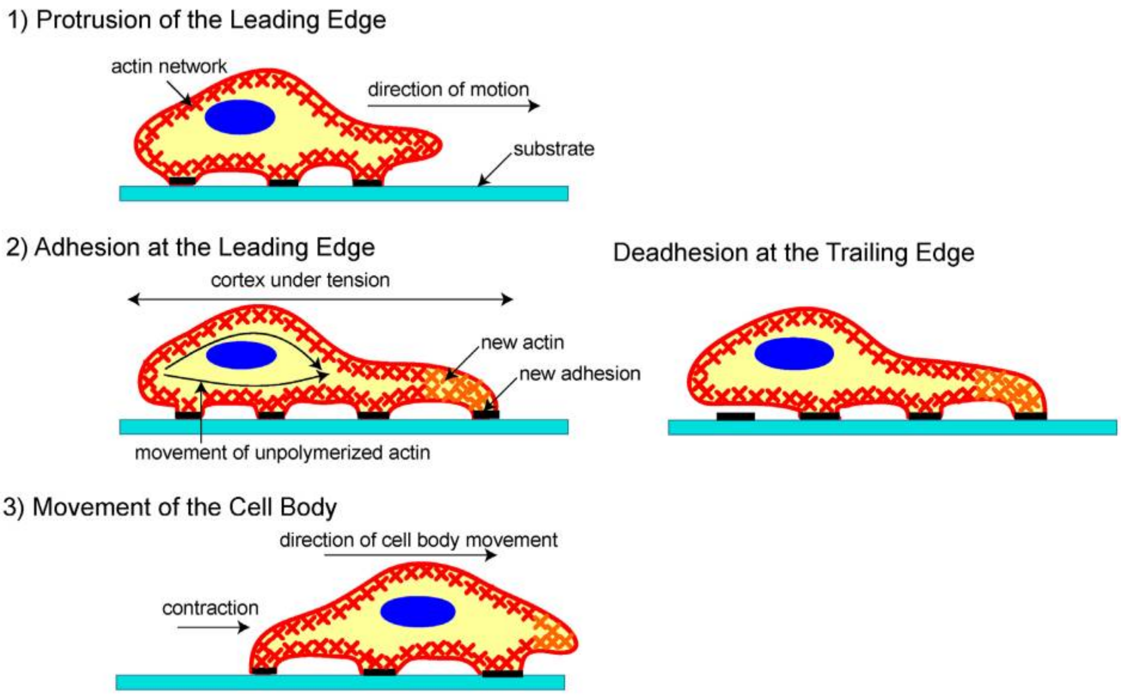
1) Protrusion of the Leading Edge
actin network
direction of motion
substrate
2) Adhesion at the Leading Edge
cortex under tension
new actin
new adhesion
movement of unpolymerized actin
Deadhesion at the Trailing Edge
3) Movement of the Cell Body
direction of cell body movement
contraction

FIGURE 1.11: Schematic of cell crawling by extension of the lamellipodium via actin polymerization. [21]

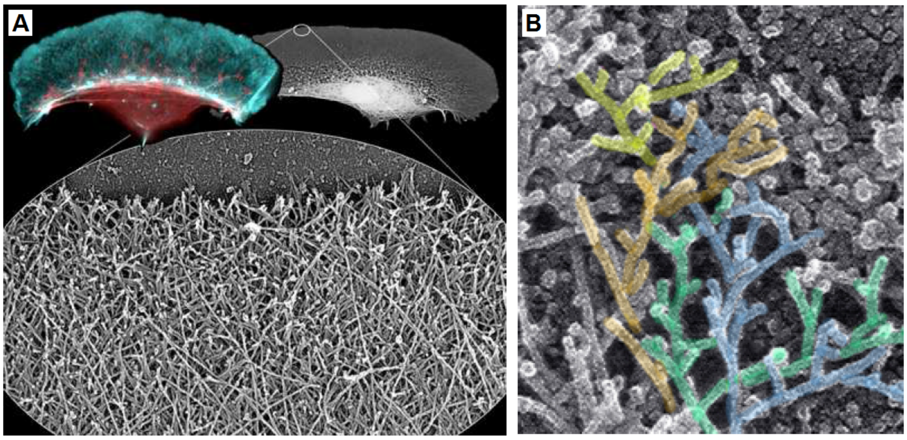

FIGURE 1.12: A, Electron micrograph of a cell showing a dense branched network of integrated actin filaments. B, Smaller scale image of dendritic branches of actin filaments. [22]

To begin to investigate a microscopic basis for the mechanical regulation of transcription via the actin cytoskeleton, I will first study the mechanics of two coupled disordered spring networks with stretching only in Chapter 4, again, to understand the simpler ”just stretching” limit first before proceeding to the more complex case.

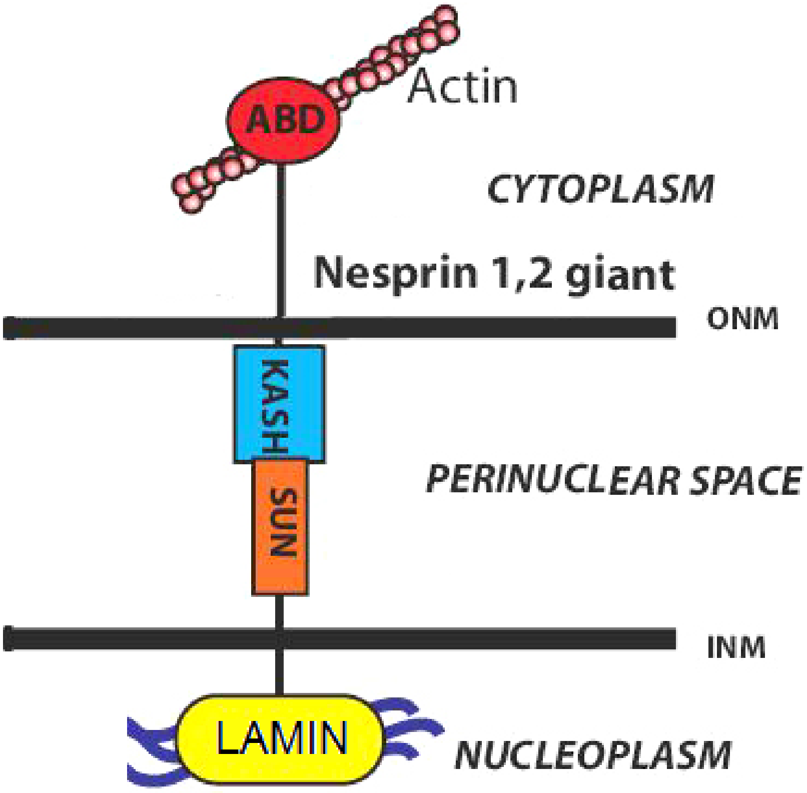

FIGURE 1.13: Structure of LINC complexes. ABD: Actin-binding domain; INM: Inner Nuclear Membrane; ONM: Outer Nuclear Membrane. [25]

1.3 Droplet networks

In nature there are many biomaterials that are internally programmed to morph into complex structures that actively and adaptively interact with the environment. This has inspired the development of *programmable* materials that controllably fold into designated structures. At the nanometer scale, the programmable chemistry of Watson-Crick base pairing allows DNA to self-assemble into a tetrahedron [29]. At the millimeter scale, efficient algorithms have been constructed to generate self-folding three-dimensional polyhedra from two-dimensional nets, driven by the minimization of the surface tension of liquid hinges that either rotate or fuse panels into place [30]. At the centimeter scale, researchers have created a self-folding robot that goes from flat to walking in several minutes without external intervention [31].

1.3.1 Bayley group's experiment

A beautiful realization of these ideas comes from the Bayley group who print tens of thousands of micron-sized aqueous droplets each joined by single lipid bilayers [32–36]

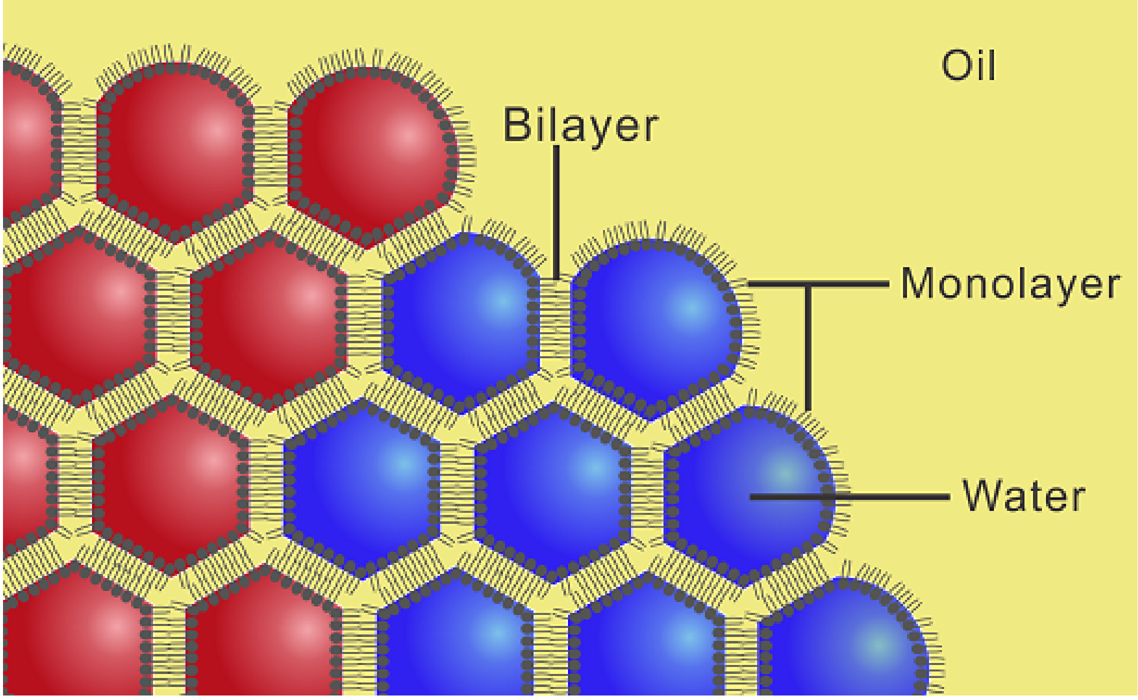

FIGURE 1.14: Schematic image showing droplets of different aqueous solutions printed into a solution of lipids in oil. The droplets acquire a lipid monolayer and form bilayers with droplets in the developing network. [32]

to form a cohesive, tissue-like material (Fig. 1.14). The droplets in these networks can be endowed with different osmolarities. The resultant osmotic pressure leads to local fluid flow from low to high concentration. This swells the high concentrations droplets and shrinks the low concentration droplets, leading to internal stresses which distort the shape of the network in specific ways depending on the initial geometry of the network and the concentration differences.

The initial experiments explored rectangular strips composed of droplets of just two distinct osmolarities. The respective swelling and shrinking causes the rectangular strip to deform into a ring (see Fig 1.15).

The initial droplet network experiments also explored the formation of a hollow sphere from an initial two-dimensional four-petal-shaped structure (see Fig 1.16), thus demonstrating the spontaneous assembly of three-dimensional shapes. These droplet networks can also be functionalized electrically and magnetically, mimicking rapid, long-distance electrical communication along a defined path in a way that is analogous to neurons. Should such droplet networks be integrated with living organisms they could mimic biological tissue with the droplets acting as cells.

In Chapter 5, we will use computational methods to explore the self-assembly of several shapes including rings, spirals and tetrahedral shells. We will revisit the formation of

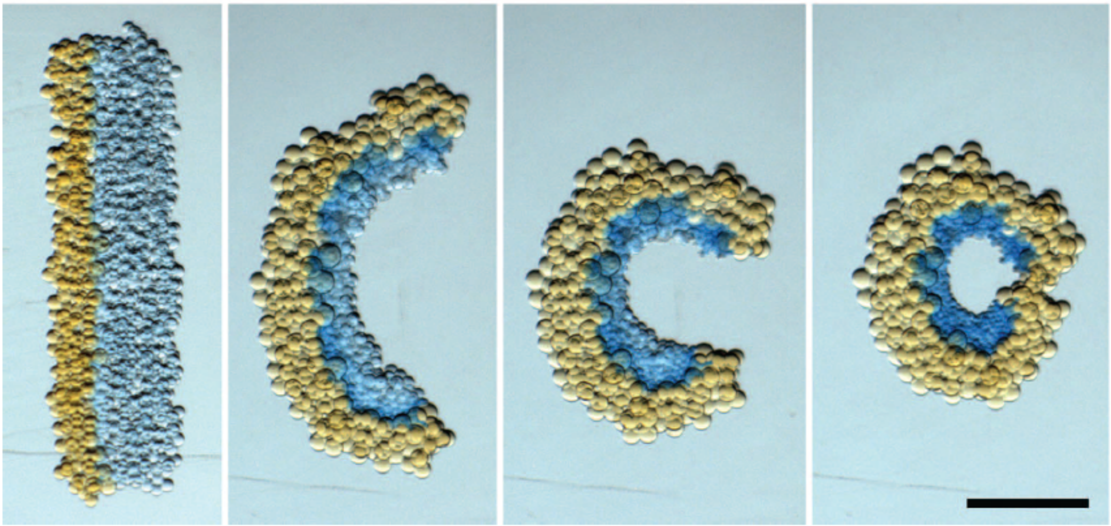

Figure 1.15: Photographs of a rectangular network folding into a circle over 3 hours. The orange and blue droplets initially contained 250 mM KCl and 16 mM KCl, respectively. Scale bar, 250 mm [32]

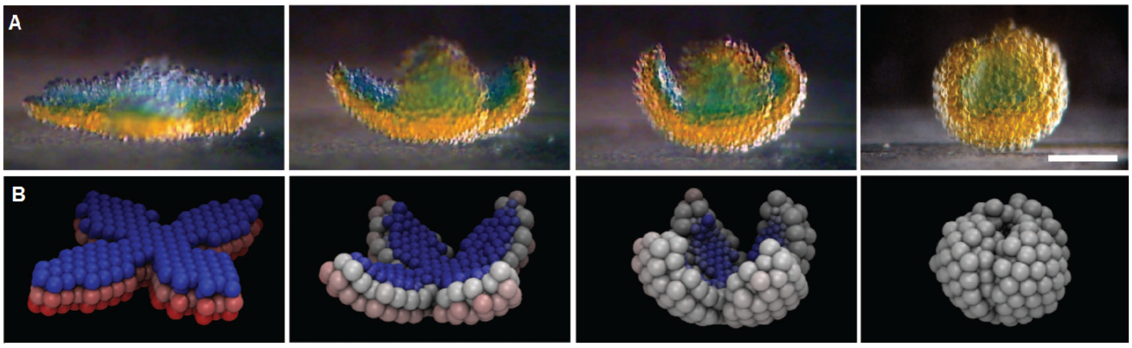

Figure 1.16: (A) Photographs of a flowershaped network folding spontaneously into a hollow sphere. The orange and blue droplets initially contained 80 mM KCl and 8 mM KCl, respectively. The photographs cover a period of 8 hours. Scale bar, 200 mm. (B) Frames from a folding simulation of a network with a similar initial geometry to the network in (A). Blue and red represent the lowest and highest initial osmolarities, respectively, and white indicates the average of the two. [32]

rings studied in [32] and identify a buckling transition from a round to a polyhedral ring after ring closure. The spirals provide an interesting example of an initial quasi-one-dimensional structure generating a three-dimensional structure. Tetrahedra, the simplest and least symmetric class of the regular polyhedra, can serve as mesoscopic building blocks for molecules and bulk materials with sp^3-like directional bonding [37, 38]. We will also illustrate reversibility with shape shifting from a four-petal configuration to a hollow sphere transition and back. This opens the way to osmotically-driven small scale robotics.

Chapter 2

Endocytosis in yeast

2.1 Motivation

Endocytosis is the process by which extracellular agents are ingested by the cell as a result of the cell membrane surrounding and engulfing them [4]. The membrane then pinches off to form a vesicle that encloses the now intracellular material. Fig. 2.1 presents an electron micrograph image of a deformed cell membrane near pinch-off in S. cerevisiae [39]. Experiments have identified a handful of core proteins, though there are upwards of 50 proteins participating in the endocytotic machinery [5–7]. Live cell imaging of these fluorescently labeled core proteins provide us with a sequence of events for the endocytotic machinery [40, 41]. Though the composition and time-line of the endocytotic machinery is known, in yeast, there are competing proposals about how these few core proteins interact with the cell membrane to deform it into a vesicle [42–44].

According to experiments, the sequence of events in the endocytotic machinery in yeast is as follows [45, 46]. Clathrin is recruited to the invagination site [47], along with adaptor proteins, such as Sla1 and Ent1/2 [7]. Sla1 and Ent1/2 proteins bind the clathrin to the membrane, while Sla2 proteins bind actin filaments to the membrane [7]. Another protein, WASp, is also recruited to the site. WASp is an activator for the branching agent Arp2/3, enabling a branched actin filament network to be generated near the invagination site [40]. The growth of this network drives membrane tube formation. BAR proteins eventually become prominent and help facilitate pinch-off of the membrane [48]. Fig. 2.2 illustrates this process using what will turn out to be Proposal 1 for the organization of the actin. The initial invagination due to clathrin and other adaptor proteins takes about one to two minutes. The time for the tube to form and pinch-off, in

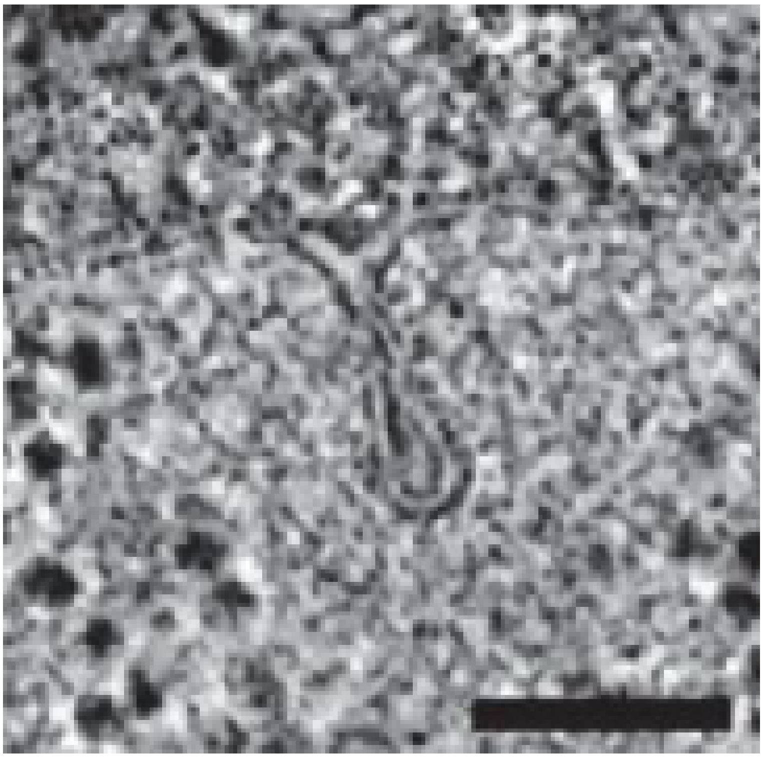

Figure 2.1: An electron micrograph image of a deformed membrane during endocytosis in S. cerevisiae. The image is reprinted with permission from [39]. The scale bar is 100 nm.

contrast, takes only about 10-15 seconds. The length-to-radius ratio of the tube before pinch-off is typically 7-10 [39] (Fig. 2.1).

Clathrin is one of the first proteins recruited to the endocytic site. Each clathrin molecule is a nonplanar triskelion that can pucker in the center [49]. Clathrin molecules bind together to form a basket-like structure as a result of the intrinsic curvature of the molecules. Clathrin molecules, however, require adaptor proteins, such as Sla1 and Ent1/2, to bind to the membrane [7, 50]. The spontaneous curvature of individual clathrin molecules presumably helps initiate membrane deformation as they indirectly attach to the membrane via adaptor proteins with the initial deformation being rather small, in contrast to mammalian cells.

How the actin filament network reshapes the membrane is even less clear since there are currently three competing proposals put forth by the biologists as to how this is done. The first proposal (Proposal 1) argues that the barbed/plus ends of polymerizing actin filaments are oriented towards the flat part of the membrane with the pointed/minus ends anchored just above the clathrin bowl [42]. A second proposal (Proposal 2) argues that a collar-like structure of plus end filaments anchored to the rest of the cytoskeleton

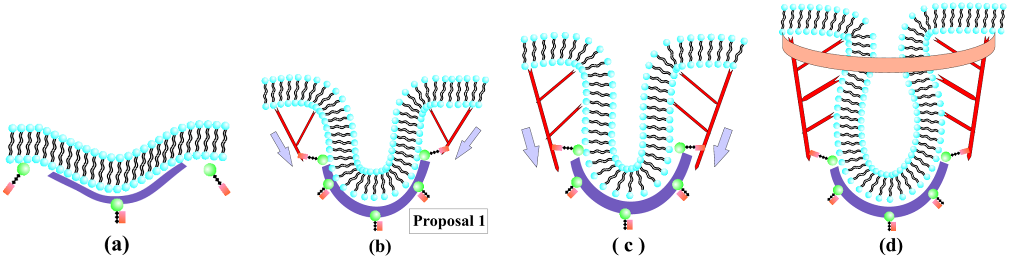

Figure 2.2: Schematic for endocytosis in yeast using Proposal 1 for the actin filament organization: (a) Clathrin (purple) attaches to the membrane (black/blue) via proteins Sla1 and Ent1/2 (not depicted here) and the protein Sla2 (green/brown) is recruited near the clathrin. (b) Actin (red) attaches to the membrane near the edge of the clathrin "bowl" via Sla2 and lengthens due to polymerization to initiate tube formation. (c) Actin continues to polymerize and lengthen the tube. (d) BAR proteins (orange) become prominent and surround part of the tube (and the actin). The grey arrows denote the direction of the actin force on the membrane. Note that potential additional actin filaments rooted in the surrounding cytoskeleton and extending towards the invagination site not been drawn.

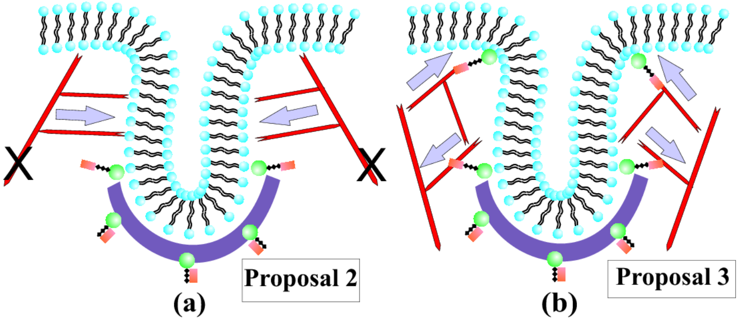

Figure 2.3: (a) Schematic depicts Proposal 2, where the actin filaments are tethered to the rest of the cytoskeleton, as denoted by the two black Xs, and polymerize inward towards the invagination site. (b) Schematic represents Proposal 3, where there are two local anchoring regions such that two actin networks form to drive tube formation. The grey arrows, again, denote the direction of the actin force on the membrane.

and oriented towards the neck of the deformation to elongate it and drive the pinch-off [43]. A third proposal (Proposal 3) suggests that there are two regions of attachment of the actin filaments to the membrane such that two branched actin networks are generated [44]. The two networks repel each other as they grow because they cannot interpenetrate and, therefore, drive tube formation. See Fig. 2.2b for a schematic of Proposal 1 and Fig. 2.3 for a schematic for Proposals 2 and 3.

Each of these three proposals for endocytosis in yeast assumes its own respective organization for the actin filament network. Can any of these models be ruled out on the basis that they do not provide the forces required to deform the cell membrane that is consistent with observations? And what about the mechanism for pinch-off? Is there any underlying instability, or is there a more engineered approach with the pinch-off occuring at some fixed distance from the top of the invagination? We approach clathrin-initiated endoctyosis in yeast by breaking up the sequence of fluid membrane deformations into three stages: (i) initiation, (ii) elongation, and (iii) pinch-off. In the process we identify a possible mechanism that could assist in the pinch-off via a pearling-like instability, where surface tension competes with bending energy in cylindrical vesicles such that, for long enough cylinders, it is energetically favorable for the cylinder to break up into spheres. An instability driven mechanism is potentially powerful given the ubiquitousness of endocytosis.

This proposed pearling-like instability mechanism will be contrasted with a competing pinch-off mechanism put forth in Refs. [42, 51]. In this model, the cell membrane is modeled as a fluid membrane—a two-component fluid membrane, where one component consists of the nonscission region and the other component consisting of the scission region such. Physically, the two regions correspond to hydrolyzed PIP_2 and non-hydrolyzed PIP_2 regions. The increasing interfacial line tension between the two components drives the pinch-off with the pinch-off distance always occuring at some fixed distance from the top of the invagination site by construction, if you will. We will ultimately compare and contrast our model with this earlier model and compare our model with another more recent model in which the cell membrane is modeled as an elastic membrane with a non-zero shear modulus [52].

In mammalian cells, the two key players in endocytosis are clathrin and dynamin, a motor protein that drives the pinch-off, which is very different from yeast. One difference between yeast and mammalian cells is the presence of a cell wall in yeast cells. This wall is needed to prevent lysis due to an internal turgor pressure, which can be as large 10^6 Pa. It has been speculated that the presence of the turgor pressure biases the use of F-actin as an invagination tool [53]. We will discuss the implications of turgor pressure for our model throughout this work.

2.2 Model and methods

The energy of a bare membrane depends on its curvature [3] and can be written as

$$E_{bare} = \int dS \left[2\kappa \left(H - C_0\right)^2 + \kappa_G K + \sigma\right] + p \int dV, \tag{2.1}$$

where C_0 is a spontaneous curvature, κ is the membrane bending rigidity, κ_G is the saddle-splay modulus, σ represents the surface tension, and dS represents the area of an infinitesimal element of the surface. Finally, p represents the turgor pressure present in yeast cells with dV the infinitesimal volume element for any deformation from a flat surface.

Beginning with the above energy functional, which models the energy of the deformations of a bare cellular membrane, we systematically incorporate new physics associated with the three stages of endocytosis by allowing the parameters to be component-dependent or by adding new terms to the energy.

2.2.1 Initiation stage

Clathrin is one of the first proteins recruited to the endocytic site. Each clathrin molecule is a nonplanar triskelion that can pucker in the center [49]. Clathrin molecules bind together to form a basket-like structure as a result of the intrinsic curvature of the molecules. Clathrin molecules, however, require adaptor proteins, such as Sla1 and Ent1/2, to bind to the membrane [7, 50]. The binding process induces curvature in the membrane. The membrane rigidity may also be affected by protein binding. In fact, membrane rigidities depend on several factors, such as membrane lipid and protein composition, to account for the range of values (tens of $k_B T$) that is reported in the literature [54].

We encode the effect of the clathrin binding, via Sla1 and Ent1/2, to the cell membrane with effective parameters characterizing the model of the cell membrane. The clathrin indirectly binding to one side of the membrane induces spontaneous curvature in the membrane. Since the clathrin indirectly binds only to part of the membrane, we study a two-component membrane, one component denoting the bare membrane and the other denoting the part of the membrane to which the clathrin is indirectly attached with non-zero spontaneous curvature. We also vary the bending rigidity of the part of the membrane to which the clathrin is indirectly attached.

The energy functional of the membrane for this initiation stage is given by [3]

$$E_{init} = \sum_{i=1,2} \int dS_i \left[2\kappa_i \left(H_i - C_{0i} \right)^2 + \kappa_{G_i} K_i + \sigma_i \right] + p \int dV_i \tag{2.2}$$

where $i = 1$ denotes the Sla1/Ent1/2-bound membrane and $i = 2$ denotes the bare membrane.

2.2.2 Elongation stage

We now ask how the emergent actin network exerts additional deformations/forces on the membrane following the initiation of endocytosis. As shown in Fig. 2.2, the protein Sla2 is recruited to the invagination site before actin assembly. Sla2 binds to the clathrin and the membrane near the clathrin, but, according to Ref. [7], Sla2 bound to the membrane near the top of the clathrin basket binds actin filaments. These Sla2 binding sites provide localized binding/anchoring of the actin filaments to the cell membrane since these Sla2 molecules are near the top of the clathrin basket, i.e. "butting" up against the elastic clathrin basket. Assuming the minus end of the actin filament anchors to the cell membrane via Sla2, the plus end then polymerizes upward and ratchets against the cell membrane. The asymmetry between anchoring at the minus end and ratcheting at the plus end provides a time-averaged force to invaginate the membrane further into the cell. Actin filament nucleation via Arp2/3 increases this force.

We, therefore, model the actin filament network as an applied force on the membrane localized at these Sla2 anchoring points. The magnitude of this force is related to the total number of actin filaments participating in the network, and this number has been computed based on a combination of experimental data and kinetic modelling [55, 56]. We use the final configuration of the emergent actin network to determine the force applied to the membrane. Given the observed tubular structure of the deformation, this actin force is assumed to be axisymmetric with constant components in the radial and $-z$ (downward) directions, i.e. $\vec{F}_{act} = F_\rho \vec{e}_\rho + F_z \vec{e}_z$. The actin force is imposed by adding a linear potential of the form $V_{act}(\rho, \varphi, z) = -(F_\rho \rho + F_z z)$ to the energy for the part of the membrane to which the force is locally applied. The energy functional for the elongation stage is

$$\begin{aligned} E_{elong} = E_{init} + \int d\vec{r}\, [V_{act}(\rho, \varphi, z)\, g(\rho, \varphi, z) \\ + V_{ster}(\rho, \varphi, z) + V_{pin}(\rho, \varphi, z)], \end{aligned} \tag{2.3}$$

where $g(\rho, \varphi, z) = 1$ for the region over which the actin force is applied and zero otherwise. To distinguish between Proposals 1, 2, and 3, we explore different anchoring regions and different ratios of the force components. Note also that $V_{ster}(\rho, \varphi, z < 0) = \infty$ for $\rho > R_{ap}$ and zero otherwise. This models the accumulation of the yeast actin cytoskeleton just beneath the cell membrane and near the tubular invagination as it emerges [43, 57]. The $\rho > R_{ap}, z > 0$ region acts as a "reservoir" for tube growth. We, therefore, impose an additional quadratic potential, $V_{pin}(\rho, z) = \frac{1}{2}\beta z^2$ for $\rho > R_{ap}$, where β is chosen so that the membrane outside this region remains flat.

Pinchoff stage: Experiments indicate that the BAR proteins dominate in this last stage, *after* the tubular-like deformation forms [39, 51]. This observation is rather perplexing since BAR proteins, which themselves are curved, can, sense and generate spontaneous curvature in the cell membrane [58]. In other words, why does actin play the dominant role in generating the tubular-like deformation and not the BAR proteins? We suggest that once a tubular-like deformation occurs, the BAR proteins surround and confine the tube-plus-actin filament network near the top of the invagination site (see Fig. 2.2(d)) to stop actin polymerization. The BAR proteins only sense curvature here, not generate it. Since actin polymerization is driven by a ratcheting effect in a spatially fluctuating membrane, when these spatially fluctuations are supressed, actin polymerization stops. When the polymerization stops, no more membrane material can become part of the tube. In other words, the membrane tube area remains constant. With the BAR proteins confining the top part of the actin filament network against the membrane to couple the network to the membrane, we introduce an additional energetic term to the system. Now that the actin network has developed, we model it as an underlying elastic network of springs. Because the actin network is now connected to the membrane (as opposed to ratcheting against it in the elongation stage), the filament tips of the spring network depends on the configuration of the membrane. As with any elastic network coupled to a fluid membrane, the BAR protein-plus-actin filament contribution to the energy of a now cylindrical membrane is [59]

$$E_{BAR+actin} = \sum_{<i,j>} \frac{\mu}{2}[\vec{r_i} - \vec{r_j}]^2, \tag{2.4}$$

where μ is the spring constant and i, j denotes the meshwork coordinates of the springs on the surface of the membrane. Since the tube has now been formed, we will study a cylinder membrane described by Eq. (1) with this additional energy, $E_{BAR+actin}$. This energy will turn out to raise the surface tension of the membrane. This calculation will also suggest a new pearling instability pinch-off mechanism for endocytosis in yeast.

Methods: We utilize both analytical and numerical techniques to study the above model. On the numerical side, we use simulated annealing Monte Carlo (MC) simulations to identify low-energy structures, see Appendix C. In our simulations we represent the membrane using standard techniques for constructing discrete surface triangulations [60]. The discrete version of the bending energy in Eq. (2) is then implemented using expressions introduced by Brakke[61]. The mean curvature at vertex i is given as a $H_i = \frac{1}{2}\frac{\mathbf{F}_i \cdot \mathbf{N}_i}{\mathbf{N}_i \cdot \mathbf{N}_i}$ with $\mathbf{F}_i$ being the gradient of area and $\mathbf{N}_i$ being gradient of volume calculated with respect to the coordinates of vertex i. The bending energy is then given as $E_{bend} = (H - C_0)^2 A_i/3$, where A_i is the total area of triangles sharing vertex i. The spontaneous curvature C_0 is chosen according to the region of the membrane to which the vertex belongs. Surface tension is computed as an energy penalty to change the reference area of the membrane. Reference area A_0 is chosen to be that of the initial flat configuration. The energy associated with changes of the surface area is then $E_{surface} = \sigma\,|A - A_0|$, where A is the area associated with a vertex and computed as one third of the sum of areas of all triangles sharing that vertex.

To ensure that we simulate a fluid membrane, each MC step involves two steps [60]: *i*) displace a vertex in a direction chosen at random uniformly from a cube $[-0.05l_0, 0.05l_0]^3$, where l_0 is the average edge length of the initial triangulation, and *ii*) flip an edge on a rhombus. This flip removes an edge shared by two triangles and reconnects it so that it spans the opposite, previously unattached, vertices [62, 63]. Moves are accepted or rejected according to the Metropolis algorithm. The sweeps are continued until the total energy does not change with some prescribed precision. Different random number generator seeds are used to ensure the reproducibility of the lowest energy configurations. A typical run with $N_v \approx 3.5 \times 10^3$ vertices consists of $\sim 10^6$ MC sweeps, with a sweep consisting of attempted moves of each vertex and attempted flips of each edge. Any moves or edge flips leading to unphysical self-intersection of the triangulation are rejected. This is achieved by endowing each vertex with a hard core of diameter $b = 0.9l_0$, and each edge with a tethering potential [60] with maximum length $l_{max} = 1.4l_0$ such that $l_{max}/b \approx 1.55$. These values are chosen in accordance with Refs. [64, 65] to be tight enough to prevent edge crossings but still allow edge-flips, thus ensuring fluidity. Finally, the actin forces are applied to the vertices.

2.3 Results

2.3.1 Initiation stage with clathrin

To analyze the equilibrium shapes of the membrane in the initiation stage, we use the Monge representation such that each coordinate on the membrane in three-dimensional space is parameterized by two planar coordinates x and y with $\vec{r} = (x, y, z(x, y))$. We then assume axial symmetry so that $\vec{r} = (r, \theta, z(r))$. In the small gradient approximation Eq. (2) simplifies to (see Appendix D):

$$\begin{aligned} E_{init}[z(r)] \approx \sum_{i=1,2} \int_{R_{i-1}}^{R_i} & \pi \kappa_i r \big[(\Delta z)^2 - 4C_{0i} \Delta z \\ & + \left(2C_{0i}^2 + \frac{\sigma_i}{\kappa_i} \right) (\nabla z)^2 + \left(4C_{0i}^2 + 2\frac{\sigma_i}{\kappa_i} \right) \big] dr \\ & + \sum_{i=1,2} \int_{R_{i-1}}^{R_i} 2\pi \kappa_{G_i} \left(\frac{dz}{dr} \frac{d^2 z}{dr^2} \right) dr \\ & + \sigma_0 \left(2\pi \int_0^{R_1} \left(1 + \frac{1}{2} (\nabla z_1)^2 \right) r dr - A \right) \\ & + \gamma 2\pi R_1, \end{aligned} \tag{2.5}$$

where A is the area of domain 1 (the Sla1/Ent1/2 bound component which is attached to the clathrin basket), and σ_0 is a Lagrange multiplier introduced to fix the area of domain 1. We have also introduced a line tension γ at the interface between the two components—the bare component and the Sla1/Ent1/2 bound component (Ent1/2 are the yeast homologues for epsin in mammalian cells). Finally, the radial coordinate of the interface is denoted by R_1, while R_2 denotes the outer edge of the membrane. We neglect the turgor pressure for now and address it towards the end of this subsection.

We now proceed with the variation of the Lagrangian, $\delta E_{init}\left[z\left(r\right)\right] = \delta \int_0^{R_1} \mathcal{L}_1 dr + \delta \int_{R_1}^{R_2} \mathcal{L}_2 dr = 0$ (see Appendix D). As for boundary conditions we demand that membrane be continuous at the interface between the two components so that $z_1(R_1) = z_2(R_1) = z(R_1)$. In addition, the membrane cannot have ridges for the bending energy to remain finite so that ${z_1}'(R_1) = {z_2}'(R_1) = z'(R_1)$. For $R_2 \to +\infty$, we have $z_2(R_2) = 0$ so that ${z_2}'(R_2) = 0$. The radial symmetry demands that ${z_1}'(0) = 0$. With these conditions, $\delta z_1, \delta z_2, \delta R_1, \delta z'(R_1)$, and $\delta z_1(0)$ are free variables, so the energy is minimized by solving the following equations:

$$\frac{\partial \mathcal{L}_1}{\partial z_1} - \frac{d}{dr}\frac{\partial \mathcal{L}_1}{\partial {z_1}'} + \frac{d^2}{dr^2}\frac{\partial \mathcal{L}_1}{\partial {z_1}''} = 0 \tag{2.6}$$

$$\frac{\partial \mathcal{L}_2}{\partial z_2} - \frac{d}{dr}\frac{\partial \mathcal{L}_2}{\partial {z_2}'} + \frac{d^2}{dr^2}\frac{\partial \mathcal{L}_2}{\partial {z_2}''} = 0 \tag{2.7}$$

$$\begin{aligned} &\left[\mathcal{L}_1 - {z_1}'\left(\frac{\partial \mathcal{L}_1}{\partial {z_1}'} - \frac{d}{dr}\frac{\partial \mathcal{L}_1}{\partial {z_1}''}\right) - {z_1}''\frac{\partial \mathcal{L}_1}{\partial {z_1}''}\right]\Bigg|_{r=R_1} \\ = &\left[\mathcal{L}_2 - {z_2}'\left(\frac{\partial \mathcal{L}_2}{\partial {z_2}'} - \frac{d}{dr}\frac{\partial \mathcal{L}_2}{\partial {z_2}''}\right) - {z_2}''\frac{\partial \mathcal{L}_2}{\partial {z_2}''}\right]\Bigg|_{r=R_1} \end{aligned} \tag{2.8}$$

$$\left[\left(\frac{\partial \mathcal{L}_1}{\partial {z_1}'} - \frac{d}{dr}\frac{\partial \mathcal{L}_1}{\partial {z_1}''}\right) - \left(\frac{\partial \mathcal{L}_2}{\partial {z_2}'} - \frac{d}{dr}\frac{\partial \mathcal{L}_2}{\partial {z_2}''}\right)\right]\Bigg|_{r=R_1} = 0 \tag{2.9}$$

$$\left[\frac{\partial \mathcal{L}_1}{\partial {z_1}''} - \frac{\partial \mathcal{L}_2}{\partial {z_2}''}\right]\Bigg|_{r=R_1} = 0 \tag{2.10}$$

$$\left(\frac{\partial \mathcal{L}_1}{\partial {z_1}'} - \frac{d}{dr}\frac{\partial \mathcal{L}_1}{\partial {z_1}''}\right)\Bigg|_{r=0} = 0. \tag{2.11}$$

Solving Eqs. (6) and (7) leads to

$$\begin{aligned} z_1(r) &= c_1 + c_2 \log(r) + c_3 I_0(r\xi_1) + c_4 K_0(r\xi_1) \\ z_2(r) &= c_5 + c_6 \log(r) + c_7 I_0(r\xi_2) + c_8 K_0(r\xi_2), \end{aligned} \tag{2.12}$$

where $\xi_1^2 = 2C_{01}^2 + \dfrac{\sigma_1 + \sigma_0}{\kappa_1}, \xi_2^2 = 2C_{02}^2 + \dfrac{\sigma_2}{\kappa_2}$, and I_0 and K_0 denote the zeroth order modified Bessel functions of the first and second kind. We can then use Eqs. (8) through (11) and the boundary conditions to determine these 8 coefficients and σ_0, R_1.

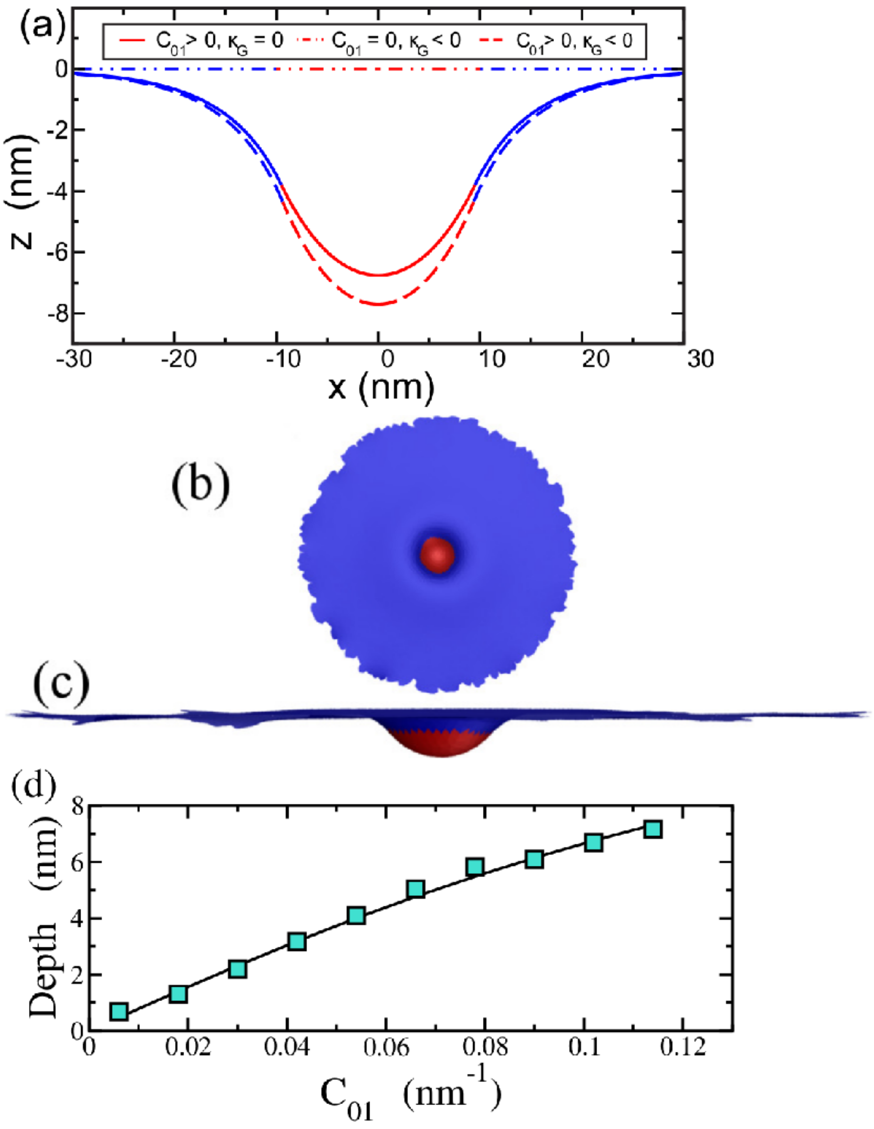

FIGURE 2.4: (a) Cell membrane profile, or $z(x, y = 0)$, for the parameters stated in the text. The red (medium grey) denotes the clathrin-bound part of the membrane, while the blue (dark grey) denotes the bare membrane. (b) Top view of the two-component membrane model using simulated annealing Monte Carlo methods. (c) Side view of the same configuration. Both images have been rescaled accordingly for presentation purposes. (d) Comparison of the maximum depth (or depth) obtained from the numerical simulation (symbols) with the analytical solution (line) for the intiation stage. All the parameters, except for the varying C_{01}, are the same as the $\kappa_G = 0$ curve in Fig. 2.4a.

For typical parameters for the two-component membrane we use $\kappa_1 = 20\ k_BT$ [66], $\kappa_2 = 10\ k_BT$ [54], $C_{01} = 0.1\ nm^{-1}$ [67], $C_{02} = 0$, $\kappa_{G1} = -0.83\kappa_1$ [68], $\kappa_{G2} = -0.83\kappa_2$, $\sigma_1 = 0.18\ k_BT/nm^2$ [69], $\sigma_2 = 0.18\ k_BT/nm^2$ [69], $A = \pi 100\ nm^2$, and $\gamma = 3\ k_BT/nm$ [70]. Given these parameters, the equilibrium shape of the membrane is plotted in Fig. 2.4a. We see that a dimple emerges due to clathrin binding. This dimple finalizes the initiation stage of endocytosis in yeast and sets the radius of the imminent tubular invagination.

Fig. 2.4a contains two additional curves to assess the effect of non-zero Gaussian rigidity κ_G. Prior work has found that differences in κ_G across a boundary can drive tube formation in membranes [71]. We find, given the above parameters, that it is the non-zero spontaneous curvature that instead drives the dimple formation. More precisely, for $C_{01} = 0$, no dimple forms and for non-zero C_{01} and κ_G, the depth of the dimple is enhanced only by about 14 percent.

Before concluding this subsection, we must point out that our method differs from an earlier two-component "dimple" analysis [72]. First of all, Ref. [72] does not take into account the $C_{01}^2(\nabla z)^2$ term [73], which is needed for consistency in the small gradient expansion. Second, we take into account non-zero κ_G because $\kappa_1 \neq \kappa_2$. Thirdly, to solve for some of the coefficients, the earlier work imposes mechanical equilibrium conditions, as opposed to implementing boundary conditions in the variation of the Lagrangian directly.

Let us now address the presence of turgor pressure. Previous models use anywhere from 10^3 Pa [42, 51] to 10^5 Pa [52] since the turgor pressure at an endocytotic site has not been measured directly. The turgor pressure could be lowered locally by a release of osmolytes near the endocytotic site it as proposed in Ref. [52] based on experiments presented in Ref. [74]. For the above set of parameters, using a turgor pressure $p = 10^4$ Pa, the energy contribution from the turgor term is 20 percent of the total energy in the absence of the turgor pressure so that the depth of the dimple will decrease slightly. For $p = 10^3$ Pa, the turgor energy is only 2 percent of the total energy in the absence of the turgor pressure can be neglected, while for $p = 10^5$, a different parameter range would need to be explored, such as the nonzero value of the spontaneous curvature of the membrane whose effect will be described below. Of course, even in the absence of turgor pressure, a depth of 7.7 nm is small such that it may be difficult to measure given an EM pixel size of 2.53 nm [39]. The presence of 10^4 Pa turgor pressure further decreases this depth. Thus, the membrane may not be perfectly flat when the actin filaments begin to polymerize as speculated in [39].

We also conduct numerical minimization of the intiation stage (Figs. 2.4b and c). As a check on our simulations, we compare the maximum depth of the dimple, i.e. $|z_{max}(r)|$, as a function of C_{01}, for the analytical calculation with the numerical one in Fig. 2.4d. Here, each energy relaxation is performed starting from a flat configuration. We place a flat patch of radius $R_2 = 40 l_0$ on a hard plane parallel to the xy plane. We then assign spontaneous curvature C_{01} to all vertices in the central region of radius $r_{C_{01}} = 6 l_0$. We use the energy functional in Eq. (2) with an additional interfacial line tension. Fig. 2.4d shows the output of the simulation for the same parameters used in Fig. 2.4a, except with additional C_{01} values. We find very good agreement between the two. Note that since non-zero κ_G does not drive the dimple formation (for the parameters studied), we do not include it here.

2.3.2 Elongation stage via actin polymerization

Now that the initial small deformation due to Sla1/Ent1/2 binding the membrane to the clathrin basket is formed, the overall radius of the tubular invagination is set. The protein Sla2 next binds to and near the clathrin dimple. Only those Sla2 molecules bound near the top of the clathrin dimple also bind to the actin to form a ring-like structure of binding sites [7]. Since the clathrin dimple is elastic-like, it impedes motion of the Sla2 molecules near the top of the clathrin dimple such that these Sla2 binding sites provide for an anchoring of the actin filaments to the membrane to which a localized force can be exerted. As the actin filaments polymerize, the interaction of the polymerizing actin filament tips with the membrane is much more dynamic than the anchoring points since actin filaments polymerize via a ratcheting effect. The membrane just provides a constraint for the growing filament tips to ratchet against along the length of the tube. This asymmetry in the force is needed for a deformation (other than due to a random fluctuation) to occur. So we model the effect of the anchored at one end, and polymerizing at the other, actin filaments as a localized force on the membrane via the potential V_{actin}, as indicated in Eq. (3). In addition, the steric potential V_{ster} models the accumulation of the yeast actin cytoskeleton just beneath the cell membrane and near the tubular invagination as it emerges [43, 57].

How large is this force? An estimate may be obtained from quantitative confocal microscopy measurements of 16 fluorescently labelled proteins involved in endocytosis in fission yeast [55]. The mean peak for the number of G-actin molecules (monomeric actin) is approximately 7500. Assuming all of these molecules polymerize to form actin filaments of about 100 nm in length [56] and each G-actin molecule is 2.7 nm in length (5 nm in diameter) then each filament contains about 40 molecules. About 200 actin filaments would then be formed. Each actin filament contributes approximately 1 pN of force, since the stalling force of an individual actin filament is approximately 1 pN [75]. The total force is then approximately 200 pN, which is applied to the anchoring region of the actin filaments. Since we do not take into account dynamics explicitly, we will merely implement the final value of the total force rather than increasing the force as the actin network develops. In the quasistatic limit the two approaches should be equivalent.

We now turn to the direction of the actin polymerization force and review the three different proposals for the actin filament orientation [43, 44, 51]. As shown in Fig. 2.2, actin filaments polymerize “upward” and branch via Arp2/3 to drive the membrane further into the interior of the cell. In Proposal 1, the force is predominantly downward, as opposed to radially inward, provided the initial actin filaments are aligned less than 45 degrees to the normal of the undeformed membrane. Assuming the orienation of the anchored actin filaments stays relatively fixed as branched actin filaments are generated, then the magnitude of the total actin force increases, whilst remaining fixed in direction. Here we assume axial symmetry so that there are only two non-zero components of the total force.

How do the competing Proposals 2 and 3 compare with Proposal 1? In Proposal 2 the actin network grows inward from the outerlying cytoskeleton towards the invagination site. The actin network is anchored to the outerlying cytoskeleton, as opposed the cell membrane, via Sla2. If we assume a purely radially inward force then the membrane will not deform into a tube with the observed length-to-radius ratio of approximately 10. The branched structure of the actin network, however, can provide a downward component to the total force to elongate the tube (Fig. 2.3a). We, therefore, distinguish Proposal 1 as a case where the downward component of the total polymerization force is smaller than the radially inward component, whilst in Proposal 2, it is the reverse.

Proposal 3 assumes that there are two anchoring zones for actin filaments—one towards the bottom of the emerging tube and another one near the top of the tube. From these two anchoring zones emerge two actin networks simultaneously growing towards each other and, thus, repelling each other since the actin filaments cannot interpenetrate (Fig. 2.3b). It is this repulsion that presumably elongates the tube. Coexistence of a downward force component and an upward force component, however, demands that the membrane simply stretches like a rubber band with no new cell membrane material being added to the tube. Because the cell membrane is bending dominated (and not stretching dominated), Proposal 3 would presumably lead to rupture of the tube [76]. It is not as likely that Proposal 3 contributes to membrane tube formation and we do not study it further as an elongation mechanism.

So we focus on Proposals 1 and 2 for the elongation stage by promoting them to Models 1 and 2, respectively, and study them quantitatively. To gain some insight, we first review a slightly simpler model, again, first in the absence of turgor pressure. Consider a bare (one-component) membrane with downward force F applied just to the origin, as opposed to being applied over an extended region of the membrane [77]. Assume the membrane has bending rigidity κ and surface tension σ. For a cylindrically shaped membrane with a length L and radius R, surface tension favors reducing the radius of the cylinder/tube, while bending favors a larger radius. Upon minimizing the energy, one obtains an equilibrium radius of $R_{eq} = \sqrt{\kappa/2\sigma}$ and an equilibrium force of $F_{eq} = 2\pi\sqrt{2\sigma\kappa}$. For forces less than F_{eq}, the membrane deformation is a wide-necked depression and reaches some equilibrium depth that depends on the force, while for forces greater than F_{eq} there is a first-order transition to a cylindrical shape of arbitrary length. Simulations of the membrane shape equation indicate that there is a force barrier from the wide-necked depression to cylinder formation that is 13 percent larger than F_{eq} [77]. Barriers are a characteristic signature of first-order transitions. Monte Carlo simulations of pure downward pulling on a membrane over an extended region (as opposed to a single point) support this scenario with the force barrier increasing linearly with the size of the region over which the force is exerted [78].

Now consider Models 1 and 2 with an additional radially inward force and a steric interaction between the membrane and the actin. To begin, we expect the radially inward force to increase the force barrier to arbitrarily long cylindrical formation. We also expect the steric interaction to alter the transition since R_{ap} cuts off the wide-neck depression and makes it easier to cross-over to long cylinder formation. More specifically, we expect that as R_{ap} decreases, the change from non-cylindrical to cylindrical occurs at a lower applied force. This effect has been observed in Monte Carlo simulations of driving fluid vesicles through a pore [79].

To test these notions we study the extension-force curve of tube/cylinder formation for the various models. We do so numerically because V_{act} (Eq. (3)) is a potential localized to a particular region of the membrane, which would be difficult to handle analytically. We first apply a purely downward force to a ring of vertices right above the Sla1/Ent1/2 attached part of the membrane. We dub this model, Model 0. The magnitude of the total force is denoted by F_t and is distributed uniformly among the vertices. Since $\kappa_1 = 10\ k_bT$ and $\sigma = 0.18 k_B\ T/nm$, $F_{eq} \approx 49\ pN$(for the applied point force). To numerically determine F_{eq0}, the F_{eq} equivalent for Model 0, we pull on the ring with initially 50 pN of total force, F_t, and $R_{ap} = 15\ nm$. We then reinitialize F_t to take on smaller values and look for the F_t at the boundary between tubes becoming shorter and tubes becoming longer. We find that $F_{eq0} \approx 25\ pN$ using this algorithm. To study the force barrier, we find that deformations for $F_t < 30\ pN$ are reasonably robust to perturbations (stepping F_t up and back down again) such that 30 pN is a lower bound for the barrier. See Fig. 2.5b.

We now add a radially inward force component to the force applied to the ring of vertices to address Models 1 and 2. How does this radially inward modify the shape crossover due to the downward component of the force? For a purely radially inward force applied to the ring of vertices, the membrane will pucker inward where the force is applied and no cylindrical tube will form. The additional radially inward force increases the force barrier to long tube formation. In Model 1 the actin filaments are anchored at the bottom of the tube so that the downward component of the force is larger than the radially inward component. We assume that $\vec{F_t} = \sqrt{2/3}F_t\vec{e}_z + \sqrt{1/3}F_t\vec{e}_r$, which would correspond to actin filaments anchoring at an angle of approximately 35 degrees with respect to the normal of the flat part of the membrane. In Model 2 the radially inward component of the actin polymerization force is larger than the downward component, so we choose $\vec{F_t} = \sqrt{1/3}F_t\vec{e}_z + \sqrt{2/3}F_t\vec{e}_r$.

Fig. 2.5c depicts the depth-versus-total force curve for both models as well as two membrane configurations for Model 1. The tubes are reasonably robust to perturbations for all forces studied suggesting that the cross-over to long cylinders is not made. Even though the downward component of the force is increased, it is not enough to overcome the increasing force barrier introduced with the increasing radially inward force as well. For large enough radially inward forces, the tube depth begins to decrease resulting in a nonmonotonic depth-versus-total force curve. As the contribution of the radially inward force increases, it is energetically more favorable for the membrane to deform inward as opposed to elongate. Fig. 2.5d depicts two equilibrium configurations for Model 1. For the values of R_{ap} studied, $12 - 18$ nm, the tube depth increases only by several percent with increasing R_{ap}. In other words, the applied force clearly plays the dominant role.

Now on to Model 2. All tubes are reasonably robust to force perturbations, just as in Model 1, and the depth-versus-total force curve is also not monotonic. The largest depth of the membrane deformation for Model 2 is about 65 nm. While there is indeed some room to play with the ratio of the magnitude of the two components, we contend that Model 1 may better account for the range of observed tube depths [39]. Hindsight tells us that Model 1 would be more reasonable in obtaining longer tubes, but such depths could have been much longer than the observed ones. The nonmonotinicity suggests an optimal force of around 100 pN, should long tubes be the optimizing principle. And while Model 2 may not necessarily act as the initial driving force to elongate the tube, we address an important role for Model 2, and one aspect of Proposal 3, during the final stage of endocytosis.

To investigate the role of turgor pressure in Models 1 and 2, we find that as the turgor pressure increases to 10^3 Pa, our previous results are robust. However, for turgor pressures above this value, the depths of tubes (for a given total force) decrases. See Fig. 2.5c. So the presence of large turgor pressure biases Model 1 even more so. However, for $p = 10^4$ Pa, since the largest depth is approximately 55 nm, to account for larger observed depths, one can invoke the presence of myosin I to allow for extra downward force to increase the depth of the tube [80, 81]. Myosin I bind the membrane to the actin filaments. It has been estimated that there are approximately 300 myosin I molecules at each endoyctotic site, each exerting 2 pN of force [82] (assuming myosin I carry the same force generation potential as myosin II) to arrive at a maximal downward force of

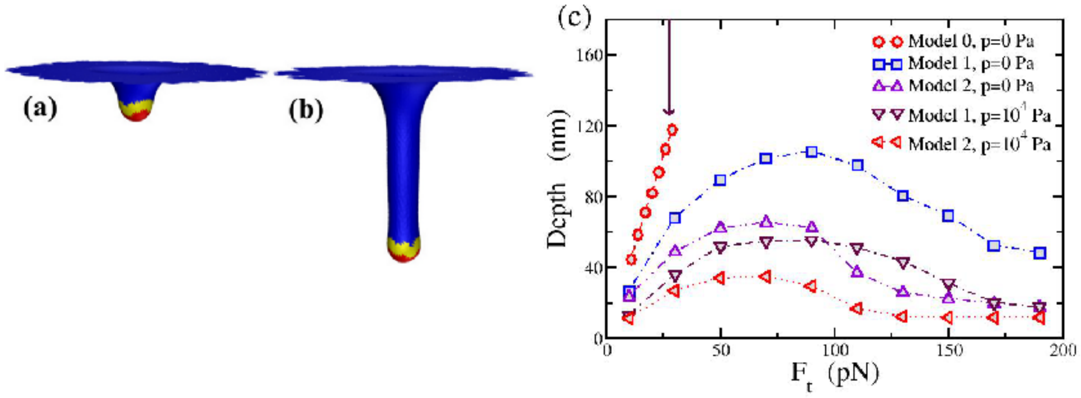

FIGURE 2.5: (a) Simulation results for Model 1 with total applied force $F_t = 10\ pN$. The total force is applied to only the yellow (light grey) part of the membrane (at the vertices). Red (medium grey) denotes the Sla1/Ent1/2 bound part of the membrane and blue (dark grey) denotes the bare membrane. (b) Same as (a) except with $F_t = 50\ pN$; (c) Comparison of the depth as a function of F_t for three different models with zero and nonzero turgor pressure, p. Again, the error bar is of order the symbol size. The arrow pointing downward denotes the value of F_{eq} for reference .

600 pN. Such an additional downward force component would allow for long tubes even in the presence of larger ($10^4 - 10^5$ Pa) turgor pressures.

2.3.3 Pinch-off stage via the pearling instability

Experiments indicate that the BAR proteins enter in this last stage, *after* the actin filament network has formed [39, 51]. Yet many qualitative depictions of the process show the BAR proteins in between the membrane and the actin filament network [51]. BAR proteins have been shown to generate spontaneous curvature in membranes [58]. Since the BAR proteins enter after the tube has formed [39, 51], there is no need to generate spontaneous curvature, only sense it. We suggest a potentially new role for BAR proteins here beyond just sensing curvature. Once the tubular-like deformation via the actin filament network occurs, the BAR proteins surround and confine the tube-plus-actin filament network toward the top of part of the tube where bare membrane is exposed to the BAR proteins (Fig. 2.2d). By surrounding the actin filament network and suppressing the fluctuations of the bare membrane, actin polymerization stops since polymerization is driven by a ratcheting effect in spatially fluctuating fluid membrane (and by the entropically elastic actin network [83]). When actin polymerization stops, no more material can become part of the tube, and the membrane tube area remains constant.

Because BAR proteins confine part of the actin filament network it is now restricted to lie on the membrane. This effect will generate a new contribution to the membrane energy as indicated in Eq. (4), where the coordinates of the network are the coordinates of the membrane. The actin filament network is modeled as an elastic network with spring constant μ [59]. Since actin filaments are semiflexible polymers with a persistence length of about 20 μm, the elasticity comes from elasticity of the Arp2/3, the branching agent responsible for nucleating new filaments. The entropic angular spring constant for Arp2/3 is approximately 10^{-19} J/rad^2 [84], so for branches several actin monomers long, the entropic linear spring constant, $\mu \approx 10^{-2}\ N/m$, or 2.5 k_BT/nm^2. This additional elasticity contributes to the membrane surface tension with the effective membrane surface tension becoming $\sigma_{eff} = \sigma + \mu/2$, at length scales larger than the meshsize of the actin network.

How does this increase in surface tension affect the membrane+actin+BAR-protein system? We investigate configurations of a cylindrically shaped membrane with bending rigidity κ and increasing surface tension to answer this question. Could such an increase lead to destabilization of the cylindrically-shaped membrane? As the surface tension increases, a sinusoidal perturbation may perhaps lead to the cylindrical membrane breaking up into spherical droplets as surface tension favors spheres. This mechanism is otherwise known as the pearling instability [85, 86].

Is this instability relevant to the system at hand? Analytical analysis of this instability is included in the Appendix E to address this question. This analysis suggests that the pearling instability may be relevant to the system at hand given the physiological parameters. For the relevant range of wavevectors (less than 0.1 nm^{-1}), the cylinder is only stable when $\sigma R_o^2/\kappa < 2.39$, where $R_o = 8.71\ nm$, the original radius of the unperturbed cylinder and $\kappa = 10\ k_BT$. The length-to-radius ratio of the initial cylinder is 10. This inequality, however, depends on the strength of the perturbation.

To analytically investigate the pearling instability, the volume is assumed to be constant such that the turgor pressure is not important (see Appendix E). This constraint is imposed so that the membrane does not shrink to a point once the surface tension term dominates. While, indeed, the invagination is an open system so that the volume of the tube may change slightly, as long as the volume remains finite a pearling instability can set in for some range of parameters. Pearling instabilities have been experimentally observed in open tubes *in vivo* and *in vitro* [87, 88].

We implement numerical simulations to numerically test for this instability. We start an initial configuration of a triangulated capsule (as opposed to cylinder) with the above parameters and then vary σ. As indicated in Fig. 2.6, the pearling instability mechanism sets in once $\sigma R_0^2/\kappa$ is large enough. In this case, the surface tension must increase by an order of magnitude for the instability to set in. This increase by an order of magnitude is precisely the contribution of the $E_{act+BAR}$ term in the energy increasing the surface tension from $\sigma \simeq 0.1\ k_BT/nm^2$ to $\sigma \simeq 1\ k_BT/nm^2$!

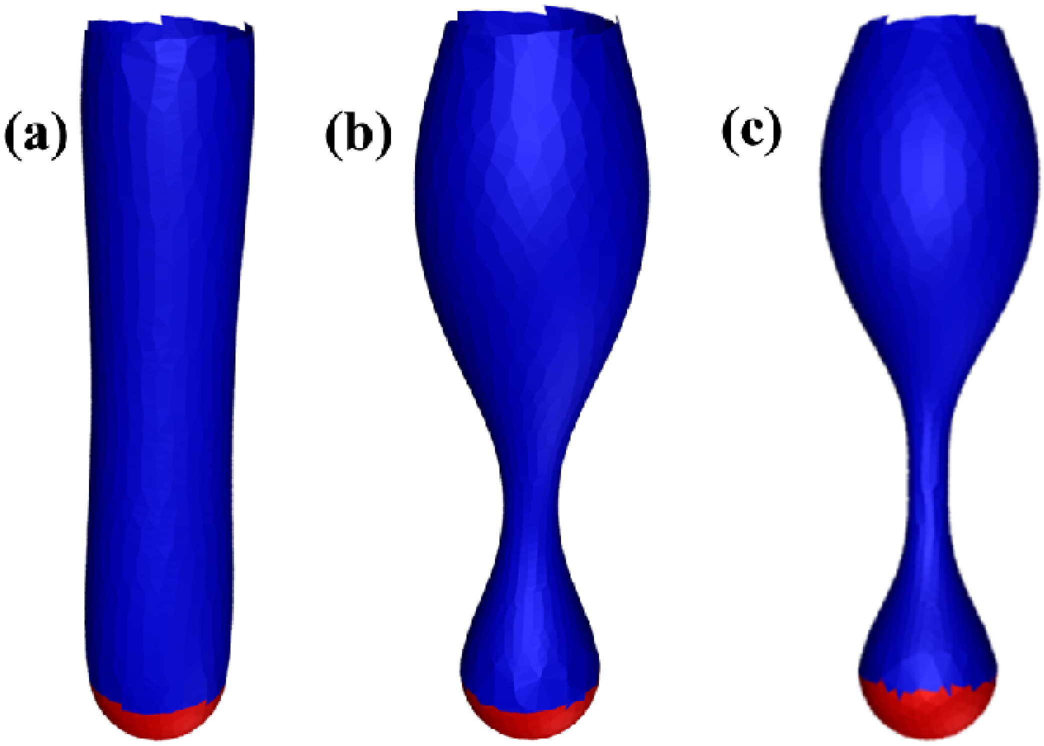

FIGURE 2.6: The pearling instability for a cylindrical membrane with increasing surface tension going from left to right, or $\sigma R_o^2/\kappa = 0.267, 2.67$, and 4.15 respectively. The top and red part of the tube are fixed.

Once the membrane breaks up into spheres, the spheres remain connected, as observed in experiments [85, 89]. This observation differs from the Rayleigh-Plateau instability, where the spheres do not remain connected. So how does the vesicle nearer to the interior of the cell break off from the upper part of the tubular membrane? The most natural answer would be via actin polymerization. Proposals 2 and 3 both provide mechanisms for some downward-directed actin polymerization on the vesicle to drive it further into the cell. In Proposal 2 actin filaments polymerizing inward from the surrounding actin cytoskeleton towards the invagination sites can facilitate break-off of the vesicle by making a comet tail behind it. Such an actin comet tail has indeed been observed in experiments [43]. In Model 3 anchoring regions of actin filaments to the membrane near the top of the invagination region, while elongation is occuring, could initiate downward actin polymerization. These filaments can then also drive the break off of the vesicle nearer to the interior of the cell from the "top" sphere. Both routes may be important for the final break-off of the vesicle.

2.4 Discussion and conclusion

We have developed and analyzed a quantitative three-stage model for endocytosis in yeast that is consistent with the experimental data [46]. We first built a model for the initial small membrane deformation due to clathrin indirectly binding to the membrane via Sla1/Ent1/2. We demonstrated that the Sla1/Ent1/2-bound domain initiates invagination of the membrane by forming a small depression, or dimple, to set the radius of the subsequent tubular invagination. This subsequent tubular invagination is driven by actin polymerization forces, which we model as an external force applied to the membrane. We found that of the three competing proposals in the literature for the orientation of the actin filaments in driving tube formation, one proposal (Proposal 1) [51] is most likely to account for the observed tubular lengthscales of the cell membrane in endocytosis in yeast [39]. For turgor pressures smaller than 10^3 Pa, our results predict the applied force that optimizes the length of the tube, where the largest length-to-radius ratio is approximately 10. For turgor pressures larger than 10^3 Pa, myosin I, an actin motor that binds directly to the cell membrane so that it can enhance actin-dependent forces on the membrane, can potentially account for the large length-to-radius ratio [80]. The combination of this large ratio and the effective surface tension increases due to the presence of BAR proteins confining the actin filament network against the tubular cell membrane (Fig. 2.2d) naturally motivates that the pearling instability may assist in the scission mechanism. We showed that the pearling instability may promote spherical vesicle formation by both analytical calculations and simulations given the physiological parameters involved in endocytosis in yeast.

Let us contrast our model with an earlier model for endocytosis in yeast [42, 51]. In the latter, the coordinated effect of protein-induced lipid phase segregation along the tubule plays a key role in vesicle scission. The phase separation between hydrolyzed and non-hydrolyzed PIP_2, a membrane-bound protein to which actin attaches, calls for a two-component fluid membrane and induces an interfacial line tension between the two components to drive pinch-off. The effect of actin in this model is to decrease the effective surface tension of the membrane, which makes it easier for the interfacial line tension to scission the membrane and is rather different than the effect of actin in our model. We, however, model the actin as an applied force and are able to generate tube formations as a result. The competing quantitative model is not able to generate tubes explicitly given the manner in which actin polymerization is incorporated into the model. We also demonstrate that the pearling instability could potentially facilitate pinch-off. The frequency of endocytosis in budding yeast, invaginating its total cell membrane surface in about 100 minutes [39], suggests that an instability, as opposed to coordinated effort involving lipid phase separation, would be useful. The observation that scission occurs at a range of invagination depths also favors an instability as opposed to a more regulated mechanism. Comparison with another recent model is rather difficult since this new model assumes that the cell membrane is an elastic membrane with a nonzero shear modulus rather than assuming the cell membrane is a fluid one [52]. The formation of tubes in elastic membranes is very different from the formation of tubes in fluid membranes, where there is no shear modulus.

While we have presented a quantitative model for endocytosis in yeast, how much of this story applies to endocytosis in mammalian cells? More spherical-like membrane deformations are generated in mammalian cells due to clathrin cage formation and the motor protein, dynamin, driving pinch-off? Many of the same proteins involved in yeast clathrin-mediated endocytosis (CME) are conserved in mammalian CME [6]. It could be that the presence of the turgor pressure in yeast makes clathrin cage assembly difficult, but clathrin basket assembly less difficult given the much smaller change in volume for the basket. Then it is up to the actin, etc. to finish the job. As some of our results depend on the strength of the turgor pressure, it would be good to measure it directly at an endocytotic site. There is also another route to endocytosis in mammalian cells via the CLIC/GEEC pathway, which does not require clathrin or dynamin, and forms more tubular deformations as observed in yeast [90]. The requirement for actin in mammalian CME has been less clear. Several new studies in mammalian cells provide support for an actin requirement in the invagination and late stages of CME [6]. On the other hand, a recent *in vitro* experiment with clathrin and dynamin suggest that these two proteins are sufficient to drive endocytosis in mammalian cells [91]. In light of this experiment, it would be interesting to revisit the modeling of endocytosis in mammalian cells [92]. It may also be useful to investigate how the modeling presented here can be extended to enveloped virus entry [93], extocytosis, and budding to form a more unified theoretical framework for cell membrane deformations used to transport material in and out of the cell.

Chapter 3

Mechanics of anisotropic spring networks

3.1 Motivation

The onset of rigidity in disordered spring networks has been studied as a model for elasticity in disordered materials. Such a model undergoes a phase transition from not-rigid to rigid at some critical fraction of springs (bonds) [15, 94–96]. Numerical simulations on a bond-diluted triangular lattice suggest that the transition is a continuous one with the percolating rigid cluster having a fractal dimension at the transition [17, 95]. To date, one of the few theoretical tools to analyze rigidity percolation is effective medium theory (EMT). In 1985, an effective medium theory was developed by Feng, Thorpe, and Garboczi analytically capturing the relationship between disorder and mechanical response in these systems in good agreement with numerical simulations [18, 19, 97].

We now extend this theoretical framework – the EMT and the numerical simulations – to a disordered spring network with anisotropy. Anisotropic networks abound in nature and man-made materials, and are an important class of soft matter. Consider, for example, an orientationally ordered, but spatially disordered, network made of liquid crystal elastomers. The interplay between the gel-sol transition and the isotropic-nematic transition in both synthetic and biological systems has been studied [98, 99]. Consider also a layered, but disordered, system of granular particles [100]. What are the macroscopic elastic properties of such a system? Some properties have been analyzed in the ordered case [101, 102], but the disordered case is more complex and has received less attention. Finally, the cytoskeleton, the filamentous scaffolding that provides most animal cells their shape and rigidity, can consist of rather oriented, cross-linked filaments such as in lamellipodia, the broad, thin protrusion at the leading edge of a crawling cell [103, 104].

While we focus on extending the analytical framework of effective medium theory to disordered linear spring networks with anisotropy, the rigidity transition in “super-elastic” anisotropic central-force networks has been studied in prior work by Roux and Hansen and Wang and Harris [105–107]. In these “super-elastic” networks, all bonds in a preferred direction are occupied with springs, and bonds in other directions have infinite rigidity with a probability p and a finite rigidity with a probability $1 - p$. In addition to determining the rigidity percolation threshold, the notion of splay rigidity, in which only rotational degrees of freedom are frozen out, and a mapping to a random resistor network for the bulk modulus is discussed [106]. Some of their results can be extended to the usual bond-diluted system that we study here. However, there remain open questions about the interplay between anisotropy and rigidity in these systems. In particular, one can ask how does the difference in the directional occupation probability of springs influence the mechanical response of the network, and how does this couple to the direction of the applied deformation?

To answer these questions, we investigate a triangular lattice based anisotropic bond-diluted network and study how the anisotropy in the occupation of the springs influences the ability of the network to bear stresses using an effective medium theory and numerical simulations.

3.2 Model

We begin with a fully ordered, but anisotropic network of springs arranged in a two-dimensional triangular lattice. The bonds are given an extensional spring constant α for springs in the x direction, and γ for springs making 60° and 120° angle to the x direction, i.e. having a y component. We then introduce disorder into the system by removing bonds along the x direction with probability $1-p_x$, where $0 < p_x < 1$, and bonds with a y component with probability $1-p_y$, where $0 < p_y < 1$. There are no spatial correlations between these cutting points in either case. This generates a disordered network with a broad distribution of spring lengths in either direction. When two springs intersect, there exists a cross-link preventing the two springs from sliding with respect to one another, but they can rotate freely without any energy cost.

We study the mechanical response of this disordered network under an externally applied strain in the linear response regime. For simplicity we set the rest length of the springs to unity. Let $\boldsymbol{r}_{ij}$ be the unit vector along the spring ij and $\boldsymbol{u}_{ij} = \boldsymbol{u}_i - \boldsymbol{u}_j$ be the deformation of this spring. For small deformations, the deformation energy can be written as follows:

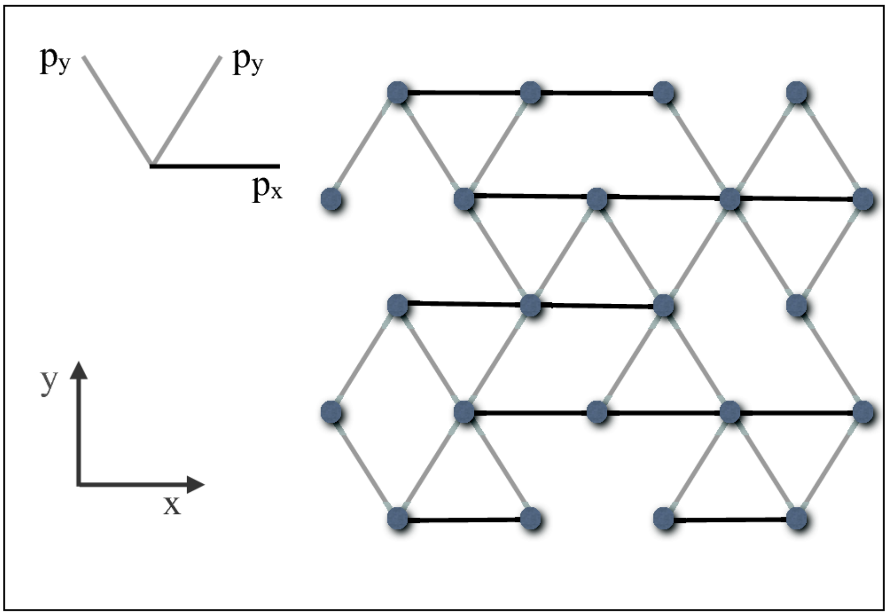

FIGURE 3.1: Schematic figure showing the randomly diluted anisotropic spring network with corresponding occupation probabilities p_x and p_y.

$$E = \frac{\alpha}{2}\sum_{\langle ij\rangle} p_{x,ij}\left(\boldsymbol{u}_{\alpha,ij}.\boldsymbol{r}_{\alpha,ij}\right)^2 + \frac{\gamma}{2}\sum_{\langle ij\rangle} p_{y,ij}\left(\boldsymbol{u}_{\gamma,ij}.\boldsymbol{r}_{\gamma,ij}\right)^2, \tag{3.1}$$

where $p_{x,ij}$ ($p_{y,ij}$) is the probability that the ij bond in the x (y) direction is occupied as shown in Fig.3.1 and a is the lattice spacing and is set to 1. The deformation energy corresponds to the cost of extension or compression of the springs. Although the model allows for anisotropy in disorder as well as in constitutive elasticity of the springs, we have set the bare elastic constant of both types of springs to have the same value ($\alpha = \gamma = 1$ in arbitrary units). We investigate the shear and bulk moduli of this disordered network as a function of the direction dependent occupation probability of springs in response to suitable strains imposed on the boundaries.

3.3 Methods and Analysis

3.3.1 Constraint counting argument and the rigidity threshold

We start with a constraint counting argument due to Maxwell [16, 18, 108], a very powerful and simple way to estimate at what occupation probability the phase transition takes place. Consider a d dimensional system with N particles or points, and hence Nd

degrees of freedom. The number of zero-frequency modes ($\phi N d$), where $0 < \phi \leq 1$, is equal to the number of degrees of freedom (Nd) minus the number of constraints, which in this case is $(\frac{1}{2}z_x N p_x + \frac{1}{2}z_y N p_y)$, where z_x is the number of nearest-neighbor points in the x direction and z_y is the number of nearest-neighbor points in the y direction. Here, $z_x = 2$ and $z_y = 4$. Hence, the fraction of zero-frequency modes is

$$\phi = 1 - (\frac{1}{2}p_x + p_y).$$

So the transition takes place when ϕ goes to zero or

$$\frac{p_x}{2} + p_y = 1.$$

In Fig. 3.2, we show the rigidity phase diagram of the disordered network, as a function of the occupation probability p_x and p_y of springs in the x and 60° and 120° to the x direction, respectively. We also show the network structure for three representative points in the rigid phase of the phase diagram: $p_x = 1$, $p_y = 1$, $p_x = 0.75$, $p_y = 0.90$, and $p_x = 0$, $p_y = 1$. In what follows we investigate how the mechanical response of the system changes as the network is progressively diluted, finally reaching the transition threshold. To accomplish this objective, we have used an effective medium theory and an energy minimization approach, which we describe below.

3.3.2 Effective Medium Theory

We study the mechanical response of this disordered network for small deformations using an effective medium theory [15, 18, 19, 97, 109]. The aim of the theory is to construct an effective medium or ordered network that has the same mechanical response as the depleted network under consideration. The effective filament stretching elastic constants are determined by requiring that strain fluctuations produced in the original, ordered network by randomly cutting filaments have zero average.

We first illustrate how the effective medium elastic constant can be calculated for the simple case where we apply a uniform strain on an isotropic central force network, so that all bonds are equally stretched by an amount $\delta\ell_m$ with effective medium spring constant α_m. Let us now replace a spring between two points, say, i and j by different one with spring constant α. It would lead to additional extension or compression of this spring, which we calculate as follows [18, 19].

The virtual force necessary to return i and j to their original positions before the replacement of the spring is $f = \delta\ell_m(\alpha_m - \alpha)$. If this force is now applied between i and j in the unstrained and ordered network, it will lead to a deformation δu of this spring

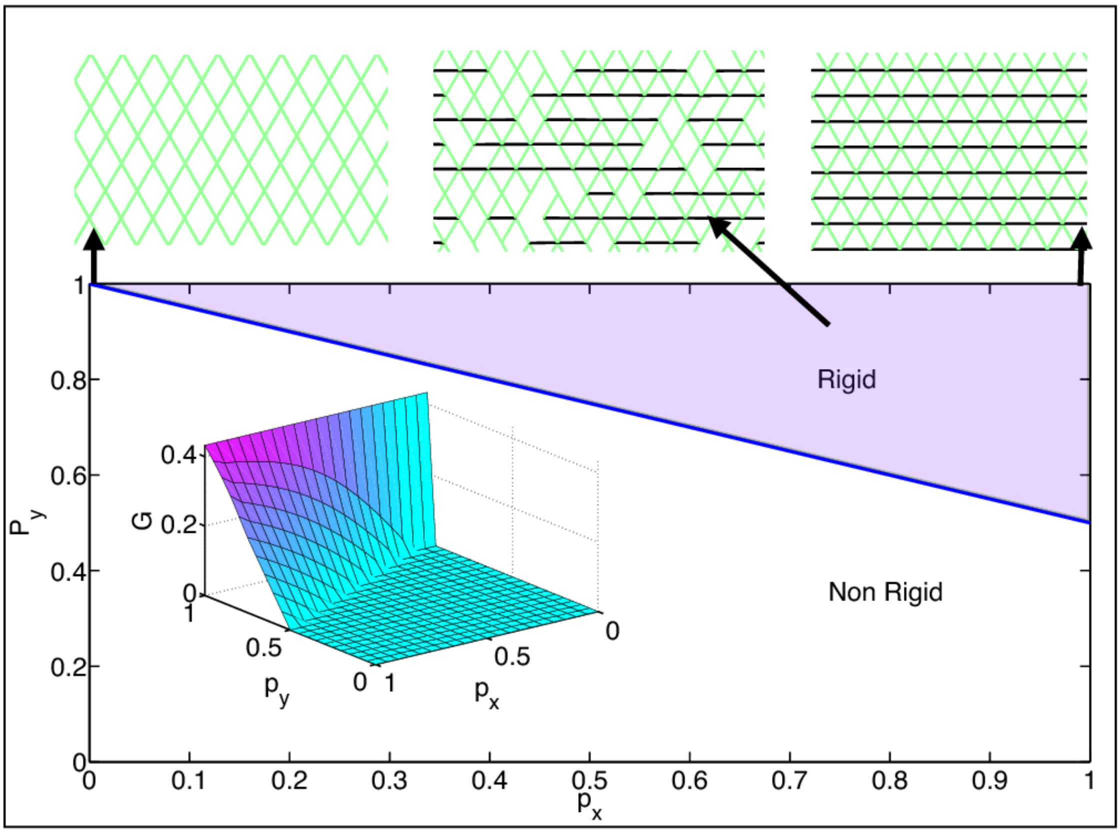

FIGURE 3.2: Plot of the phase diagram according to mean field constraint counting argument, with the inset showing the shear modulus G as a function of p_x and p_y obtained from the EMT in units of γ (set to unity) and the horizontal lattice spacing (set to unity). Different lattice realizations are also shown.

given by $f/\delta u = \alpha_m/a^*$. The effective spring constant $\alpha_{eff} = \alpha_m/a^*$ takes into account, through the dynamical matrix, the elasticity of the entire network including the direct connections between these points. If the force f is applied now on an unstrained network where the spring between i and j has been replaced by a spring with stretching constant α, $f/\delta u = \alpha_{eff} = \alpha_m/a^* - \alpha_m + \alpha$. Therefore change or fluctuation δu of the bond between i and j is given by

$$\delta u = \delta \ell_m \frac{\alpha_m - \alpha}{\alpha_m/a^* - \alpha_m + \alpha}. \tag{3.2}$$

It follows from the superposition principle that this fluctuation δu is the same as the extra extension or compression in the strained network due to the replacement of the bond ij. Considering random bond dilution in the network and defining an effective medium such that the fluctuations δu should vanish when averaged over the entire network,

$$\langle \delta u \rangle = 0. \tag{3.3}$$

For a distribution of bonds $P(\alpha') = p\delta(\alpha'-\alpha)+(1-p)\delta(\alpha')$, with p being the probability that a bond is present, the effective medium spring constant α_m is given by:

$$\frac{\alpha_m}{\alpha} = \frac{p-a^*}{1-a^*}, \tag{3.4}$$

with $a^* = \frac{2}{Nz}\sum_q Tr\left[\boldsymbol{D}(q)\boldsymbol{D}^{-1}(q)\right] = 2/3$ for a central force network [18].

Now let us consider an anisotropic network where the spring constant and probability of occupation for springs in the x direction (α, p_x) and springs making 60° and 120° angles with the x direction (γ, p_y) are different as described in Eq. 3.1. We decompose the triangular lattice system into two interconnected subsystems as shown in the schematic (Fig.3.1) and calculate the stretching forces and strain fluctuations $\boldsymbol{u}_\alpha$ and $\boldsymbol{u}_\gamma$ for these two subsystems separately. For small deformations, the restoring forces on the springs are given by:

$$\begin{aligned} \boldsymbol{F}_{\alpha,ij} &= \alpha_m \sum \boldsymbol{u}_{\alpha,ij}\cdot\boldsymbol{r}_{\alpha,jk}\,\boldsymbol{r}_{\alpha,jk} \\ \boldsymbol{F}_{\gamma,ij} &= \gamma_m \sum \boldsymbol{u}_{\gamma,ij}\cdot\boldsymbol{r}_{\gamma,jk}\,\boldsymbol{r}_{\gamma,jk} \end{aligned} \tag{3.5}$$

The x and y components of the deformation can be written as $\boldsymbol{u}_{\alpha,\gamma}(q) = -\boldsymbol{D}^{-1}(q)\boldsymbol{F}_{\alpha,\gamma}(q)$, where $\boldsymbol{D}(q)$ is the dynamical matrix [18] of the fully ordered lattice. Following the procedure for the isotropic network discussed above, we can calculate strain fluctuations in the depleted network, and effective medium elastic constants α_m and γ_m by demanding that the strain fluctuations vanish when averaged over the entire network. Since we consider uncorrelated distributions of the elastic constants α and γ, the effective medium elastic moduli α_m and γ_m are given by

$$\begin{aligned} \frac{\alpha_m}{\alpha} &= \frac{p_x-a^*}{1-a^*} \\ \frac{\gamma_m}{\gamma} &= \frac{p_y-b^*}{1-b^*}, \end{aligned} \tag{3.6}$$

above the rigidity percolation threshold, and $\alpha_m = \gamma_m = 0$ below, with p_x and p_y at the threshold obeying the constraint condition $p_y + p_x/2 = 1$ as discussed earlier. The geometric constants a^* and b^* represent the whole network contribution to the effective spring constants α_m/a^* and γ_m/b^* of the bonds. When the network is strained springs in the y direction will contribute to the elasticity in the x direction and vice versa due to the coupling between the two-sublattices accounted for by a^* and b^*. They are given by:

$$\begin{aligned} a^* &= \frac{2\alpha_m}{N z_\alpha} \sum_q Tr\left[(1-e^{-ia\boldsymbol{q}.\boldsymbol{r}_{\alpha,ij}})\boldsymbol{r}_{\alpha,ij}\boldsymbol{r}_{\alpha,ij}\boldsymbol{D}^{-1}(q)\right] \\ b^* &= \frac{2\gamma_m}{N z_\gamma} \sum_q Tr\left[(1-e^{-ia\boldsymbol{q}.\boldsymbol{r}_{\gamma,ij}})\boldsymbol{r}_{\gamma,ij}\boldsymbol{r}_{\gamma,ij}\boldsymbol{D}^{-1}(q)\right]. \end{aligned} \tag{3.7}$$

The sum is over the first Brillouin zone and $z_{\alpha,\gamma}$ are coordination numbers, and $\boldsymbol{r}_\alpha$ are unit vectors along bonds with spring constants α, i.e. bond that were originally along the x direction, while $\boldsymbol{r}_{\alpha,\gamma}$ are unit vectors along bonds with spring constants α, γ in the original undeformed lattice. The above definition of a^* and b^*, together with fact that in the fully ordered triangular lattice network, $1/3$ of all the bonds have a spring constant α and $2/3$ of the bonds by spring constants γ lead to the constraint condition: $\frac{1}{3}a^* + \frac{2}{3}b^* = \frac{2}{3}$. At the rigidity percolation threshold, $a^* = p_x$ and $b^* = p_y$, and thus $\frac{p_x}{2} + p_y = 1$, in agreement with the Maxwell constraint counting. We obtain the effective medium spring constants α_m and γ_m by solving equations (3.6) and (3.7) simultaneously. These elastic constants describe an ordered network that has the same mechanical response as the original depleted network, and can be used to calculate the shear and bulk moduli of the latter as discussed in Section IV.

3.3.3 Numerical Simulations

Simulations are conducted on the triangular lattice with system size $N_x = N_y = 128$ (shown unless otherwise specified). The network is initialized by adding bonds in the x direction with probability p_x, and the bonds with a y component with probability p_y.

Since the model system is anisotropic, there exist more than one shear modulus. We calculate the following shear response: a shear deformation is applied to two fixed boundaries along the x direction with strain magnitude $\epsilon = 1\%$, while the other two boundaries are periodic. Our simulations suggest that the mechanical response of the network may be reasonably approximated by linear response at such strains. Then the network is relaxed by minimizing the total energy of this system using the conjugate gradient method [110] allowing the deformation to be fully propagated. Eventually a minimum energy state is be found within the tolerance 10^{-8} with energy E_{min}. Then the shear modulus is calculated by $G = \frac{2E_{min}}{A_{unit}N_xN_y\epsilon^2}$,where $A_{unit} = \frac{\sqrt{3}}{2}$, denoting the area of one unit cell with unit bond length. Sample averaging is performed over 10 runs typically.

For the measurement of bulk modulus, a small ($\epsilon = 2\%$) uniform strain is applied to all four fixed boundaries. Once the system energy is minimized, we calculate the energy E_{box} from part of the network within a box in the center of the system with box size

$N'_x = N'_y = 108$. The bulk modulus is then calculated by $K = \frac{2E_{box}}{a_{unit}N'_xN'_y\epsilon^2}$, where $A_{unit} = \frac{\sqrt{3}}{2}$.

3.4 Results

We now discuss our main results on the mechanical response of the anisotropic disordered network under the shear and hydrostatic strains. To compare the results of the simulation on the shear modulus G and bulk modulus K of the network with the effective medium theory, we first calculate the corresponding effective medium predictions in terms of the previously calculated spring constants α_m and γ_m. To do so, consider a fully ordered triangular network with central force interactions only. For small, uniform deformations, the strain energy density of a unit hexagonal cell is given by

$$F = \frac{1}{4\sqrt{3}}\Sigma_{b=1}^{6}\alpha^{(b)}n_i^{(b)}n_j^{(b)}n_k^{(b)}n_m^{(b)}u_{ij}u_{km}, \tag{3.8}$$

where the superscript $b = 1, 2, 3, 4, 5, 6$ represents the six nearest neighbor bonds in the unit cell and $\alpha^{(b)}$ is the corresponding spring constant.

For the system under study, the unit vectors $n^{(b)}$ and respective angles $\theta^{(b)}$ for the springs with spring constant α are given by

$$\begin{aligned} \theta^{(1)} &= 0, n_1^{(1)} = 1, n_2^{(1)} = 0 \\ \theta^{(2)} &= \pi, n_1^{(2)} = -1, n_2^{(2)} = 0 \end{aligned} \tag{3.9}$$

Similarly, for springs with γ_m,

$$\begin{aligned} \theta^{(3)} &= \frac{\pi}{3}, n_1^{(3)} = \frac{1}{2}, n_2^{(3)} = \frac{\sqrt{3}}{2} \\ \theta^{(4)} &= \frac{2\pi}{3}, n_1^{(4)} = \frac{-1}{2}, n_1^{(4)} = \frac{\sqrt{3}}{2} \\ \theta^{(5)} &= \frac{\pi}{3}, n_1^{(5)} = \frac{1}{2}, n_2^{(5)} = \frac{-\sqrt{3}}{2} \\ \theta^{(6)} &= \frac{2\pi}{3}, n_1^{(6)} = \frac{-1}{2}, n_2^{(6)} = \frac{-\sqrt{3}}{2} \end{aligned} \tag{3.10}$$

With these inputs, the deformation energy density F of the effective medium anisotropic network is given by [102, 111]:

$$
\begin{aligned}
F =& \frac{1}{8\sqrt{3}}[(8\alpha_m + \gamma_m){u_{xx}}^2 + 9\gamma_m {u_{yy}}^2 \\
&+ 6\gamma_m u_{xx} u_{yy} + 3\gamma_m (u_{xy} + u_{yx})^2]
\end{aligned}
\tag{3.11}
$$

The stress components can then be calculated using $\sigma_{ij} = \frac{\partial F}{\partial u_{ij}}$, and can be used to calculate the direction dependent shear and bulk moduli as shown below [112].

In the simulation we calculate the shear modulus corresponding to the boundary applied shear strain u_{xy}, and the 2D bulk modulus corresponding to a hydrostatic compression. The shear modulus for a shear strain applied via the boundaries along the x direction at $L_y = 0$ and $L_y = \frac{\sqrt{3}}{2}(N_y - 1)$ (in units of the lattice spacing) is given by

$$
G = \frac{\sigma_{xy}}{u_{xy}} = \frac{\sqrt{3}}{4}\gamma_m. \tag{3.12}
$$

Under the hydrostatic compression of the system, the network undergoes a uniform compression by an amount δ in both x and y directions. Clearly $u_{xx} = u_{yy} = \delta$ and $u_{xy} = 0$. The area bulk modulus is given by

$$
K = \frac{\sigma_K}{\Delta A / A}, \tag{3.13}
$$

where the hydrostatic stress σ_K is given by $\sigma_K = \frac{\sigma_{xx} + \sigma_{yy}}{2} = \frac{(\alpha_m + 2\gamma_m)\delta}{\sqrt{3}}$, and the change in area of the system relative to its original area is given by $\Delta A/A = u_{xx} + u_{yy} = 2\delta$. The area bulk modulus is then $K = \frac{\alpha_m + 2\gamma_m}{\sqrt{12}}$. Note that, we recover the expected results $G = \frac{\sqrt{3}}{4}\gamma_m$ and $K = \frac{\sqrt{3}}{2}\gamma_m$ for the isotropic case.

Figure 3.3 shows the shear modulus obtained from the numerical simulation (open symbols) against the effective medium theory (solid lines). We keep p_x fixed at different values, and study how G changes as a function of p_y. We find that the agreement on the value of the shear moduli between the theory and simulation to be rather good for larger values of p_x and p_y. In addition, our effective medium calculations suggest that for the network to have finite rigidity, $\frac{p_x}{2} + p_y \geq 1$, i.e. it is a necessary but not sufficient condition. Random dilution of the triangular lattice leads redundant bonds and floppy inclusions being introduced [17, 108]. Such beyond mean field effects are not taken into account in the Maxwell constraint counting. In other words, the lattice is not cleverly constructed so that, at the transition for example, the network is minimally rigid. One ultimately needs to go beyond mean field (or EMT) and take into account the spatial makeup of the network to determine the precise value of the threshold. Also, the subtraction of the global degrees of freedom are not included in the above condition.

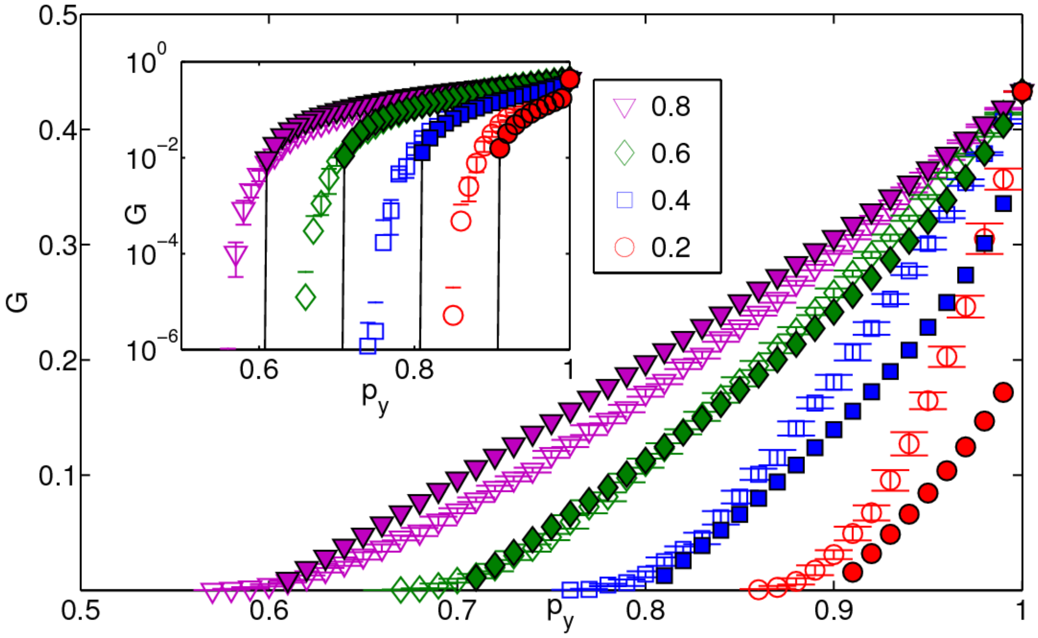

FIGURE 3.3: The shear modulus G as a function of p_y for different p_x as shown in the legend. The open symbols show data from the simulations and the filled symbols (joined by solid lines in the inset) represent the result from the effective medium theory. The inset shows the same data on a log-linear scale. The system size in the simulation is $N_x = N_y = 128$.

We observe that the numerically calculated value of the threshold p_y is less than the analytical estimate. In addition to redundant bonds, floppy inclusions, and subtracting the global degrees of freedom, another reason for the discrepancy is that in the simulation there are two boundaries fixed where the shear deformation is applied. For the vertices on these fixed boundaries, they lose some neighbors compared to those with periodic boundary conditions, but they will add to the number of constraints since they are fixed. This would suggest a smaller threshold of p_y for a given p_x in the simulations as seen.

To begin to quantify such boundary effects we study the dependence of the rigidity percolation threshold on system size as shown in Fig. 3.4. We find that while the numerically calculated value of the threshold is always less than the analytical estimate, it moves closer to the analytical value with increasing system size. Our results suggest that the system-size dependence in the y direction is stronger than in the x direction. This may be because the x-direction has periodic boundary conditions, while in the y direction the boundary conditions are fixed. For a given size, systems with periodic boundaries tend to be less sensitive to finite system size effects as compared to those with fixed boundaries. We must also point out that the finite system size effects are even more pronounced the larger the difference between p_x and p_y.

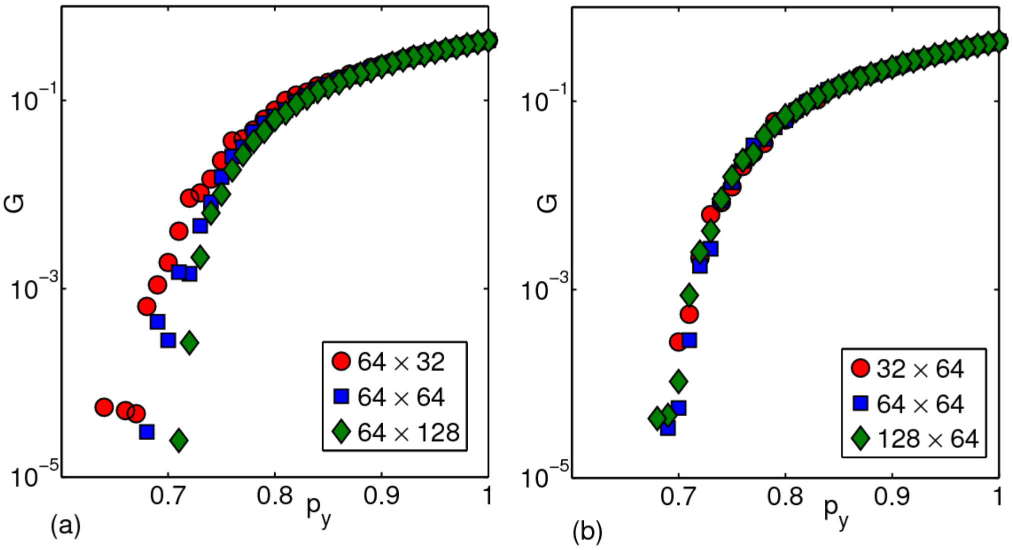

FIGURE 3.4: Shear modulus G (for shear applied via the x boundaries) as a function of p_y at fixed $p_x = 0.5$ and for different system sizes (as shown in legend).

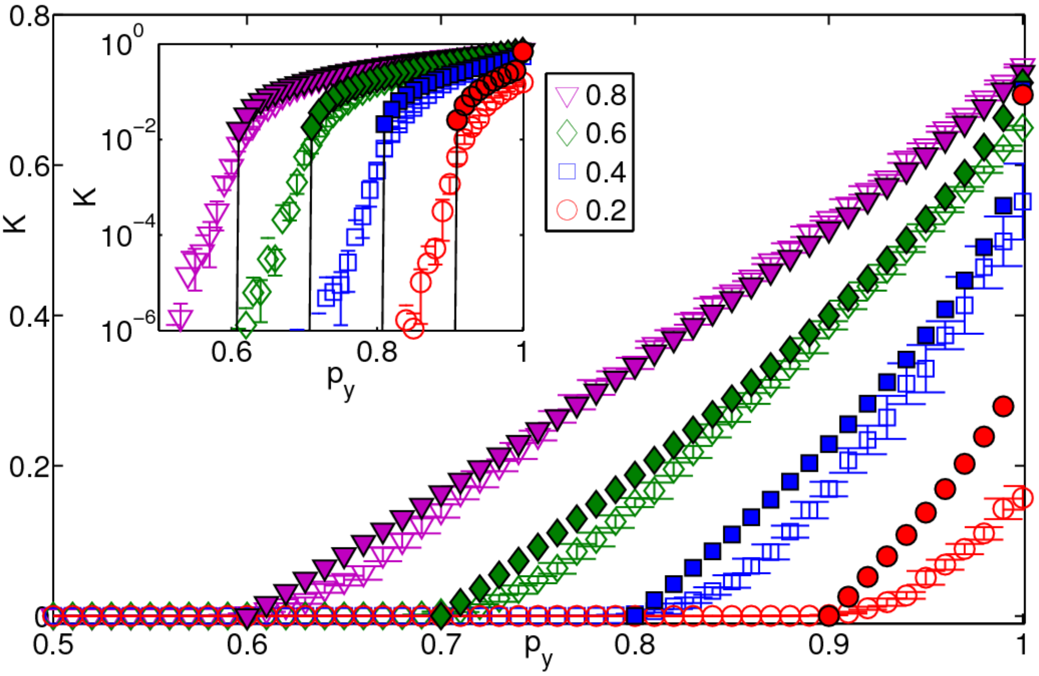

FIGURE 3.5: The area bulk modulus K as a function of p_y for different p_x as shown in the legend in units of the bare spring constant γ (set to unity). The open symbols show data from the simulations and the filled symbols (joined by solid lines in the inset) represent the results from the effective medium theory. The system size in the simulation is set to $N_x = N_y = 128$ and the modulus is calculated from part of the network within a box in the center of the system with box size $N'_x = N'_y = 108$.

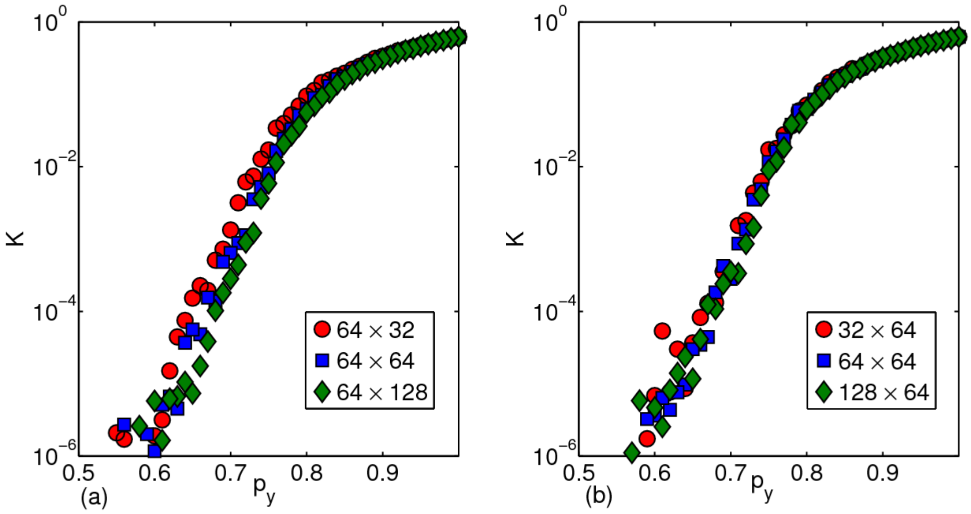

FIGURE 3.6: Area bulk modulus K as a function of p_y at fixed $p_x = 0.5$ and for different system sizes (as shown in legend).

Finally, we also study the bulk modulus K in response to a hydrostatic compression by up to 2%. Our results are shown in Fig. 3.5. As with the shear modulus, we find the best match between the simulations and the analytical estimates on the modulus for larger values of p_x and p_y. We also find that the numerically calculated value of the threshold is less than that the analytical estimate, and moves closer to the analytical value with increasing system size. The system size analysis for the bulk moduli as shown in Fig. 3.6, once again, shows specifically the rigidity percolation threshold moving closer to the theoretical prediction with increasing system size and that changes in the system size in the y direction lead to larger shift in the moduli as compared to changes in the system size in the x direction.

Before concluding, let us discuss two limits that closely relate to prior work. The first is $p_x = 1$. Wang and Harris study an anisotropic spring network on a triangular lattice where $p_x = 1$ and $0 < p_y < 1$ [106]. They propose the existence of a splay rigid phase in which the rotational degrees of freedom potentially freeze out at a smaller occupation probability than the translational degrees of freedom. For the isotropic case, rotational and translational degrees of freedom become constrained across the system at the same occupation probability. When $p_x = 1$, a splay rigid phase exists for $p_y > 0$. It seems, however, that the onset of splay rigidity coincides with rigidity, which also coincides with the connectivity bond percolation threshold on the square lattice, which is $p_c = 1/2$. Our effective medium theory predicts a rigidity percolation threshold $p_{y,rp} = 1/2$ with our lattice simulations yielding $p_{y,rp} \approx 0.4$ (for our largest system size). See Fig. 7.

When $p_x = 1$, Wang and Harris, following Roux and Hansen, consider the dual anisotropic problem of a spring with infinite spring constant with probability p_y and finite spring

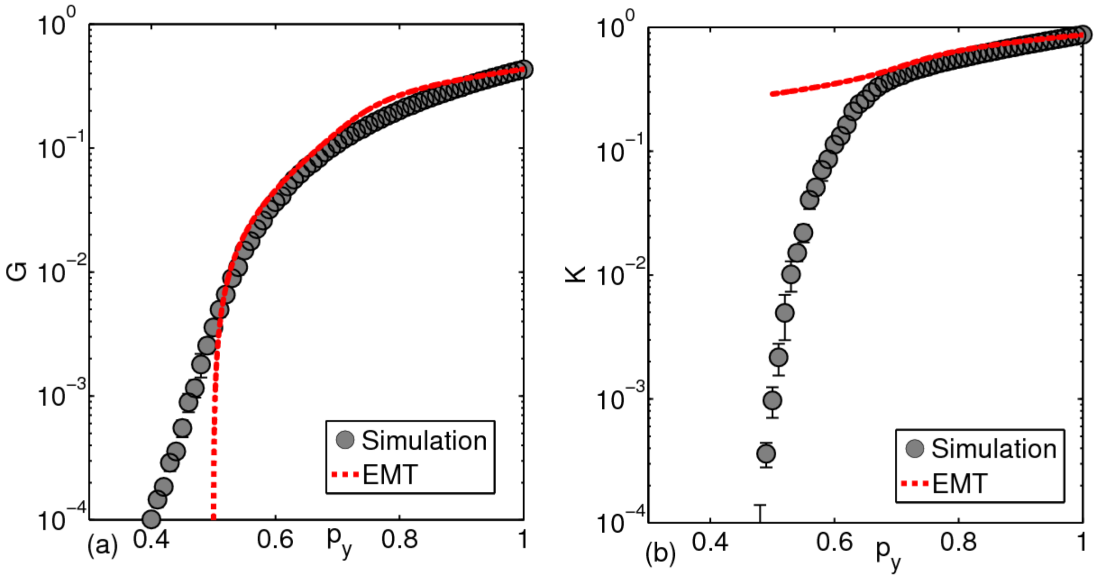

Figure 3.7: The shear modulus G and bulk modulus K as a function of p_y at fixed $p_x = 1$.

constant for probability $1 - p_y$, otherwise known as the “super-elastic” case [105, 106]. Wang and Harris demonstrate that the behavior of the bulk modulus K should be identical to the conductance exponent in random resistor networks in the super-elastic network case [106]. Random resistor networks are scalar analogues to the vectorial force/rigidity percolation [113]. It is not obvious whether their results can be extended to the bond-diluted case studied here. And, in fact, our analytical results suggest that at $p_{y,rp} = 1/2$, K is has a finite value proportional to the spring constant α of the springs in the x direction, i.e K jumps discontinuously from zero for $p_y < 1/2$ (See Fig. 7). The simulations show a K increasing from ~ 0 in not as dramatic way due to the finite size of the system. More detailed finite system size studies are needed to determine the existence of a jump in the lattice simulations. The shear modulus G, on the other hand, increases continuously from zero as a function of p_y.

As for the second limit, the system is isostatic when $p_y = 1$ and $p_x = 0$ and periodic boundary conditions are implemented. For fixed boundary conditions, the system is hyperstatic (over-constrained) and for free boundary conditions, the system is hypostatic (under-constrained). In the periodic case, we expect a rigidity transition as soon as $p_x > 0$ as dictated by Maxwell constraint counting. This expectation is also related to work by Mao and collaborators beginning with a fully occupied square lattice of springs and adding next-nearest-neighbor springs with probability p_{NNN} [114, 115]. In this model, the system is rigid for $p_{NNN} > 0$, i.e. the transition occurs at $p_{NNN} = 0$. The result goes beyond the mean-field Maxwell constraint counting, which, again, is a

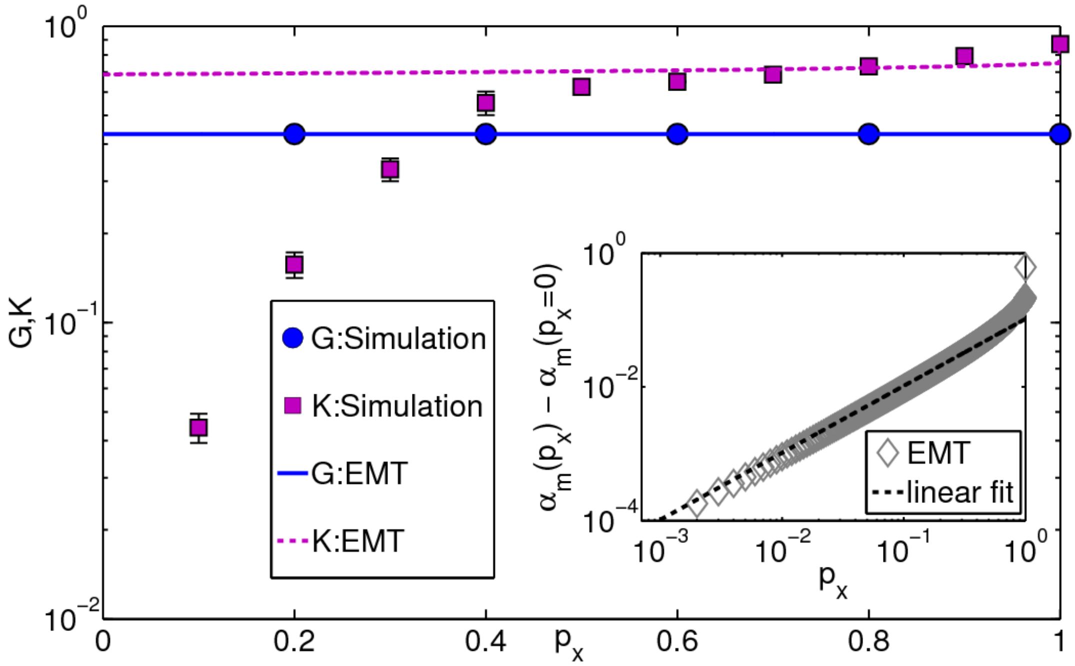

Figure 3.8: The shear modulus G and bulk modulus K as a function of p_x at fixed $p_y = 1$. The inset shows the effective medium elastic constant α_m as a function of p_x at fixed $p_y = 1$.

necessary, but not sufficient condition for rigidity [115]. In addition, G becomes non-zero continuously with $G \sim p_{NNN}^2$ [114]. In our model, p_x is the corresponding p_{NNN}, however, it is a nearest neighbor bond. Interestingly, we obtain a discontinuous onset in G at $p_x = 0$, where the rigidity transition occurs. See Fig. 8. This is because our shear is applied 45 degrees to the p_y bonds with fixed boundary conditions in the y-direction, while in the earlier work shear is applied perpendicularly to the vertical square lattice bonds. Given the relation between the effective spring constants and K, $K > 0$ as well at the transition. As p_x increases above zero, G remains constant while K increases to its respective limiting value. We find that $\alpha_m(p_x) - \alpha_m(p_x = 0)$ increases linearly with p_x to compare with the quadratic behavior found in the square lattice with additional next-nearest neighbor bonds. See Fig. 8.

We now end this results section with a phase diagram that incorporates bending in the manner described by Equation 1.6, the co-linear bending along filaments. See Figure 3.9. With the introduction of more constraints via bending, as expected, the region of rigidity is enlarged upon the addition of bending. We are currently working to understand this phase diagram from an analytical perspective.

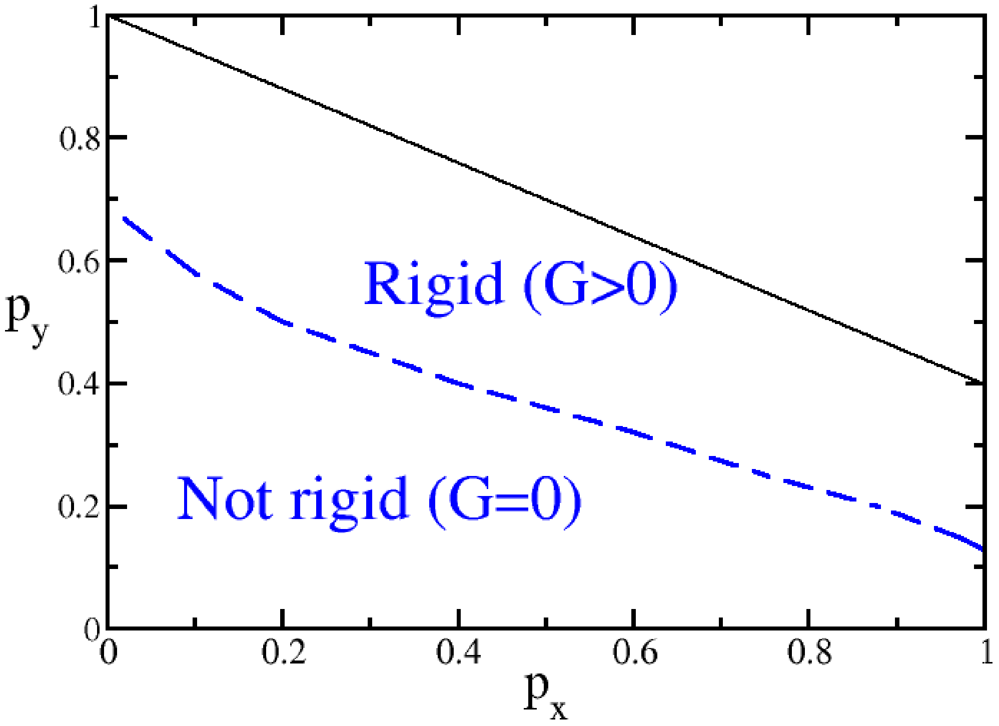

FIGURE 3.9: Phase diagram with semiflexibility included. The black line denotes the nonrigid-rigid boundary in the absence of bending.

3.5 Discussion

We have now extended effective medium theory (EMT) to anisotropic disordered spring networks. We have done so by considering a particular type of anisotropy in the occupation probability such that the triangular lattice can be considered as two interconnected sub-lattices leading to two coupled equations for the effective medium elastic constants, α_m and γ_m. The elastic response of the system, such as the bulk and shear moduli, depend on these effective medium constants. For example, the shear modulus G_{xy} was found to $\sqrt{3}\gamma_m/4$ with both the effective medium theory and simulations. Given the anisotropy of the network, there also exists a second shear modulus for shear applied at 60 degrees to the $x - y$ shear, given by $\sqrt{3}(\alpha_m + \gamma_m)/8$, and can be obtained from the theory. This work focused on shear strains applied in the $x - y$ direction for the calculation of the shear modulus, and uniform expansion in all directions for the bulk modulus.

The rigidity percolation thresholds from our EMT agree with Maxwell constraint counting with the threshold depending on both p_x and p_y. And unlike the isotropic case where G and K increase linearly with p above the transition, the G and K versus p_y curves (at fixed p_x) exhibit a slight departure from linearity. While this beyond-linear aspect is not as dramatic as in the EMT with spring networks with additional angular springs [20, 116–119], anisotropy is yet another way to generate nonlinearity in the G vs p characteristics in a disordered solid, even at small strains. Although the stress-strain relationship continues to be linear at small strains studied in this work, we speculate that anisotropy would have a non-trivial contribution to the nonlinear scaling of the shear modulus, and the differential shear modulus as a function of strain at large strains, and will be studied in future work.

Drawing further comparison with the isotropic triangular lattice, we find in two limiting cases, discontinuous onsets of the bulk and/or shear modulus. Such discontinuous onsets do not occur in the isotropic case. When $p_x = 1$, the bulk modulus jumps discontinuously from zero to a finite value as a function of p_y, while the shear modulus increases continuously from zero. When $p_y = 1$, both the bulk and shear modulus jump discontinuously from zero to a finite value at $p_x = 0$. The latter result differs from recent work adding additional next-nearest-neighbor springs to a square lattice of springs. In this recent work, the shear modulus is equal to effective spring constant due to these additional springs and scales quadratically with the occupation probability of the next-nearest-neighbor bonds, i.e. it increases beyond zero continuously. In the anisotropic case, the "additional" p_x bonds are nearest-neighbors bonds and the effective medium elastic constant scales linearly with p_x (see inset of Fig. 3.8) after some initial non-zero value at $p_x = 0$ due to the x-component of the p_y bonds contributing to elasticity (in the x-direction).

We compare our EMT with lattice simulations and find rather good agreement, particularly for larger values of p_x and p_y. As with lattice simulations in the isotropic case, the rigidity percolation threshold is lower than the EMT value. For reference, in the isotropic case, the EMT threshold value is $p_{rp} = 2/3$, while simulations yield $p_{rp} = 0.6602 \pm 0.0003$ [17] the p_{rp}s to the infinite system limit in the isotropic case is difficult. For the anisotropic case, the task is further complicated by anisotropic finite-size scaling with different relevant length scales in the two directions such that one needs to rescale the x and y directions by different amounts. Anisotropic finite-size scaling in, say, directed percolation, has been done and is based on a field theory able to estimate the two different length scales [120]. The absence of a field theory for rigidity percolation leaves one little to hang his/her hat on and so we leave this for future work.

While our lattice simulations are not as in good agreement with the EMT as in the isotropic case, this discrepancy is due, in part, to finite-size effects, which tend to be more complex in anisotropic systems than isotropic systems given the presence of different lengthscales. On the other hand, one could argue that the rather good agreement is unexpected since the effective dimensionality of the system may differ from the isotropic case where mean field and two-dimensional predictions behave similarly.

To our knowledge, our EMT calculation is the first for anisotropic spring networks and lays the foundation for the next stage where we will consider the presence of bending elasticity and non-linear response to more accurately mechanically model cytoskeletal filaments in lamellipodia where the actin filaments have a preferred orientation [103, 104]. We would then be able to better quantify the collective elastic response of a system that is important for cell motility on two-dimensional substrates. This will also allow for better comparison with recent work on the mechanics of anisotropic semiflexible polymer networks [121–123]. We have begun to do so as indicated in Figure 3.9. It would also be interesting to investigate the effects of splay rigidity [106, 107] in anisotropic network models with bending, which may turn out to be more generic than originally thought and may be relevant for packing derived anisotropic networks based on granular materials and emerging liquid crystalline order in elastomeric gels. Such effects can be quantified with development of anisotropic effective medium theories going beyond the one constructed here.

Chapter 4

Coupled spring networks

4.1 Introduction

The previous chapter explored the role of anisotropy in disordered spring networks. Motivated yet again by a biological example, we explore the mechanics of coupled disordered spring networks. Since the number of ways two disordered spring networks can be coupled together is vast, let us first focus on the biological example. The example will help guide the nature of the coupling.

It has already been established that the actin cytoskeleton provides the cell with structural integrity and allows it to change shape. A *potential* new role for the actin cytoskeleton, however, has recently emerged, namely a role in the mechanical regulation of transcription [124–126]. Yes, transcription. Transcription initiates gene expression with a segment of DNA being copied by mRNA. The mention of DNA, which sits inside the nucleus, then begs the question: How does the actin cytoskeleton outside the cell nucleus interact with the DNA inside the cell nucleus if the actin cytoskeleton is to play a potential role in the regulation of transcription?

Cytoskeletal actin filaments bind to nesprin-1 and -2 located on the outer nuclear membrane. See Figure 4.1. Nesprins interact across the perinuclear space through their C-terminal KASH domain with SUN proteins, which reside in the inner nuclear membrane. The SUN proteins can then bind to the lamin network located just inside the inner nuclear membrane. This complex of proteins connecting the nuclear lamina and the actin cytoskeleton is called LInkers of the Nucleoskeleton and Cytoskeleton (LINC) complexes [26, 27]. Lamins are intermediate filaments forming a filamentous network surrounding the DNA, RNA, and other proteins located at the core of the cell nucleus [28]. It has recently been discovered that mammalian genomes contain about 1,000-1,400 lamina associated domains (LADs) that specifically associate with the nuclear lamina [127].

While the LADs are typically gene poor, they impose major constraints on the spatial organization of the DNA so that disrupting the lamin-LAD binding could lead to changes in the packing of the DNA. Therefore, through the sequence of actin filaments binding to nesprins binding to SUN proteins binding to lamins binding to DNA, there exists a means by which forces imposed on cytoskeletal actin are transmitted to the DNA. It has indeed been observed that disruption of the LINC complex impairs the propagation of intracellular forces [128].

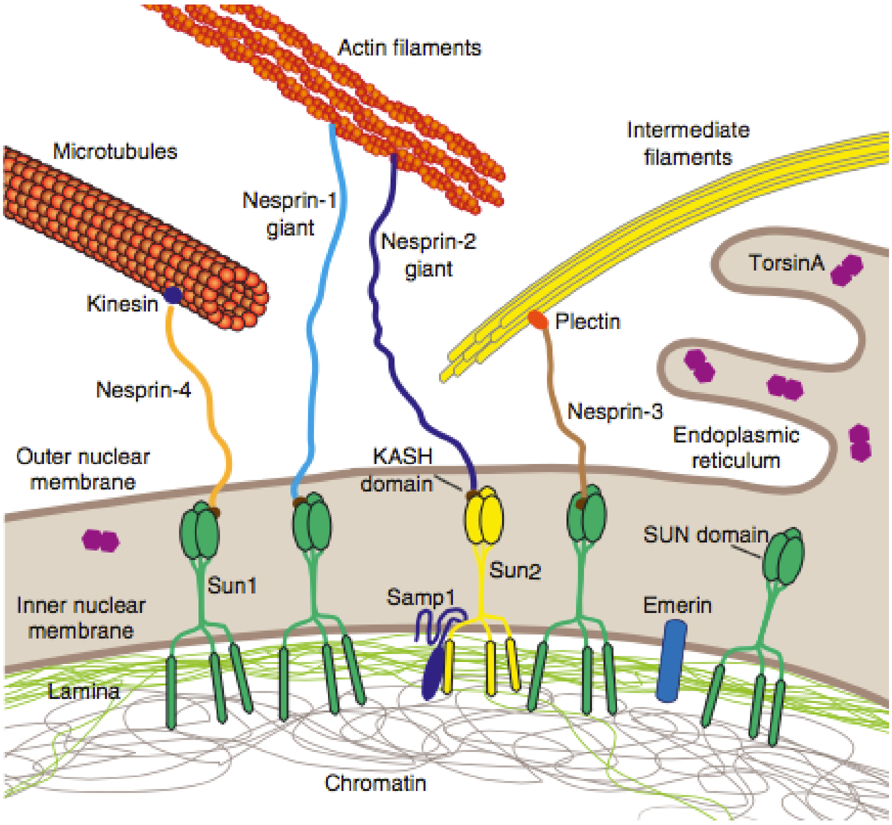
Actin filaments
Microtubules
Intermediate filaments
Nesprin-1 giant
Nesprin-2 giant
TorsinA
Kinesin
Plectin
Nesprin-4
Nesprin-3
Endoplasmic reticulum
Outer nuclear membrane
KASH domain
SUN domain
Sun1
Sun2
Samp1
Emerin
Inner nuclear membrane
Lamina
Chromatin

FIGURE 4.1: Schematic of the actin-LINC complex-lamin-chromatin (DNA+proteins) coupling. Figure from Ref. [129]

Just because there are forces transmitted from the actin cytoskeleton to the DNA does not necessarily imply that the actin cytoskeleton can regulate transcription. While there is no direct evidence for this, there is certainly indirect evidence [124]. For example, mutations or deletion of the nuclear envelope proteins that connect the nucleus and cytoskeletonparticularly lamins A/C, emerin, and nesprinscause impaired activation of mechanosensitive genes in response to mechanical stress [128]. In addition, disruption of the nucleo-cytoskeletal coupling abrogates mechanically induced conformational changes in nuclear proteins [130].

Since both the actin cytoskeleton and the lamin nucleoskeleton are filamentous, semi-flexible polymer networks, they can be modeled as disordered springs networks with

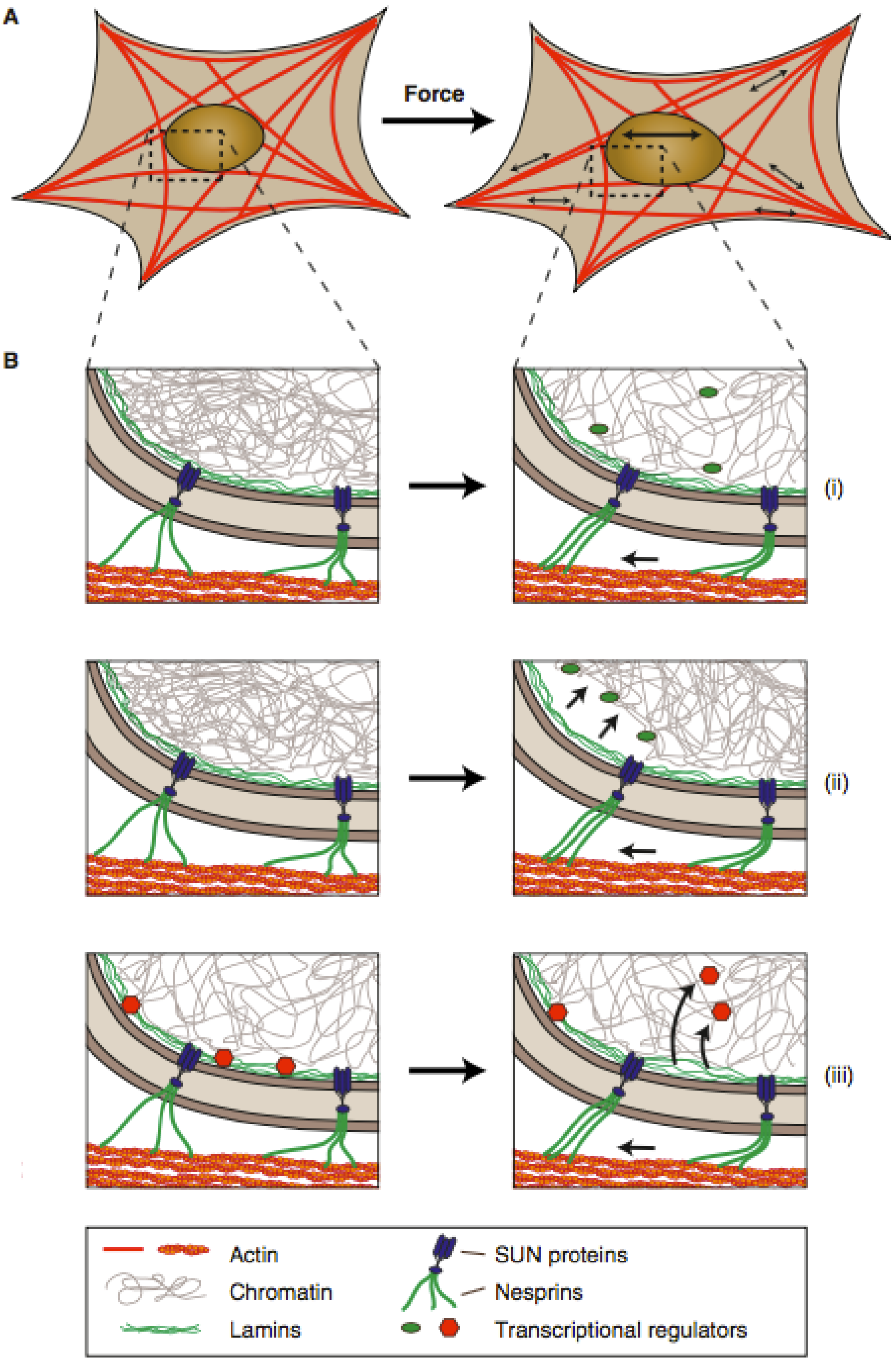
A
Force
B
(i)
(ii)
(iii)
Actin
Chromatin
Lamins
SUN proteins
Nesprins
Transcriptional regulators

FIGURE 4.2: Schematic for potential mechanisms for the mechanical regulation of transcription. In (A) the cell is exposed to uniaxial stretch. In (B) various effects of that stretch are proposed. Figure from Ref. [129].

bending and stretching. The LINC complex, comprised of the nesprin and SUN proteins, provide the coupling between the two networks. At this juncture, not much is know about the mechanics of lamin networks or the LINC complex. While such details may be important, as a physicists, we begin to explore mechanical interplay between a model actin cytoskeleton and a model lamin nucleoskeleton to ultimately determine different classes of couplings, if you will. We will ultimately incorporate model DNA, which directly binds to lamins and investigate how deformations in the actin network induce deformations in the lamin network and, subsequently, the conformation of the DNA. This latter step, however, is outside the boundaries of this thesis.

To begin to look for a microscopic basis for the mechanical regulation of transcription via the actin cytoskeleton, we first study the mechanics of two coupled disordered spring networks with stretching only. We would like to understand this limit first before including bending and the DNA. In particular, we will measure the shear modulus of the coupled disordered spring network as a function of properties of the coupling between them for small strains.

To ultimately understand potential conformational changes in the DNA, we will not only study the limit of small strains (as was done in the previous chapter), we will also study the limit of large strains. In this limit, the network can be underconstrained in terms of Maxwell constraint counting, and yet undergo a strain-induced rigidity transition [108, 131]. This is because large strains may not couple to the zero-frequency modes in the system, i.e. the node displacements are orthogonal to the strain. Since zero-frequency modes fluidize the system, if they are frozen out, then the system appears rigid.

4.2 Model and Methods

Consider a three-dimensional HCP lattice where each bond on the lattice represents a spring. The HCP lattice is broken up into three regions, regions 1, 2, and 3. Regions 1 and 3 represent the actin and lamin networks respectively, while Region 2 represents the proteins connecting the two networks. Note that the model does not include the inner and outer nuclear fluid membranes for simplicity. The disorder is implemented by randomly diluted bond ij of the HCP lattice with dilution probability $1-p_{1,ij}$, $1-p_{2,ij}$, and $1-p_{3,ij}$ in each region respectively. For the coupling region, Region 2, the dilution of bonds is broken down into two types—those that are in the $x-y$ plane, denoted as $p_{2xy,ij}$ and those bonds that are extended in the z-direction, denoted as $p_{2z,ij}$. This is because the LINC complexes do not appear to form a cross-linked network of extended proteins [129]. In other words, LINC complex springs connect to the actin network at one end and the lamin network at the other and do not interconnect among themselves. Each region has its own spring constant, k_1, k_2, and k_3. See Figure 4.3 Putting these pieces together, the total energy of the coupled network with $N = N_1 + N_2 + N_3$ vertices/nodes is

$$E_{CN} = \frac{k_1}{2} \sum_{\langle ij \rangle\ \in 1} p_{1,ij}(|\mathbf{u}_i - \mathbf{u}_j| - 1)^2 + \frac{k_3}{2} \sum_{\langle ij \rangle\ \in 3} p_{3,ij}(|\mathbf{u}_i - \mathbf{u}_j| - 1)^2$$
$$+\frac{k_2}{2} \sum_{\langle ij \rangle\ \in 2,xy} p_{2xy,ij}(|\mathbf{u}_i - \mathbf{u}_j| - 1)^2 + \frac{k_2}{2} \sum_{\langle ij \rangle\ \in 2,z} p_{2z,ij}(|\mathbf{u}_i - \mathbf{u}_j| - 1)^2, \tag{4.1}$$

where $\mathbf{u}_i$ is the position of the vertex i and the lattice spacing is set to 1.

To obtain information about the mechanics of the coupled network, a shear strain γ is applied followed by minimization of the total energy using the same conjugate gradient method described in the previous chapter. In the limit of small strains, the shear modulus, $G = 2E/V\gamma^2$, gives a measure of the mechanical robustness of the system. For all strains, one can compute the stiffness K of the coupled network where $K = \frac{d^2E_{CN}}{d\gamma^2}$. Strains from about 1 percent to 40 percent are studied.

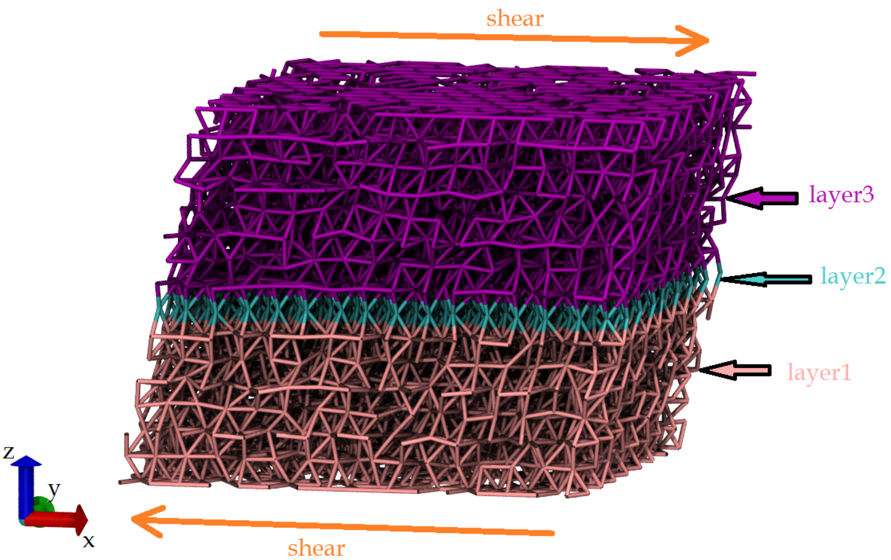

FIGURE 4.3: Schematic of coupled network.

4.3 Results

4.3.1 Decoupled limit

For context, first set $p_{2xy,ij} = p_{2z,ij} = 0$ so that the Regions 1 and 3 are decoupled. Focusing only on Region 1 and the limit of small strains, we study the rigidity transition as a function of $p_{1,ij}$. In this limit, Maxwell constraint counting tells us that the transition should occur when the number of degrees of freedom equals the number of constraints, or

$$< z_1 >= 6, \tag{4.2}$$

which translates to $p_{1,ij} = 0.5$ for the HCP lattice since for the fully-occupied lattice $z_1 = 12$. Of course, this condition is necessary but not sufficient so the transition could occur at a different average coordination number as addressed earlier. In Figure 4.4, we plot the shear modulus G as a function on $p_{1,ij}$. We find a transition probability p_r that is slightly lower than the Maxwell constraint counting argument, which is consistent with two-dimensional findings of a slightly smaller p_r than what is found by Maxwell constraint counting [18]. Specifically, we find $p_r \approx 0.46$. Above the rigidity transition we observe linear behavior in the $G(p_{1,ij})$ curve due to the linearity of the springs at small strains. This result is also consistent with Figure 1.8 in two dimensions.

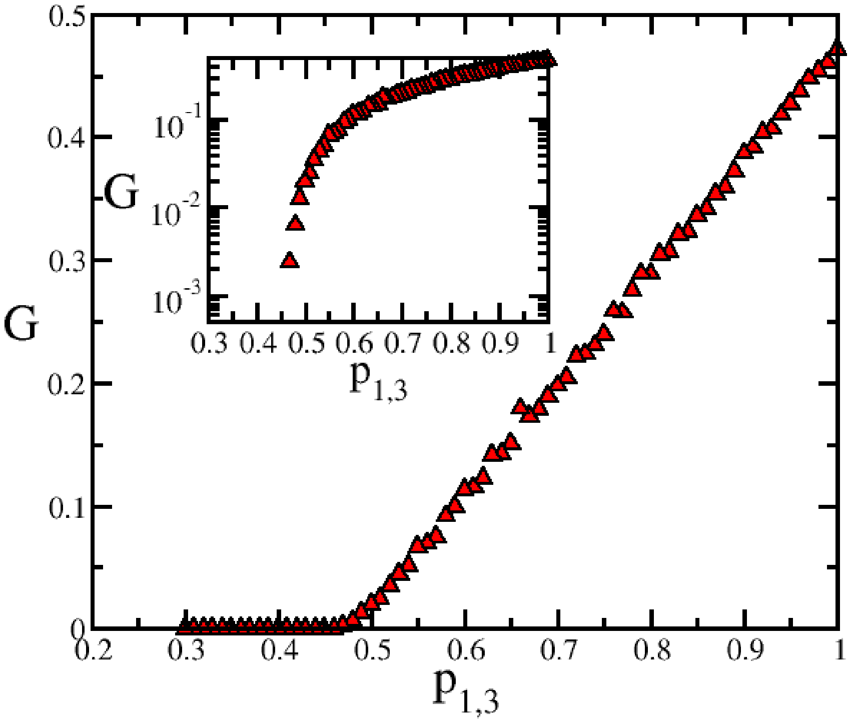

FIGURE 4.4: The shear modulus G as a function of $p_{1,ij} = p_1 = p_2 = p_3$ for small strain ($\epsilon = 5\%$) and $k_1 = 1.0$. The inset shows the same data on a log-linear scale. The system size in the simulation is $L_x = L_y = L_z = 16$. Note that G is measured in units of the spring constant and the lattice spacing.

At larger strains, a rigidity transition can be induced even for $p_{1,ij} < p_r$. We observe this strain-dependent transition in Figure 4.5 where we observe a strain-dependent transition in the energy as a function of strain in the sense that the energy changes on a logarithmic scale from essentially zero to nonzero. Note that we did not compute the stiffness K but will do so in the near future. For $p_{1,ij} = 0.4$, the strain-induced rigidity transition occurs at around 15 percent strain, while for $p_{1,ij} = 0.3$, it occurs around 25 percent strain. The more dilute the system, the larger the strain required to freeze out the zero-frequency modes and rigidify the system.

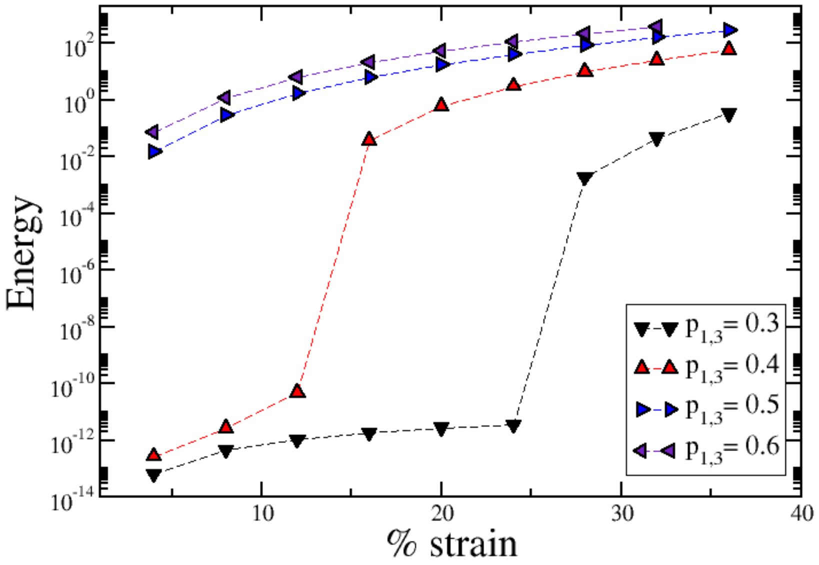

FIGURE 4.5: Energy as a function of percent strain for different values of $p_{1,ij} = p_1 = p_2 = p_3$. Note that energy is measured in units of the spring constant and the lattice spacing.

4.3.2 One coupled limit

We now study the limit $p_{1,ij} = p_{3,ij}$, $p_{2xy,ij} = 0$, and $k_1 = k_2 = k_3 = 1$. Also, $N_1 = N_3$ and $N_2 = L_x \times L_y$, where L_x is the system length in the x direction and L_y is the system length in the y direction, i.e. Region 2 is one layer "thick". In this limit for small strains, when $p_{2z,ij} = 0$, Regions 1 and 3, again, become decoupled and we expect zero shear modulus in the limit of small strains and zero stiffness for all strains studied and even if Regions 1 and 3 are rigid independently. This is because the system has been split into two separate systems. Now the following questions emerge: How large does $p_{2z,ij}$ have to be for the stiffness to be non-zero even when Regions 1 and 3 are rigid independently? As in the case for the strain-induced rigidity transition, does it depend on the amount of strain? Moreover, if Regions 1 and 3 are just below rigidity, could a few extra connections via Region 2 cause the system to go from nonrigid to rigid?

We, again, begin with the small strain limit. In Figure 4.6 we present results for $G(p_{1,ij})$ for different p_{2z}s. We observe that for $p_{2z} = 0$, G is essentially zero for all $p_{1,ij}$ studied, as expected. We also observe, interestingly, that the location of the transition shifts to below $p_r =\approx 0.46$ for $p_{2z} = 0.8$ and $p_{2z} = 1.0$. This could mean that the extra connections in the coupling region may induce rigidity globally even though the effective occupation probability is higher only in one region of the network. Careful finite-size scaling analysis is needed to further test this idea.

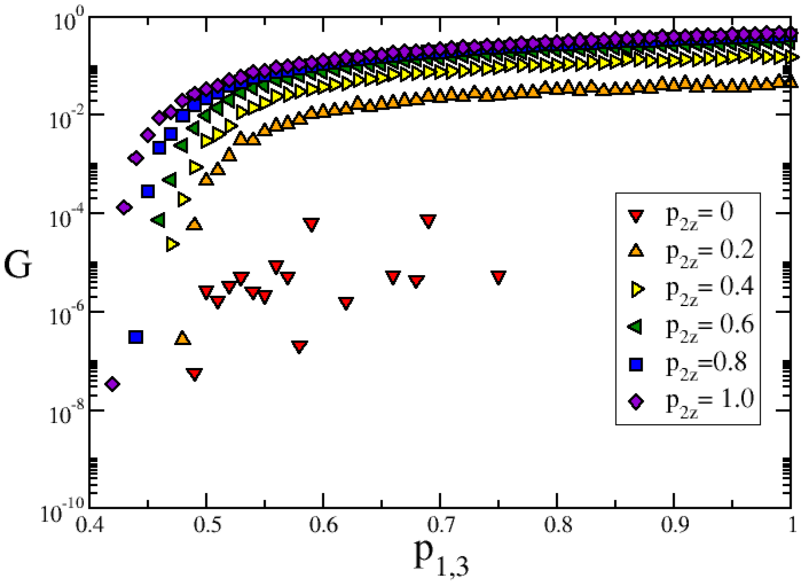

FIGURE 4.6: G as a function of $p_{1,3}$ for different p_{2z}s. The strain is 4 percent and $L_x = L_y = L_z = 16$.

In the limit of large strain, we study the strain-inducing rigidity transition and present our results in Figure 4.7. We observe that for $p_{i,ij} < p_r$, large external strain can induce rigidity. We also observe that increasing p_{2z} shifts the location of the transition downward.

4.4 Discussion

We observe a rigidity transition on the randomly diluted HCP lattice as a function of the dilution with a threshold is close to the Maxwell constraint counting criterion. We also observe a strain-induced rigidity transition in the randomly diluted HCP lattice. What is the nature of the transition remains to be explored.

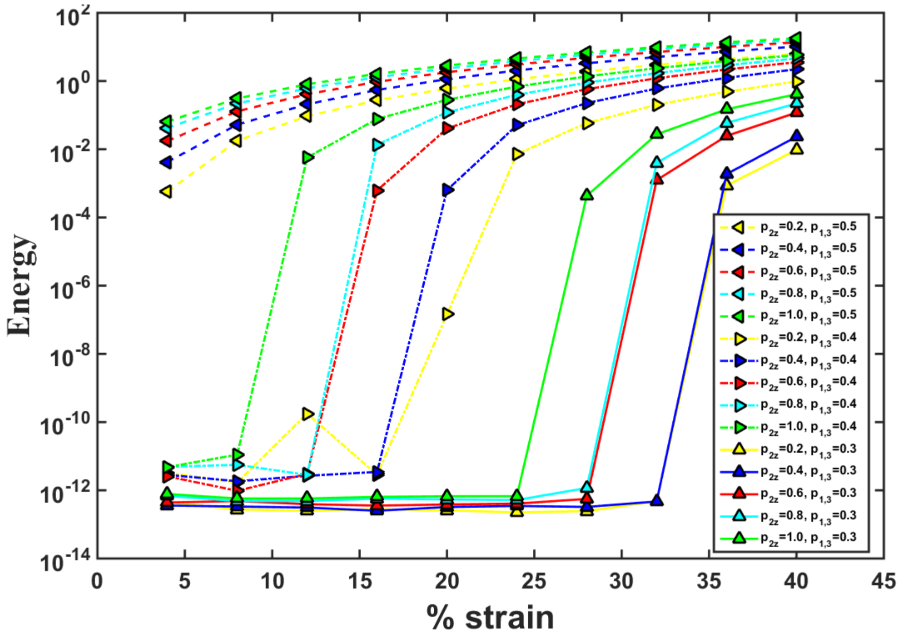

FIGURE 4.7: Energy as a function of strain for different p_{2z}s and several $p_{1,3}$s.

For the coupled network in the limit of small strains, we find a rigidity transition whose location can be downshifted with an increase in p_{2z}, the occupation probability of springs in the coupling region. The strain-induced rigidity transition is also observed in the coupled network case.

In light of our initial motivation, one advantage of coupling two spatially distinct spring networks is that each can have its own rigidity and, yet, if there is no coupling between them, there is no force transmission from one network to the other, i.e. one network is insulated from the other. However, with just a few LINC complex springs, if your will, there is rigidity across the coupled system and one networks transmits force to another. So the coupled network can be sensitive to a small increase in coupling springs. The concentration of coupling springs can also affect the location of the transition. The biological system may exploit this knob to moderate force transmission between the two networks.

After further mechanical understanding of this coupled spring network system we will incorporate model DNA into the system and investigate how deformations in the spring network propagate down from Region 1 to Region 3 via Region 2 and potentially deform the DNA.

Chapter 5

Shape-shifting droplet networks

5.1 Motivation

In nature there are many biomaterials that are internally programmed to morph into complex structures that actively and adaptively interact with the environment. Polypeptide chains fold into proteins and tubular lipid membranes self-assemble in branching networks to form the endoplasmic reticulum. Organisms as a whole develop shape by reorganizing the spatial distribution of their constituent cells in morphogenesis.

These biological examples have inspired the development of *programmable* materials that controllably fold into designated structures. At the nanometer scale, the programmable chemistry of Watson-Crick base pairing allows DNA to self-assemble into a tetrahedron [29]. At the millimeter scale, efficient algorithms have been constructed to generate self-folding three-dimensional polyhedra from two-dimensional nets, driven by the minimization of the surface tension of liquid hinges that either rotate or fuse panels into place [30]. At the centimeter scale, researchers have created a self-folding robot that goes from flat to walking in several minutes without external intervention [31].

A beautiful realization of these ideas comes from the Bayley group who print tens of thousands of micron-sized aqueous droplets each joined by single lipid bilayers [32–36] to form a cohesive, tissue-like material (Fig. 1.14). The droplets in these networks can be endowed with different osmolarities. The resultant osmotic pressure leads to local fluid flow from low to high concentration. This swells the high concentrations droplets and shrinks the low concentration droplets, leading to internal stresses which distort the shape of the network in specific ways depending on the initial geometry of the network and the concentration differences.

Here we use computational methods to explore the self-assembly of several shapes including rings, spirals and tetrahedral shells. We revisit the formation of rings studied in [32] and identify a buckling transition from a round to a polyhedral ring after ring closure. The spirals provide an interesting example of an initial quasi-one-dimensional structure generating a three-dimensional structure. Tetrahedra, the simplest and least symmetric class of the regular polyhedra, can serve as mesoscopic building blocks for molecules and bulk materials with sp^3-like directional bonding [37, 38].

Systems undergoing shape shifting as a result of interaction with their environment have been of recent interest. A strip of paper will, for instance, spontaneously curl up in your hand due to the interaction between the paper and the moist evaporative boundary layer of the hand [132]. Bacillus spores respond to relative changes in environmental humidity with low humidity causing the spores to shrink and high humidity causing the spores to expand [133]. When these spores self-assemble into a dense monolayer sitting on a substrate, one can cycle the relative humidity of the environment to form an actuator. Osmotic actuation is used in plants, perhaps because it can generate a variety of plant movements, depending on the environmental conditions [134], without consuming much power.

Here we shall explore this plant analogue in the micron-sized droplet network and show how shape shifting can be made reversible by exploiting the dynamically evolving coupling to the environment, which here is simply the surrounding solvent. We illustrate reversibility with shape shifting from a four-petal configuration to a hollow sphere transition and back. This opens the way to osmotically-driven small scale robotics.

5.2 Model

We model the droplet network using molecular dynamics in three-dimensional Euclidean space. Each droplet i is treated as a fluid sphere of mass m_i, radius R_i and osmolarity (defined as the number of osmoles (Osm) of solute per litre (L) of solution) C_i. As described in Ref. [32], each droplet interacts with neighboring droplets via an elastic interaction and an osmotic interaction. The elastic interaction potential of a pair of droplets i and j via the bilayer attaching the two droplets is written as

$$E_{ij} = \begin{cases} \dfrac{1}{2} k \left[r_{ij} - l\left(R_i + R_j\right)\right]^2 & \text{for } r_{ij} \leq R_i + R_j \\ 0 & \text{for } r_{ij} > R_i + R_j \end{cases} \tag{5.1}$$

where k is the spring constant, r_{ij} is the distance between a pair of droplets i and j, and $l = 0.8$ represents the change of the equilibrium length due to the deformation of two droplets when they are fused [32]. A damping force for each droplet proportional to its velocity is included as demanded by Stokesian flow. The exchange of water between droplets of different osmolarities is described by Fick's first law as

$$J_{ij} = A_{ij} D \left(C_j - C_i\right), \tag{5.2}$$

where J_{ij} is the volume of water transferred per unit time from a droplet i with osmolarity C_i to a connected droplet j with osmolarity C_j, A_{ij} is the common interfacial area of two connected droplets i and j and D is an effective permeability coefficient taken to be constant. The flow of water between two connected droplets changes the size of each droplet. To simulate the dynamics of the droplet network, the net force on each droplet $\vec{F}_i$ is described by

$$\vec{F}_i = -\sum_{<ij>} \frac{dE_{ij}}{dr_{ij}} \hat{r}_{ij} - \gamma \vec{v}_i = m \frac{d^2 \vec{r}_i}{dt^2}, \tag{5.3}$$

where $\vec{v}_i$ is the velocity of droplet i and γ is the damping coefficient. Following Ref. [32], we assume m, k, and D are the same for all droplets. Because the time scale for mechanical relaxation is much faster than the time for water transfer (seconds compared to tens of minutes), any global shape change is in mechanical quasi-equilibrium. Thus the simplifying assumption of identical and constant m, k, and D for all droplets should not affect our results in any significant way. We chose, in simulation units, $D = 0.002$, $k = 10^3$, and $m = 0.2$. The value of the damping coefficient, $\gamma = 1.1$, was chosen so that there are no oscillations between the droplets when they bind as observed experimentally. The osmolarities (C_i) were chosen to give gradients similar to those for the flower-closing experiment. Length, time, and mass scales in simulation units can be converted to microns, seconds, and grams by matching to experiment.

Implementing different initial osmolarity gradients and droplet configurations yields folding into a variety of important structures such as rings, spirals, and tetrahedra. To search for such structures, the droplets are initially positioned in hexagonal closed-packed arrangements and equilibrated first without water exchange, after which osmosis is switched on. Any two droplets in contact are then connected via the elastic interaction. Once the elastic interaction is established, water is exchanged via Fick's first law and the radius of each droplet is updated accordingly. The position of the center of each droplet is then updated using a fourth-order Runge-Kutta scheme to obtain the position of the centers at the subsequent time step with $\Delta t = 0.01$ in simulation units. We have checked that our simulation results are robust to making the time step as small as $\Delta t = 0.001$ and as large as $\Delta t = 0.02$. As for the computational cost involved, a 4372 particle simulation for tetrahedron formation over 250,0000 simulation time steps took approximately 3 hours and 19 minutes on a computer with 2 quad core 2.66GHz processors.

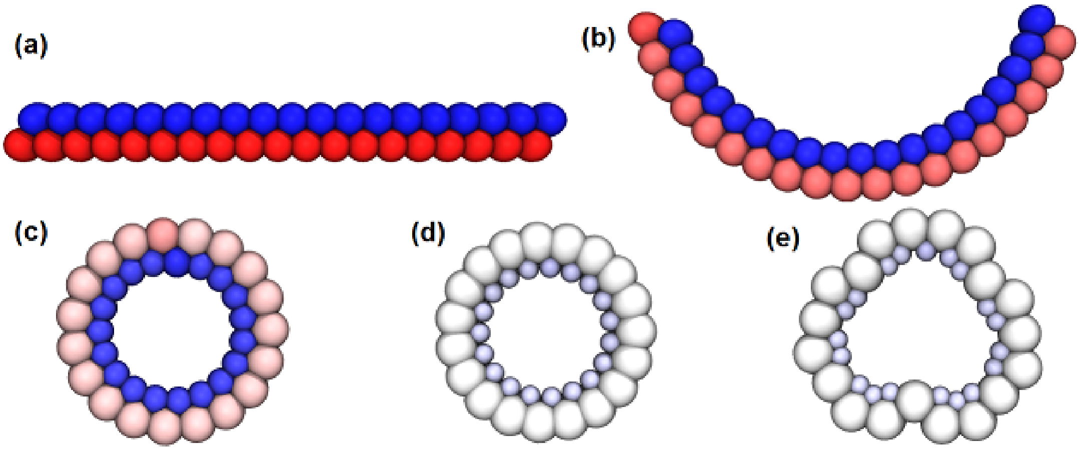

FIGURE 5.1: (Color online) (a)-(e) Buckling of a ring with $N = 38$ total droplets. The initial osmolarities of the two rows are $C_1 = 0.1$ (blue) and $C_2 = 1.0$ (red), respectively. Snapshots were generated using the Visual Molecular Dynamics (VMD) package [136] and rendered using the Tachyon ray tracer [137].

To model the droplet network osmotically interacting with the solvent in a controlled way, we place the folded droplet network in a medium with osmolarity C_m exceeding any individual osmolarity of the droplets. The surrounding medium can only interact with part of the droplet network, as described above. We did not simulate the medium explicitly and neglected any mechanical response of the medium.

5.3 Methods and results

We have explored the following structures:

5.3.1 Rings

The buckling of a circular elastic ring subject to an external radial pressure has been extensively studied in applied mechanics [135]. To study ring formation and subsequent buckling in the context of droplet networks we evolve from an initial configuration consisting of two rows with different osmolarities. FIG. 5.1 shows ring closure for $N = 38$ total droplets. The initial osmolarity of the top row is $C_1 = 0.1$ (blue) and that of the bottom row is $C_2 = 1.0$ (red). After each row closes to form a ring there is still an osmolarity difference between the outer and inner rings, as can be seen from Fig.5.1(c). This residual osmolarity mismatch is followed by a ring buckling transition, as shown in Fig.5.1(e).

The final shape depends on the osmolarity difference and the number of droplets. In Fig. 5.2, we sketch the phase diagram for ring closure and buckling as a function of the

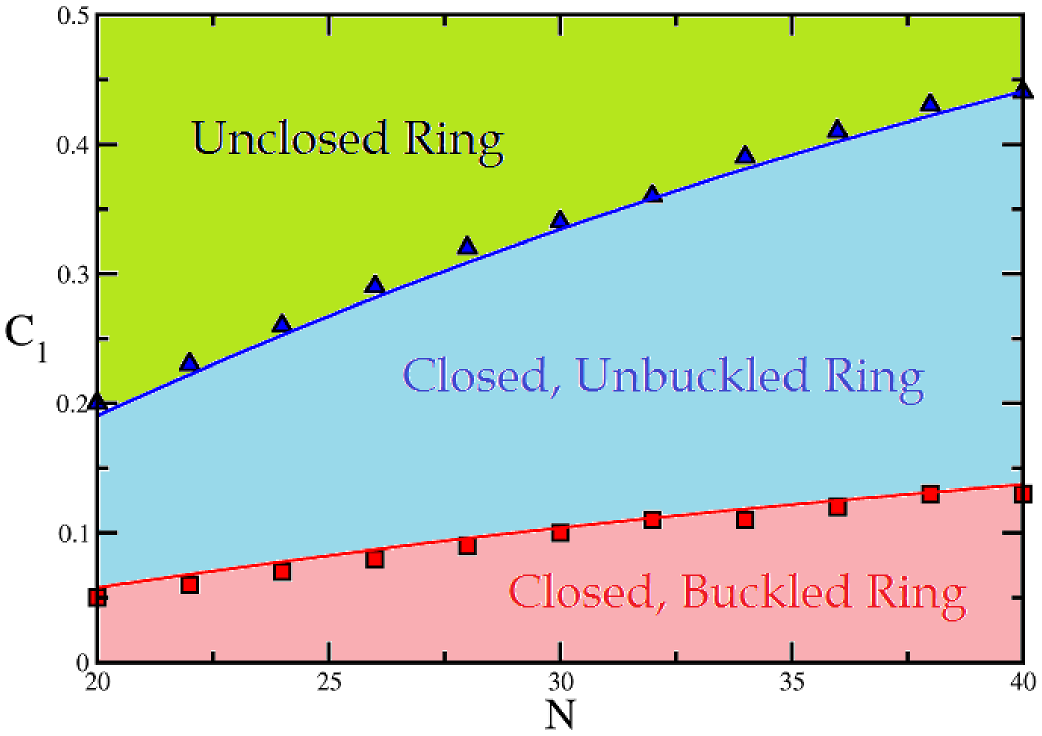

FIGURE 5.2: (Color online) Plot of the ring buckling phase diagram as a function of top row osmolarity C_1 and total number of droplets N. The bottom row osmolarity is fixed at $C_2 = 1.0$. The symbols, obtained from simulation, should be compared with lines showing analytical results.

top row osmolarity C_1 and the total number of droplets N. The bottom row osmolarity is fixed at $C_2 = 1.0$. There are three phases. For a given value of N, rings do not form at all until the osmolarity difference $\Delta C = C_2 - C_1$ exceeds a threshold. The threshold value is computed analytically as follows. For a range of ΔC one then finds smooth rings. For yet larger ΔC the closed ring buckles. An upper bound for the buckling transition can also be obtained analytically as follows. The larger N, the easier it is to form a ring and so the smaller is the threshold osmolarity difference for ring closure and subsequent buckling.

The initial configuration has two lines of N total droplets. The initial radius of each droplet is R_i and the final equilibrated radii of droplets are R_{1f} on the top row and R_{2f} on the bottom row. The initial osmolarity of the top row is C_{1i} and the bottom row C_{2i}, and the final equilibrated osmolarity is C_f. The amount of solute in each droplet is conserved. This implies

$$\begin{aligned} C_{1i}\frac{4}{3}\pi {R_i}^3 &= C_f\frac{4}{3}\pi {R_{1f}}^3, \\ C_{2i}\frac{4}{3}\pi {R_i}^3 &= C_f\frac{4}{3}\pi {R_{2f}}^3. \end{aligned} \tag{5.4}$$

The total amount of solution is also conserved:

$$2\left(\frac{4}{3}\pi {R_i}^3\right) = \frac{4}{3}\pi {R_{1f}}^3 + \frac{4}{3}\pi {R_{2f}}^3. \tag{5.5}$$

This yields

$$\begin{aligned} R_{1f} &= \left(\frac{2C_{1i}}{C_{1i}+C_{2i}}\right)^{\frac{1}{,}3} R_i \\ R_{2f} &= \left(\frac{2C_{2i}}{C_{1i}+C_{2i}}\right)^{\frac{1}{3}} R_i. \end{aligned} \tag{5.6}$$

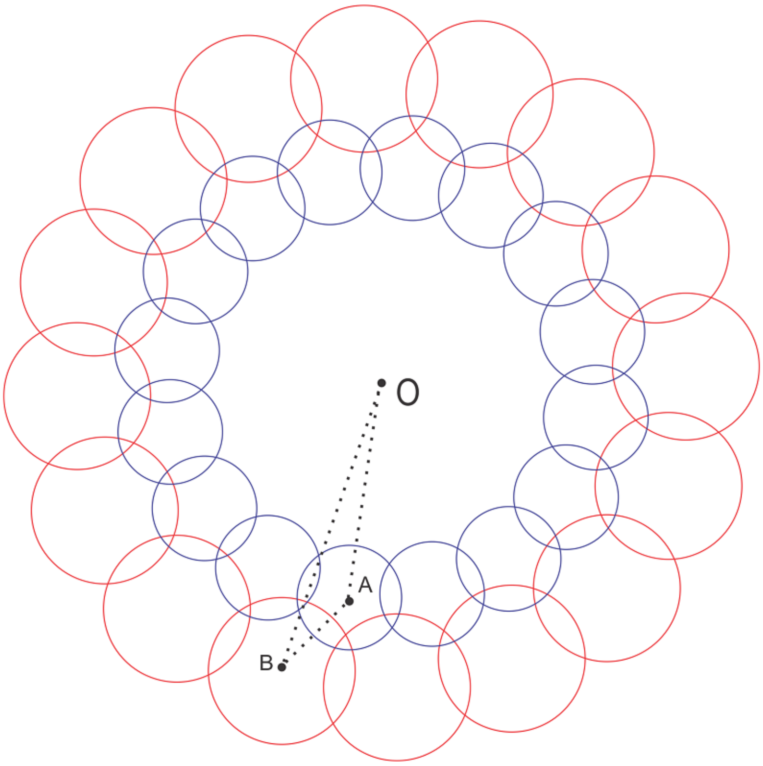

FIGURE 5.3: Schematic figure for the onset of ring formation.

To determine the condition for the onset of ring formation note that each row of droplets must have the same center of curvature, labeled as point O in Fig. 5.3. The distance between two neighboring droplets in the top(inner) row is $2lR_{1f}$, the distance between two neighboring droplets, one from the top row and the other one from the bottom row, is $l\left(R_{1f}+R_{2f}\right)$, and the distance between two neighboring droplets from the bottom row is $2lR_{2f}$, where $l = 0.8$ as shown in Fig. 5.3. In $\triangle OAB$, we have

$$\begin{aligned} |OA| &= (lR_{1f})\,/\sin\left(\frac{\pi}{(N/2)}\right) \\ |OB| &= (lR_{2f})\,/\sin\left(\frac{\pi}{(N/2)}\right) \\ |AB| &= l\,(R_{1f}+R_{2f}) \\ |AB|^2 &= |OA|^2+|OB|^2-2|OA||OB|\cos\left(\frac{\pi}{(N/2)}\right) \end{aligned} \tag{5.7}$$

This yields for onset condition of ring formation

$$(R_{1f}+R_{2f})^2 = \frac{R_{1f}^2+R_{2f}^2-2R_{1f}R_{2f}\cos\left(\frac{\pi}{(N/2)}\right)}{\sin^2\left(\frac{\pi}{(N/2)}\right)} \tag{5.8}$$

By combining equations 5.6 and 5.8 we can numerically solve for C_1 if given the value of N.

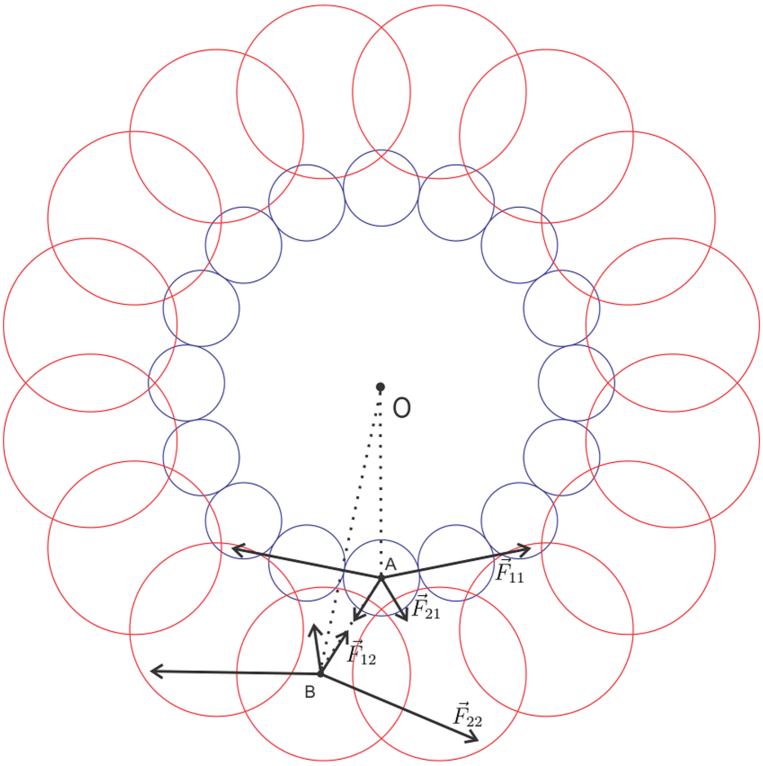

FIGURE 5.4: Schematic figure for the onset of ring buckling.

To determine the parameters for the onset of ring buckling where the inner droplets become separated, note that the distance between two neighboring droplets from the top(inner) row is $2R_{1f}$, the distance between two neighboring droplets one from the top row and the other one from the bottom row is $l_{12}\,(R_{1f}+R_{2f})$, and the distance between two neighboring droplets from the bottom row is $l_{22}\,(2R_{2f})$, as shown in Fig. 5.4. For a droplet from the inner row, the force exerted by each of the two neighboring droplets from the same row is $|\vec{F}_{11}| = (1.0 - l)\,(2R_{1f})$, and the force exerted by each of the two neighboring droplets from the outer row is $|\vec{F}_{21}| = (l_{12} - l)\,(R_{1f} + R_{2f})$, where $l = 0.8$. Those four forces balance each other, yielding

$$2|\vec{F}_{11}|\sin\left(\frac{\pi}{(N/2)}\right) = 2|\vec{F}_{21}|\frac{\sqrt{\left[l_{12}\,(R_{1f} + R_{2f})\right]^2 - (l_{22}R_{2f})^2}}{l_{12}\,(R_{1f} + R_{2f})} \tag{5.9}$$

so that

$$2\,(1.0 - l)\,(2R_{1f})\sin\left(\frac{\pi}{(N/2)}\right) = 2\,(l_{12} - l)\,(R_{1f} + R_{2f})\,\frac{\sqrt{\left[l_{12}\,(R_{1f} + R_{2f})\right]^2 - (l_{22}R_{2f})^2}}{l_{12}\,(R_{1f} + R_{2f})} \tag{5.10}$$

For a droplet from the outer row, the force exerted by each of the two neighboring droplets from the same row is $|\vec{F}_{22}| = (l - l_{22})\,(2R_{2f})$ and the force exerted by each of the two neighboring droplets from the inner row is $|\vec{F}_{12}| = (l_{12} - l)\,(R_{1f} + R_{2f})$, where $l = 0.8$. Those four forces balance each other, yielding

$$2|\vec{F}_{22}|\sin\left(\frac{\pi}{(N/2)}\right) = 2|\vec{F}_{12}|\frac{\sqrt{\left[l_{12}\,(R_{1f} + R_{2f})\right]^2 - (R_{1f})^2}}{l_{12}\,(R_{1f} + R_{2f})} \tag{5.11}$$

so that

$$2\,(l - l_{22})\,(2R_{2f})\sin\left(\frac{\pi}{(N/2)}\right) = 2\,(l_{12} - l)\,(R_{1f} + R_{2f})\,\frac{\sqrt{\left[l_{12}\,(R_{1f} + R_{2f})\right]^2 - (R_{1f})^2}}{l_{12}\,(R_{1f} + R_{2f})} \tag{5.12}$$

We also have

$$\begin{aligned}
|OA| &= (R_{1f})\,/\sin\left(\frac{\pi}{(N/2)}\right)\\
|OB| &= (l_{22}R_{2f})\,/\sin\left(\frac{\pi}{(N/2)}\right)\\
|AB| &= l_{12}\,(R_{1f} + R_{2f})\\
|AB|^2 &= |OA|^2 + |OB|^2 - 2|OA||OB|\cos\left(\frac{\pi}{(N/2)}\right)
\end{aligned} \tag{5.13}$$

The condition for the onset of ring buckling is thus

$$l_{12}^2\,(R_{1f} + R_{2f})^2 = \frac{R_{1f}^2 + l_{22}^2R_{2f}^2 - 2l_{22}R_{1f}R_{2f}\cos\left(\frac{\pi}{(N/2)}\right)}{\sin^2\left(\frac{\pi}{(N/2)}\right)}. \tag{5.14}$$

By combining equations 5.6, 5.10, 5.12 and 5.14, we can numerically solve for l_{12}, l_{22} and C_1 if given the value of N.

5.3.2 Spirals

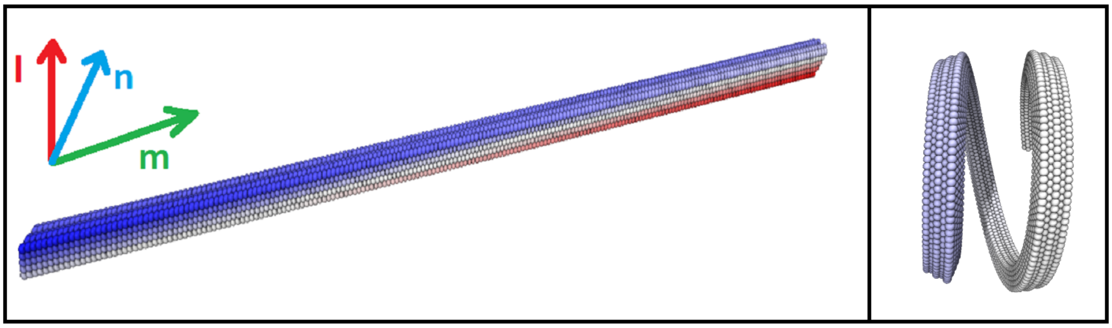

Figure 5.5: (Color online) Typical initial (left) and final (right) configurations for the formation of spirals.

We choose as initial state a $200 \times 5 \times 5$ rectangular slab (see Fig. 5.5). Each droplet can be indexed by integer orthogonal coordinates l, m, n, with $0 \leq m < 200$, $0 \leq n < 5$ and $0 \leq l < 5$. The initial osmolarity of each droplet is set to be

$$C_{mnl} = (1.0 - K_n\, n)\left(1.0 + K_l\, l \frac{(m-100)}{100}\right) , \tag{5.15}$$

where K_n and K_l are free parameters. We explore how spiral formation process depends on K_l and K_n for fixed slab size.

Fig. 5.6(a) shows how the radius of curvature of the spiral depends on K_l and K_n. K_n determines how efficiently the slab folds up in the $m - n$ plane. As K_n increases the rod folds up more effectively and the radius of curvature decreases. A positive value of K_l will make each part of the slab fold up differently in the l direction. If $K_l = 0$, for example, the two ends of the slab will fold and then meet each other, leading to a ring. Note that the radius of the spiral also decreases with increasing K_l, making folding more efficient.

Fig. 5.6(b) plots the pitch of the spiral as a function of K_l and K_n. The pitch depends mainly on K_n, with more efficient folding occurring at large K_n. There is a slight dependence on K_l.

5.3.3 Tetrahedra

A tetrahedron may be formed by choosing as initial droplet network a central triangle connected to three other triangles by hinges on each of its sides. We use four layers of droplets, all of osmolarity C_1, to create sufficiently rigid faces. For each hinge, the top two layers of droplets have osmolarity C_1, while the bottom two layers droplets have

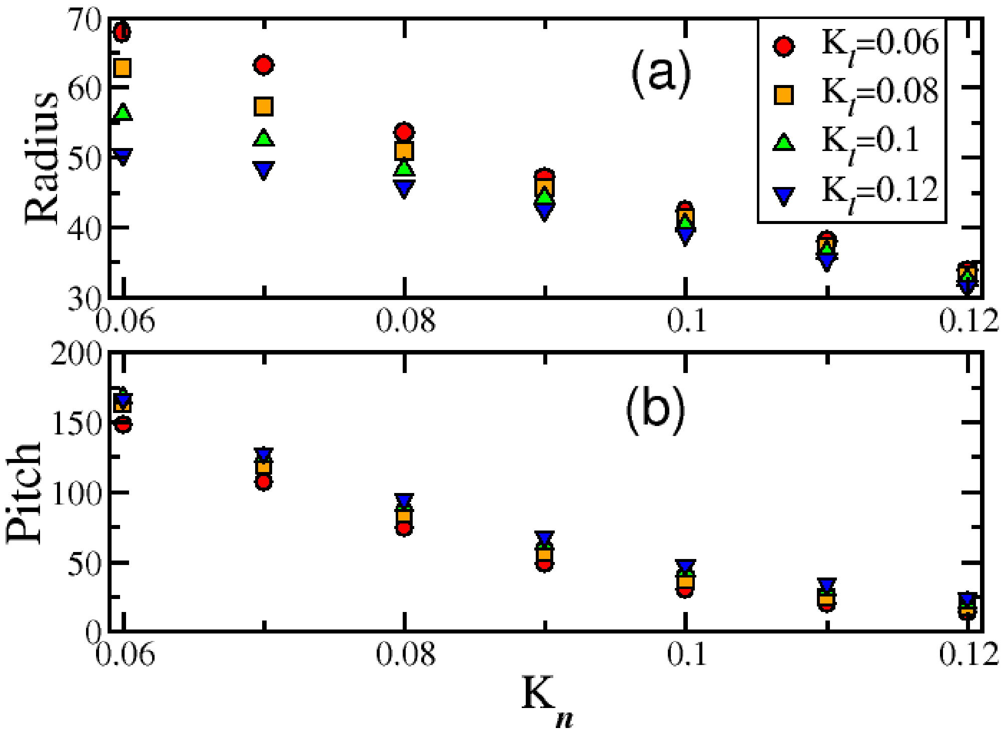

FIGURE 5.6: (Color online) (a) The radius of the spiral as a function of K_n for different K_ls. (b) The pitch of the spiral as a function of K_n for different K_ls.

osmolarity $C_2 > C_1$. The flow of water to the outer layers causes the hinges to bend upward, closing all faces into a tetrahedral shell (see Fig. 5.7).

The osmolarity difference must be tuned to achieve tetrahedral folding. If $C_1 = 1.0$ and $C_2 < 4.0$, the osmolarity difference is too small to drive tetrahedral closure. The critical osmolarity difference may be lowered or raised by using wider or thinner hinges respectively.

5.3.4 Reversible Folding

By adding an osmotic interaction with the environment we can realize a *reversible* folding-unfolding process, as shown in Fig. 5.8. To generate reversible folding we place part of the folded droplet network into a medium with higher osmolarity C_m ($C_m > C_{1,2}$) so that water will flow from the droplets on the bottom layer of the "flower" to the medium. More precisely, the bottom layer droplets located below a horizontal $x - y$ plane at $z = h$ are exposed to the higher osmolarity medium. As the flower folds, an

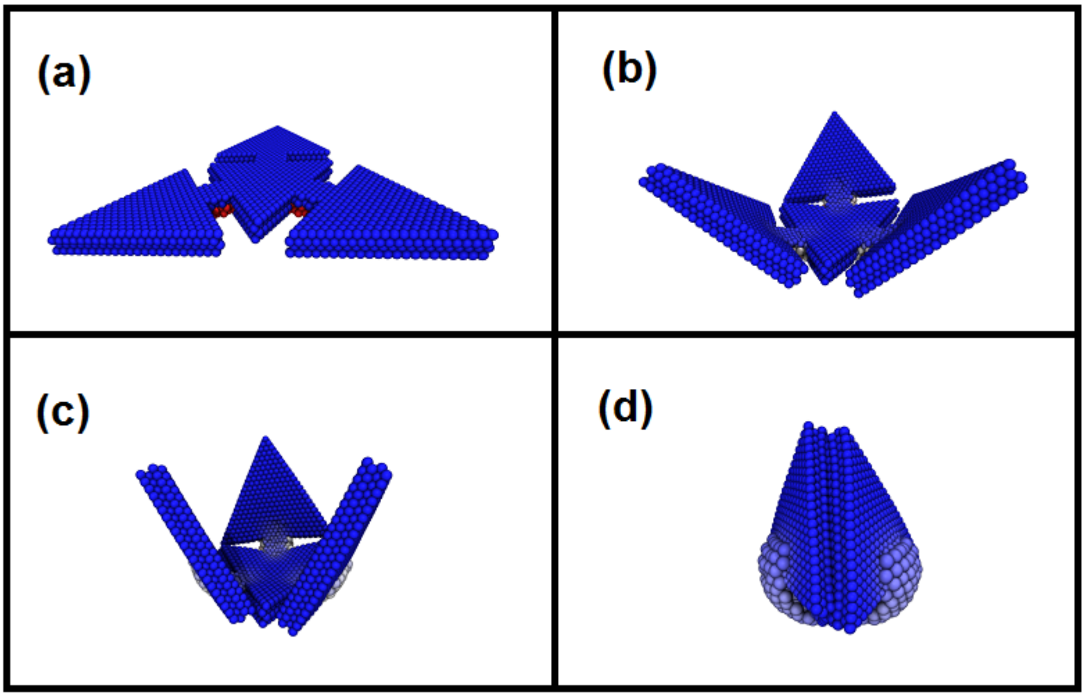

Figure 5.7: (Color online) (a)-(d) Forming a tetrahedral shell ($C_1 = 1.0$ and $C_2 = 5.0$). The color represents osmolarity with blue/red representing low/high osmolarity with white intermediate.

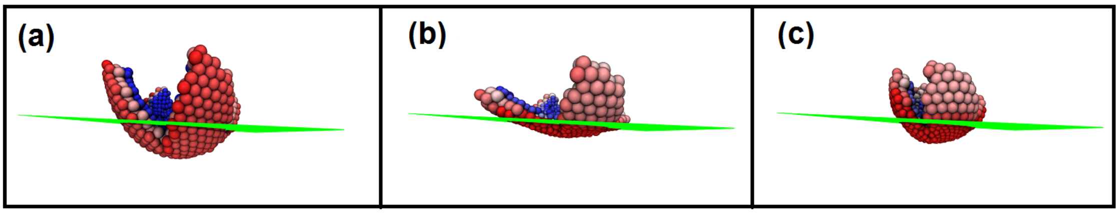

Figure 5.8: (Color online) (a)-(c) Three snapshots from the reversible folding process.

increasing number of bottom layer droplets naturally become exposed to the medium. They therefore lose water, to the surrounding medium, and start to unfold again. The overall volume of the unfolded flower also drops, preventing a complete reversal. As the bottom droplets continue losing water to the medium, the top droplets are also losing water to the bottom droplets. The detailed evolution depends on the the osmolarity difference and the total contact area through which the water is passing. Lower h, which means the smaller the contact area between the bottom droplets and the medium, and the smaller C_m, which means a smaller osmolarity difference, will lead to a slower rate of water transfer between the bottom droplets and the medium. For top layer osmolarity $C_{top} = 0.1$ and bottom layer osmolarity $C_{bottom} = 1.0$, one finds that the top layer loses more water to the bottom layer than the bottom layer itself loses to the surrounding medium. This eventually reverses the unfolding and the structure starts to fold once again. As discussed in Appendix **??**, our simulation uses the same algorithm as before, other than a modification of Fick's first law (Eq. (2)) resulting from the separation of time scales between mechanical relaxation and water transfer.

To characterize the reversibility of the system, we define reversibility as

$$\rho = \left(D_{max\_before} + D_{max\_after} - 2D_{min}\right) / K_{norm}, \tag{5.16}$$

where D_{min} is the minimum depth of unfolding, D_{max_before} is the maximum depth of the flower before the "flower" unfolds, D_{max_after} is the maximum depth of the flower after it reaches a minimum and refolds, and K_{norm} is a normalization constant. For $\rho = 1$, the system is fully reversible in the sense that the flower opens out fully before folding back up again, while for $\rho = 0$ there is no reversal.

Fig. 5.9 shows the dependence of ρ on the horizontal plane's $z = h$ coordinate and the media's osmolarity C_m. As the horizontal plane rises, the reversibility increases since there are more bottom droplets in contact with the medium. The reversibility also increases with a rise in the media's osmolarity C_m.

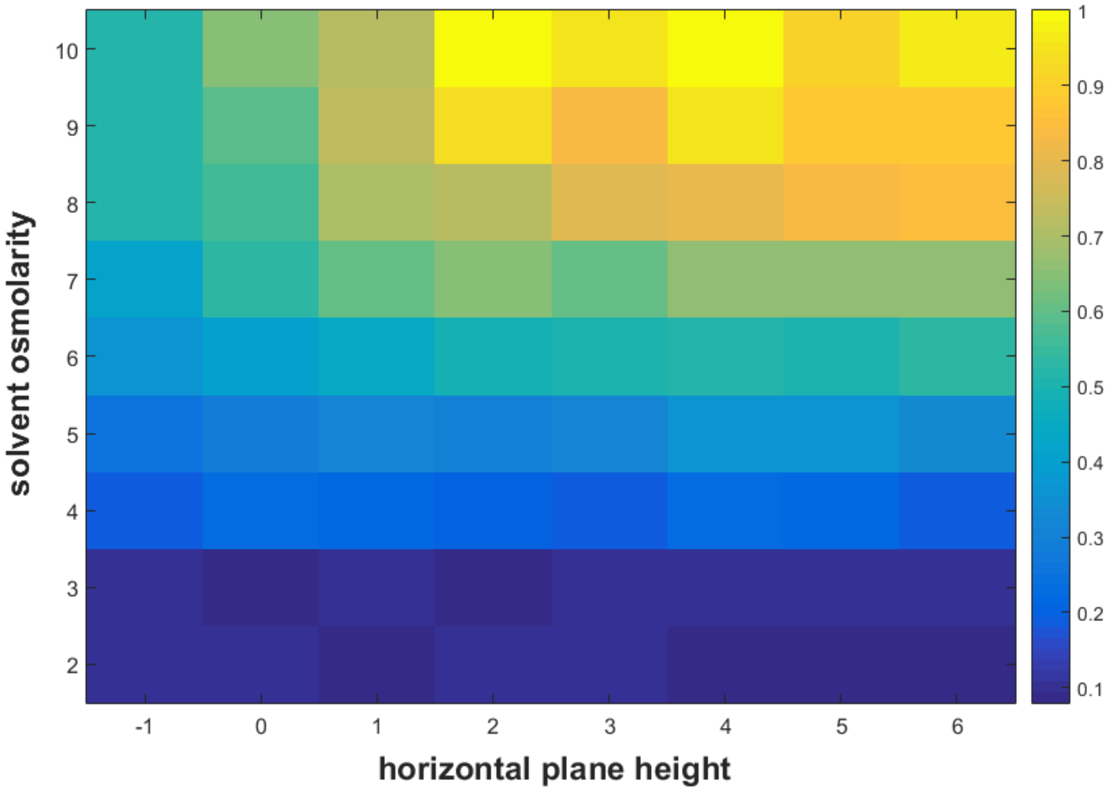

FIGURE 5.9: (Color online) Reversibility dependence on the z coordinate of the horizontal plane and the osmolarity of the surrounding medium.

5.4 Discussion

We have explored the formation of rings, spirals, and tetrahedra in droplet networks in which the individual droplets are programmed with different osmolarities. These osmolarity gradients create local flows of water that lead to global shape change. For ring formation, we find a subsequent buckling transition for large enough osmolarity difference. For spiral formation, we determine how the size of the gradients in each of the three dimensions affects both the radius and pitch of the spiral. Finally, for the formation of tetrahedra, there must be a large enough osmolarity difference between the triangles and the hinges for the edges of the triangles to meet and form a closed tetrahedron.

In the flower-closing system we have also shown how to reverse the large-scale shape change so that the four-petaled flower folds, unfolds, and folds back again. This folding-unfolding-refolding processes capitalizes on the interaction between part of the droplet network and the surrounding medium (environment) and relies on the medium having an osmolarity larger than the osmolarities in the droplet network. This mechanism is a first step towards osmotic robotics. The reversibility of our model is limited, however, because (1) the flower-shaped droplet network folds, unfolds, and folds again only once and (2) the volume of the final state of the folded "flower" (a hollow shell) is smaller than if it had just simply folded.

To address the limited reversibility of our model, a recent study [138] extends osmosis to active solutes containing, for example, self-propelled colloids [139–142] or hot nanoparticles [143, 144]. The study finds that active solute activity increases the osmotic pressure and can also expel solvent from the solution. By using active solutes, the solvent can be controlled to flow from the higher osmolarity to lower, which is reversed from the usual passive solute situation. The use of reverse osmosis via active solutes could make the folding-unfolding process completely reversible. Further study, however, is needed to assess the feasibility of active solutes to achieve such a goal.

Appendix A

Effective medium theory

How does one compute the macroscopic elastic properties of a disordered network? Instead of considering the disordered system explicitly, one can study the effective medium mechanical response for such disordered networks following the mean field theory developed in [18] for central force networks and [117] for filament bending networks.

For instance, one can map a 2D disorderd spring network to an effective network where all of the springs are present and all have the same effective spring constant α_m. The goal of this theory is to make this constructed effective medium, or ordered network, have the same mechanical response to a given deformation field as the depleted network under consideration. The effective elastic constants are determined by requiring that strain fluctuations produced in the original, ordered network by randomly cutting filaments vanish when averaged over the entire network.

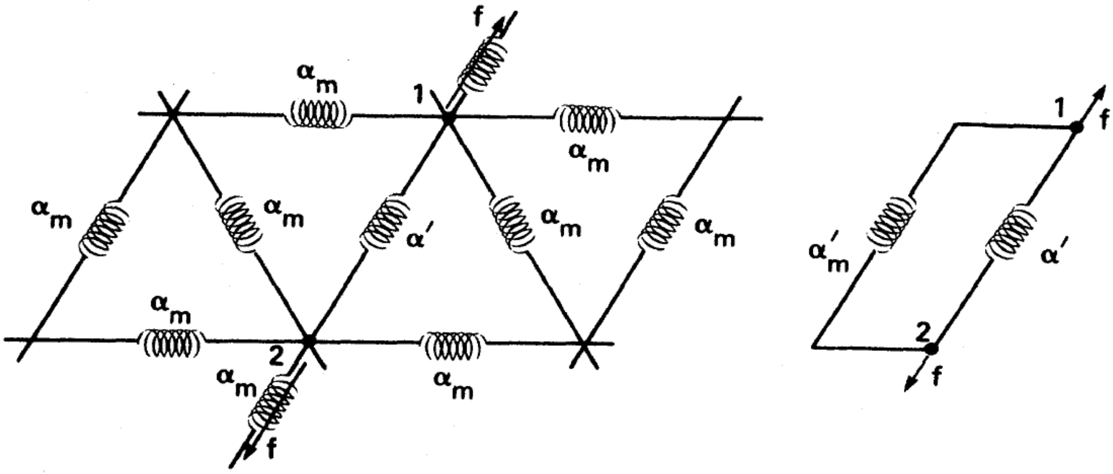

FIGURE A.1: Showing the notation for constructing the effective medium theory. [18]

The elastic energy of the strained network, arising from stretching of the constituent filaments, can be written in terms of the displacement vector $\mathbf{u}_i$ at each lattice site i. To quadratic order in $\mathbf{u}$, the stretching energy E_s is

$$E_s = \frac{1}{2}\alpha_m \sum_{<ij>} (\mathbf{u}_{ij}.\hat{\mathbf{r}}_{ij})^2 \tag{A.1}$$

where $\hat{\mathbf{r}_{ij}}$ is a unit vector directed from the ith to the jth equilibrium lattice site, and $\mathbf{u}_{ij}$ is the difference in the strain field between those lattice sites.

Then it is time to determine the spring constant α_m of this spatially uniform effective system. First we can apply a uniform dilation to the uniform system with spring constant α_m so that all bonds are stretched by δl. Then we will replace a single bond connecting points i and j by another spring with spring constant α', the virtual force needed to fix the positions of i and j is $f = \delta l\,(\alpha_m - \alpha')$.

If f were applied to the same bond in the unstrained network when all the springs are α_m, there will be an effective spring constant α_m/α^* takes account of all the connections between i and j including the direct one in this uniform system, where $0 < a^* < 1$ and will be calculated later. If we remove the α_m spring between i and j, the effective spring between i and j is $\alpha'_m = \alpha_m/\alpha^* - \alpha_m$. If then α' is added in parallel to α'_m and the force f applied, then the resulting change in relative displacement between i and j would be $f/\left(\alpha'_m + \alpha'\right) = f/\left(\alpha_m/a^* - \alpha_m + \alpha'\right) = \delta l\left(\alpha_m - \alpha'\right)/\left(\alpha_m/a^* - \alpha_m + \alpha'\right)$.

From the superposition principle, the extra displacement δu of the bond ij due to the change in that filament's spring constant in the dilated network is the same as its extension in response to the force f applied to it. Therefore, this additional displacement, or fluctuation, is

$$\delta u = \frac{(\alpha_m - \alpha')\,\delta l}{(\alpha_m/a^* - \alpha_m + \alpha')} \tag{A.2}$$

The effective-medium result is obtained by choosing α_m so that the average value $< \delta u >$ of δu is zero to give

$$< \frac{(\alpha_m - \alpha')}{(\alpha_m/a^* - \alpha_m + \alpha')} >= 0 \tag{A.3}$$

.

For a distribution of spring constant α': $P(\alpha') = p\delta(\alpha' - \alpha) + (1-p)\delta(\alpha' - 0)$, where $1-p$ is the probability of a cut bond and $\delta(...)$ is the Dirac delta function, we find a spatially homogeneous effective medium having spring constant α_m given by

$$\frac{\alpha_m}{\alpha} = \begin{cases} \frac{p-a^*}{1-a^*} & \text{if } p > a^*, \\ 0 & \text{if } p \leq a^*. \end{cases} \tag{A.4}$$

The value of a^* can be written in terms of the dynamical matrix $\mathbf{D}(q)$ as

$$a^* = \frac{1}{3}\sum_q \mathbf{Tr}\left[\mathbf{D}(q)\cdot\mathbf{D}^{-1}(q)\right] = \frac{2}{3} \tag{A.5}$$

where the sum is over the first Brillouin zone. Here the dynamical matrix is given by

$$\begin{aligned}
\mathbf{D}(q) =& \alpha_m \sum_{<ij>}\left[1-e^{-i\mathbf{q}.\hat{\mathbf{r}}_{ij}}\right]\hat{\mathbf{r}}_{ij}\hat{\mathbf{r}}_{ij} \\
=& \alpha_m \begin{pmatrix} -\left(2\cos\left(q_x\right)+\cos\left(\frac{q_x}{2}\right)\cos\left(\frac{\sqrt{3}}{2}q_y\right)-3\right) & \sqrt{3}\sin\left(\frac{q_x}{2}\right)\sin\left(\frac{\sqrt{3}}{2}q_y\right) \\ \sqrt{3}\sin\left(\frac{q_x}{2}\right)\sin\left(\frac{\sqrt{3}}{2}q_y\right) & -3\left(\cos\left(\frac{q_x}{2}\right)\cos\left(\frac{\sqrt{3}}{2}q_y\right)-1\right) \end{pmatrix}
\end{aligned} \tag{A.6}$$

Appendix B

Conjugate gradient method

The conjugate gradient(CG) method is one of the most popular and well known iterative techniques for solving sparse symmetric positive definite(SPD) systems of linear equations [145]. It was originally developed as a direct method, but became popular for its properties as an iterative method.

A symmetric matrix A is SPD(symmetric positive definite) if $x^T Ax > 0 \ \forall x \in \Omega$, or equivalently if all the eigenvalues of A are positive.

B.1 The quadratic Form

A quadratic form is simply a scalar, quadratic function of a vector with the form

$$f(s) = \frac{1}{2}x^T Ax - b^T x + c \tag{B.1}$$

where A is a matrix, x and b are vectors, and c is a scalar constant. The minimizer x^* of the function f is given as the point where the gradient of the function is equal to zero. Direct calculation gives

$$\nabla f(x^*) = Ax^* - b = 0 \tag{B.2}$$

or

$$Ax^* = b \tag{B.3}$$

B.2 Line search methods

The line search methods are a large family of iterative optimization methods where the iteration is given by

$$x_{k+1} = x_k + \alpha_k p_k \tag{B.4}$$

The idea is to choose an initial position x_0, and for each step walk along a direction (a line) so that $f(x_{k+1}) < f(x_k)$. The different methods have different strategies for choosing the search direction p_k, and the step length α_k.

B.2.1 Steepest descent method

The steepest descent method is perhaps the most intuitive and basic line search method. The gradient of a function is a vector giving the direction along which the function increases the most. The method of steepest descent is based on the strategy that in any given point x, the search direction given by the negative gradient of the function $f(x)$, the locally optimal search direction, is the direction of steepest descent. The gradient of $f(x)$ is $Ax - b$, called the residual r of the system.

After determining the direction, we still need to know how far to walk along it. THe natural choice is to walk until the function no longer descend, and an expression for the optimal step length α_k is

$$\alpha_k = \frac{\nabla f(x_k)^T \nabla f(x_k)}{\nabla f(x_k)^T A \nabla f(x_k)} = \frac{r_k^T r_k}{r_k^T A r_k} \tag{B.5}$$

by inserting the expression for the next step $x_{k+1} = x_k - \alpha \nabla f(x_k)$ into the quadratic function and minimizing with respect to α. We repeat this for every step, taking the gradient of f in the next point x_{k+1} and by finding a new step length. So this leads to search directions to be orthogonal to each other, as shown in Fig B.1.

This method's zigzag behaviour is not the optimal and fastest path towards the minimum, since each successive step is not different enough from the others.

B.2.2 Conjugate gradient method

We need a method that can use the information from the previous steps in order to avoid running back and forth across the valley of the contour plots. The solution is to make the search directions A-orthogonal instead of orthogonal. Two vectors p_i and p_j

are A-orthogonal, or conjugate, if

$$p_i^T A p_j = 0, \forall i \neq j \tag{B.6}$$

A set of n such vectors are linearly independent and hence span the whole space $\mathbb{R}^n$. We can minimize the quadratic function f in n steps by successively minimizing it along each of the directions.

Since the set of conjugate vectors acts as a basis for $\mathbb{R}^n$, we can express the difference between the exact solution x^* and our first guess x_0 as a linear combination of the conjugate vectors:

$$x^* - x^0 = \sum_{k=0}^{n-1} \sigma_k p_k \tag{B.7}$$

Because of the conjugacy property, the coefficients σ_k are found out to be the same as the step lengths α_k that minimize the quadratic function f along $x_k + \alpha_k p_k$, so

$$x^* = x^0 + \sum_{k=0}^{n-1} \alpha_k p_k \tag{B.8}$$

In practice we need a way to create a set of A-orthogonal search directions. It turns out there is a conjugate direction method with property that each new conjugate vector p_k can be computed by using only the previous vector p_{k-1}. This method works its magic by choosing each new direction p_k as a linear combination of the negative residual $-r_k$ and the previous search vector p_{k_1}. As we know for the quadratic function the negative residual is equal to the negative gradient direction, we get a name for this method: *conjugate gradient method.*

The direction for the next step is

$$p_k = -r_k + \beta_k p_{k-1} \tag{B.9}$$

where β_k is found by imposing the condition that $p_{k-1}^T A p_k$ and has expression

$$\beta_k = \frac{r_k^T A p_{k-1}}{p_{k-1}^T A p_{k-1}} = \frac{r_k^T r_k}{r_{k-1}^T r_{k-1}} \tag{B.10}$$

A comparison of the conjugate gradient method and the steepest descent method is shown in Fig B.1.

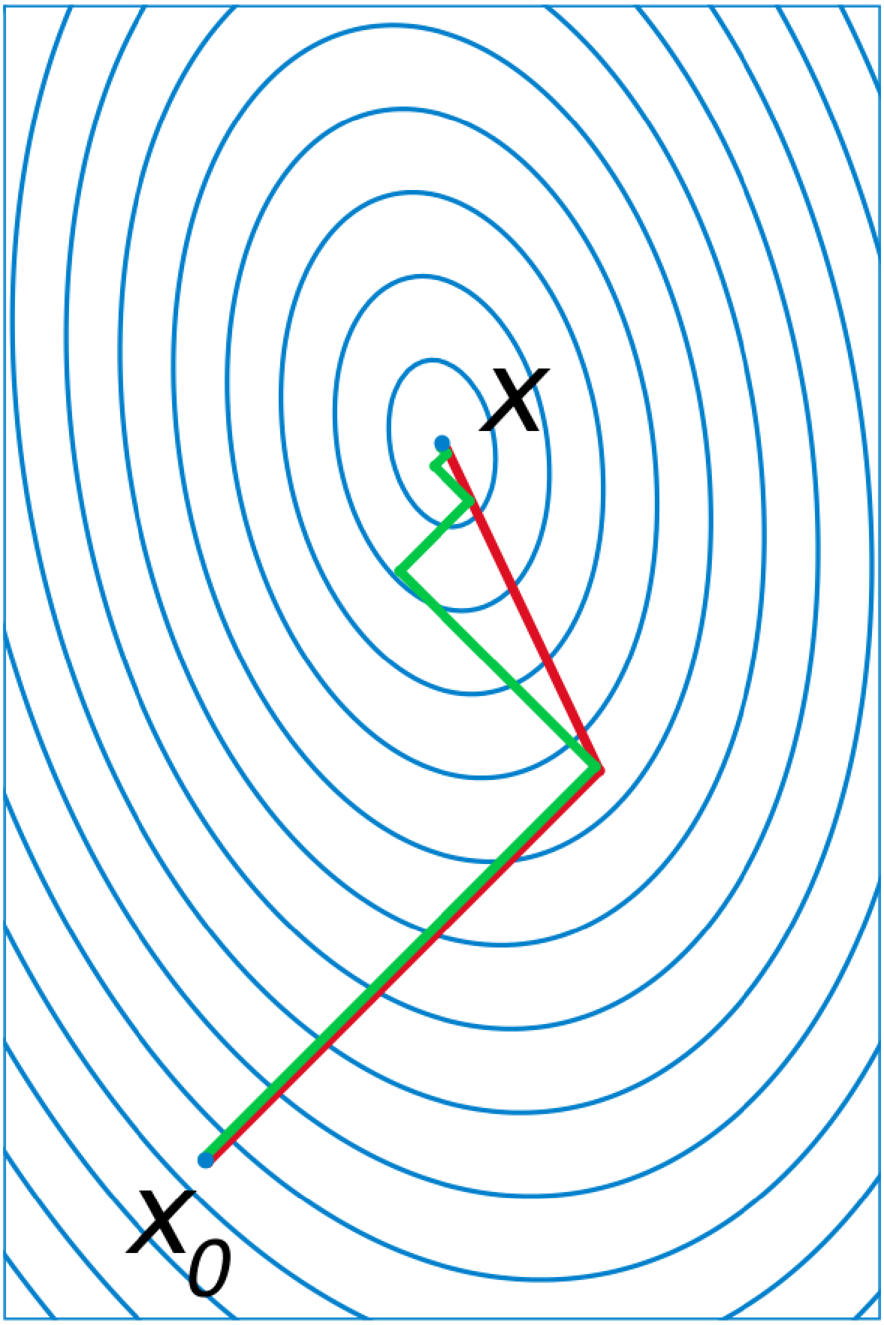

FIGURE B.1: The contour plot of a function, with the steps of the steepest descent method in green and of the conjugate gradient method in red. [145]

Appendix C

Metropolis Monte Carlo method

The Metropolis Monte Carlo method [146] is a computational approach for generating a set of N configurations of the system $\xi_1, \xi_2, \xi_3, ..., \xi_N$ such that

$$\lim_{N \to \infty} \frac{N_\xi}{N} = P(\xi) \tag{C.1}$$

where $P(\xi)$ is the Boltzmann distribution $P(\xi) = Z^{-1} exp\left[-\frac{E(\xi)}{k_B T}\right]$, k_B is the Boltzmann constant, T is the effective temperature, Z is the partition function and N_ξ is the number of configurations ξ.

The Metropolis Monte Carlo algorithm can be described as follows:

Step 1: Pick a configuration ξ_n of the system.

Step 2: Pick a trial configurationξ_t (usually a configuration similar to ξ_n) and compute the probability ratio $R = \frac{P(\xi_t)}{P(\xi_n)}$. Pick a random number p with value between 0 and 1. Make $\xi_{n+1} = \xi_t$ if $p \leq R$. Otherwise, make $\xi_{n+1} = \xi_n$.

Step 3: Go to (2) replacing ξ_n by ξ_{n+1}.

Step 3 is repeated N times, where N is a sufficiently large number. Note that, according to step 2, the probability of accepting a trial configuration ξ_t by making $\xi_{n+1} = \xi_t$ from a configuration ξ_n is

$$P_{\xi_n, \xi_t} = \begin{cases} \frac{P(\xi_t)}{P(\xi_n)} & when\ P(\xi_t) < P(\xi_n) \\ 1 & otherwise \end{cases} \tag{C.2}$$

Appendix D

Details of variational calculation for initiation stage in the Monge representation

To examine the equilibrium shape of the cell membrane with clathrin indirectly attached in a localized region (the invagination site), we consider the following energy [3]:

$$E_{init} = \sum_{i=1,2} \int dS_i \left[2\kappa_i \left(H_i - C_{0i} \right)^2 + \kappa_{G_i} K_i + \sigma_i \right] \tag{D.1}$$

where $i = 1$ denotes the Sla1/Ent1/2-bound membrane (to which the clathrin then attaches) and $i = 2$ denotes the bare membrane. In addition, κ_1 denotes the bending rigidity of component 1, while κ_2 denotes the bending rigidity of component 2. The respective spontaneous curvatures are denoted by C_{01} and C_{02} respectively. κ_{G_1} denotes the saddle-splay modulus of component 1, while κ_{G_2} denotes the saddle-splay modulus of component 2. Finally, σ denotes the surface tension.

We represent the membrane shape using the so-called Monge representation such that each point on the membrane in three-dimensional space is given as

$$\vec{r} = \left(x, y, z\left(x, y \right) \right). \tag{D.2}$$

It is straightforward to show that the differential area element is

$$dS = \sqrt{1 + \left(\nabla z \right)^2} dxdy, \tag{D.3}$$

and the mean curvature is

$$H = \frac{1}{2}\nabla\left(\frac{\nabla z}{\sqrt{1+(\nabla z)^2}}\right). \tag{D.4}$$

In the small gradient approximation, or $|\nabla z| \ll 1$,

$$dS \approx \left(1 + \frac{1}{2}(\nabla z)^2\right) dxdy, \tag{D.5}$$

and

$$H \approx \frac{1}{2}\Delta z, \tag{D.6}$$

where $\Delta z = \frac{\partial^2 z}{\partial x^2} + \frac{\partial^2 z}{\partial y^2}$ is the Laplacian. Assuming the system is axisymmetric $z = z\left(\sqrt{x^2+y^2}\right) \equiv z(r)$, we write the Laplacian in the cylindrical coordinates as

$$\Delta z = \frac{1}{r}\frac{dz}{dr} + \frac{d^2 z}{dr^2}, \tag{D.7}$$

where r is the distance from the origin, which we set to coincide with the center of a circular membrane.

Additionally, the Gaussian curvature is given by

$$K = \frac{1}{r}\frac{dz}{dr}\frac{d^2 z}{dr^2}. \tag{D.8}$$

The energy can now be written in the approximate form

$$\begin{aligned}
E_{init}[z(r)] &\approx \sum_{i=1,2}\int_{R_{i-1}}^{R_i} 2\pi r\left[2\kappa_i\left(\frac{1}{2}\Delta z - C_{0i}\right)^2 + \kappa_{G_i}\left(\frac{1}{r}\frac{dz}{dr}\frac{d^2 z}{dr^2}\right) + \sigma_i\right]\left(1+\frac{1}{2}(\nabla z)^2\right) dr \\
&\approx \sum_{i=1,2}\int_{R_{i-1}}^{R_i} \pi\kappa_i r\left[(\Delta z)^2 - 4C_{0i}\Delta z + \left(2C_{0i}^2 + \frac{\sigma_i}{\kappa_i}\right)(\nabla z)^2 + \left(4C_{0i}^2 + 2\frac{\sigma_i}{\kappa_i}\right)\right] dr \\
&\quad + \sum_{i=1,2}\int_{R_{i-1}}^{R_i} 2\pi\kappa_{G_i}\left(\frac{dz}{dr}\frac{d^2 z}{dr^2}\right) dr
\end{aligned} \tag{D.9}$$

where $R_0 = 0$. Next, we fix the area of component 1 (the Sla1/Ent1/2 attached domain) to be area A by introducing a Lagrange multiplier and also consider line tension at the interface between the two components/domains, then

$$\begin{aligned}E_{init}\left[z\left(r\right)\right] = &\sum_{i=1,2}\int_{R_{i-1}}^{R_i} \pi\kappa_i r\left[(\Delta z)^2 - 4C_{0i}\Delta z + \left(2C_{0i}^2 + \frac{\sigma_i}{\kappa_i}\right)(\nabla z)^2 + \left(4C_{0i}^2 + 2\frac{\sigma_i}{\kappa_i}\right)\right] dr \\ &+ \sum_{i=1,2}\int_{R_{i-1}}^{R_i} 2\pi\kappa_{G_i}\left(\frac{dz}{dr}\frac{d^2z}{dr^2}\right) dr + \sigma_0\left(2\pi\int_0^{R_1}\left(1+\frac{1}{2}(\nabla z_1)^2\right) r dr - A\right) + \gamma 2\pi R_1\end{aligned} \tag{D.10}$$

We define $z' \equiv \frac{dz}{dr}, z'' \equiv \frac{d^2z}{dr^2}, \xi_1^2 = 2C_{01}^2 + \dfrac{\sigma_1+\sigma_0}{\kappa_1}, \xi_2^2 = 2C_{02}^2 + \dfrac{\sigma_2}{\kappa_2}$ such that the Lagrangian for each component becomes

$$\begin{aligned}\mathcal{L}_1 &= \pi\kappa_1 r\left[\left(\frac{1}{r}{z_1}' + {z_1}''\right)^2 - 4C_{01}\left(\frac{1}{r}{z_1}' + {z_1}''\right) + \xi_1^2({z_1}')^2 + 2\xi_1^2\right] + 2\pi\kappa_{G_1}{z_1}'{z_1}'' + 2\pi\gamma r\delta(r-R_1) \\ \mathcal{L}_2 &= \pi\kappa_2 r\left[\left(\frac{1}{r}{z_2}' + {z_2}''\right)^2 - 4C_{02}\left(\frac{1}{r}{z_2}' + {z_2}''\right) + \xi_2^2({z_2}')^2 + 2\xi_2^2\right] + 2\pi\kappa_{G_2}{z_2}'{z_2}''\end{aligned} \tag{D.11}$$

We now proceed with the variation of the Lagrangian, or $\delta E_{init}\left[z\left(r\right)\right] = \delta\int_0^{R_1}\mathcal{L}_1 dr + \delta\int_{R_1}^{R_2}\mathcal{L}_2 dr$. Specifically, we have

$$\begin{aligned}\delta\int_0^{R_1}\mathcal{L}_1 dr = &\left[\mathcal{L}_1 - {z_1}'\left(\frac{\partial\mathcal{L}_1}{\partial {z_1}'} - \frac{d}{dr}\frac{\partial\mathcal{L}_1}{\partial {z_1}''}\right) - {z_1}''\frac{\partial\mathcal{L}_1}{\partial {z_1}''}\right]\Bigg|_{r=R_1}\delta R_1 \\ &+ \int_0^{R1}\left(\frac{\partial\mathcal{L}_1}{\partial z_1} - \frac{d}{dr}\frac{\partial\mathcal{L}_1}{\partial {z_1}'} + \frac{d^2}{dr^2}\frac{\partial\mathcal{L}_1}{\partial {z_1}''}\right)\delta z_1 dr + \left(\frac{\partial\mathcal{L}_1}{\partial {z_1}'} - \frac{d}{dr}\frac{\partial\mathcal{L}_1}{\partial {z_1}''}\right)\Bigg|_{r=R_1}\delta z_1(R_1) \\ &- \left(\frac{\partial\mathcal{L}_1}{\partial {z_1}'} - \frac{d}{dr}\frac{\partial\mathcal{L}_1}{\partial {z_1}''}\right)\Bigg|_{r=0}\delta z_1(0) + \frac{\partial\mathcal{L}_1}{\partial {z_1}''}\Bigg|_{r=R_1}\delta {z_1}'(R_1),\end{aligned} \tag{D.12}$$

and

$$\begin{aligned}\delta\int_{R_1}^{R_2}\mathcal{L}_2 dr = &\left[\mathcal{L}_2 - {z_2}'\left(\frac{\partial\mathcal{L}_2}{\partial {z_2}'} - \frac{d}{dr}\frac{\partial\mathcal{L}_2}{\partial {z_2}''}\right) - {z_2}''\frac{\partial\mathcal{L}_2}{\partial {z_2}''}\right]\Bigg|_{r=R_2}\delta R_2 \\ &- \left[\mathcal{L}_2 - {z_2}'\left(\frac{\partial\mathcal{L}_2}{\partial {z_2}'} - \frac{d}{dr}\frac{\partial\mathcal{L}_2}{\partial {z_2}''}\right) - {z_2}''\frac{\partial\mathcal{L}_2}{\partial {z_2}''}\right]\Bigg|_{r=R_1}\delta R_1 \\ &+ \int_{R_1}^{R2}\left(\frac{\partial\mathcal{L}_2}{\partial z_2} - \frac{d}{dr}\frac{\partial\mathcal{L}_2}{\partial {z_2}'} + \frac{d^2}{dr^2}\frac{\partial\mathcal{L}_2}{\partial {z_2}''}\right)\delta z_2 dr + \left(\frac{\partial\mathcal{L}_2}{\partial {z_2}'} - \frac{d}{dr}\frac{\partial\mathcal{L}_2}{\partial {z_2}''}\right)\Bigg|_{r=R_2}\delta z_2(R_2) \\ &- \left(\frac{\partial\mathcal{L}_2}{\partial {z_2}'} - \frac{d}{dr}\frac{\partial\mathcal{L}_2}{\partial {z_1}''}\right)\Bigg|_{r=R_1}\delta z_2(R_1) + \frac{\partial\mathcal{L}_2}{\partial {z_2}''}\Bigg|_{r=R_2}\delta {z_2}'(R_2) - \frac{\partial\mathcal{L}_2}{\partial {z_2}''}\Bigg|_{r=R_1}\delta {z_1}'(R_1).\end{aligned} \tag{D.13}$$

So,

$$
\begin{aligned}
\delta E_{init}\left[z\left(r\right)\right] = & \int_0^{R1}\left(\frac{\partial\mathcal{L}_1}{\partial z_1}-\frac{d}{dr}\frac{\partial\mathcal{L}_1}{\partial {z_1}'}+\frac{d^2}{dr^2}\frac{\partial\mathcal{L}_1}{\partial {z_1}''}\right)\delta z_1 dr+\int_{R_1}^{R2}\left(\frac{\partial\mathcal{L}_2}{\partial z_2}-\frac{d}{dr}\frac{\partial\mathcal{L}_2}{\partial {z_2}'}+\frac{d^2}{dr^2}\frac{\partial\mathcal{L}_2}{\partial {z_2}''}\right)\delta z_2 dr \\
& + \left.\left[\mathcal{L}_1-{z_1}'\left(\frac{\partial\mathcal{L}_1}{\partial {z_1}'}-\frac{d}{dr}\frac{\partial\mathcal{L}_1}{\partial {z_1}''}\right)-{z_1}''\frac{\partial\mathcal{L}_1}{\partial {z_1}''}\right]\right|_{r=R_1}\delta R_1 \\
& - \left.\left[\mathcal{L}_2-{z_2}'\left(\frac{\partial\mathcal{L}_2}{\partial {z_2}'}-\frac{d}{dr}\frac{\partial\mathcal{L}_2}{\partial {z_2}''}\right)-{z_2}''\frac{\partial\mathcal{L}_2}{\partial {z_2}''}\right]\right|_{r=R_1}\delta R_1 \\
& + \left.\left[\mathcal{L}_2-{z_2}'\left(\frac{\partial\mathcal{L}_2}{\partial {z_2}'}-\frac{d}{dr}\frac{\partial\mathcal{L}_2}{\partial {z_2}''}\right)-{z_2}''\frac{\partial\mathcal{L}_2}{\partial {z_2}''}\right]\right|_{r=R_2}\delta R_2 \\
& + \left.\left[\left(\frac{\partial\mathcal{L}_1}{\partial {z_1}'}-\frac{d}{dr}\frac{\partial\mathcal{L}_1}{\partial {z_1}''}\right)-\left(\frac{\partial\mathcal{L}_2}{\partial {z_2}'}-\frac{d}{dr}\frac{\partial\mathcal{L}_2}{\partial {z_2}''}\right)\right]\right|_{r=R_1}\delta z(R_1) \\
& + \left.\left[\frac{\partial\mathcal{L}_1}{\partial {z_1}''}-\frac{\partial\mathcal{L}_2}{\partial {z_2}''}\right]\right|_{r=R_1}\delta z'(R_1)-\left.\left(\frac{\partial\mathcal{L}_1}{\partial {z_1}'}-\frac{d}{dr}\frac{\partial\mathcal{L}_1}{\partial {z_1}''}\right)\right|_{r=0}\delta z_1(0) \\
& + \left.\frac{\partial\mathcal{L}_2}{\partial {z_2}''}\right|_{r=R_2}\delta {z_2}'(R_2)+\left.\left(\frac{\partial\mathcal{L}_2}{\partial {z_2}'}-\frac{d}{dr}\frac{\partial\mathcal{L}_2}{\partial {z_2}''}\right)\right|_{r=R_2}\delta z_2(R_2),
\end{aligned}
\tag{D.14}
$$

where we assume $z_1(R_1)=z_2(R_1)=z(R_1)$ and ${z_1}'(R_1)={z_2}'(R_1)=z'(R_1)$.

Appendix E

Pearling instability analysis

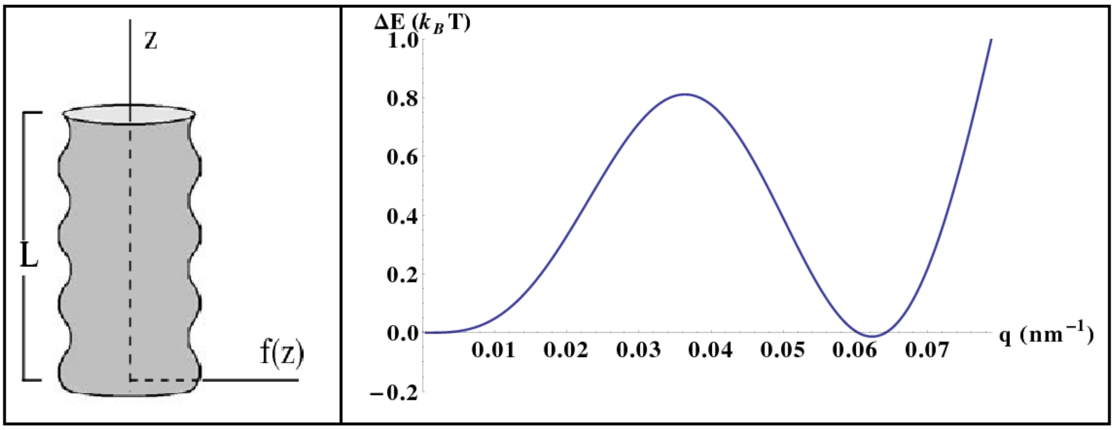

FIGURE E.1: Left: Schematic denoting notation used. Right: Difference in energy between the perturbed and unperturbed cylinder as a function of wavenumber q for $\sigma R_o^2/\kappa = 2.67$, $L/R = 10$, and $a = 0.16\ nm$.

To understand how the pearling instability comes about as surface tension increases, we model the tubular invagination as a cylinder with a surface of revolution along the z axis given in a parametric form

$$\vec{r} = \left(f\left(z\right)\cos\varphi, f\left(z\right)\sin\varphi, z\right), \tag{E.1}$$

where $f\left(z\right)$ has the form

$$f\left(z\right) = R\left(1 + \frac{a}{R}\zeta\left(z\right)\right), \tag{E.2}$$

where $\frac{a}{R} \ll 1$ and $\left|\zeta\left(z\right)\right| \sim 1$ with the assumption $\zeta\left(0\right) = \zeta\left(L\right) = 0$. See Fig. E.1a. The simplest possible form for ζ is

$$\zeta\left(z\right) = \sin\left(qz\right). \tag{E.3}$$

Moreover, to quantify the energy, the mean curvature of the surface of revolution [147] is

$$\begin{aligned} H\left(z\right) &= \frac{f(z)f''(z)-f'(z)^2-1}{2f(z)\left(f'(z)^2+1\right)^{3/2}} \\ &= \frac{-1-a^2q^2\cos(qz)^2-aq^2\sin(qz)(R+a\sin(qz))}{2\left(1+a^2q^2\cos(qz)^2\right)^{3/2}\left(R+a\sin(qz)\right)} \end{aligned} \tag{E.4}$$

In this parameterization, the energy of the cylindrical membrane is given as

$$\begin{aligned} E &= \int dS\left(2\kappa H^2+\sigma\right) \\ &= \int d\varphi dz f\left(z\right)\left(1+f'\left(z\right)^2\right)^{1/2}\left(2\kappa H^2+\sigma\right). \end{aligned} \tag{E.5}$$

This expands to

$$\begin{aligned} E = \int d\varphi dz R\left(1+\frac{a}{R}\zeta\left(z\right)\right)\left(1+a^2\zeta'\left(z\right)^2\right)^{1/2}\left(2\kappa H^2+\sigma\right) \\ = \int_0^L 2\pi\sqrt{1+a^2q^2\cos(qz)^2}(R+a\sin(qz))\big(\sigma \\ +\frac{\kappa\left(1+a^2q^2\cos(qz)^2+aq^2\sin(qz)(R+a\sin(qz))\right)^2}{2\left(1+a^2q^2\cos(qz)^2\right)^3\left(R+a\sin(qz)\right)^2}\big)dz. \end{aligned} \tag{E.6}$$

We will now impose a volume constraint as with all minimal surface problems, otherwise, once the surface tension term dominates, no surface will be the lowest energy solution. This volume constaint is given by

$$V = \int_0^L \pi\left(R+a\sin\left(qz\right)\right)^2 dz = \pi R_o^2 L, \tag{E.7}$$

where R_o is the original cylinder's radius. Using this constraint, we can solve for R and then compare the energies of the original unperturbed cylinder with the perturbed cylinder, where the former energy, E_0, is given by

$$\begin{aligned} E_0 = E(a=0) &= \int_0^L 2\pi R_o\left(\frac{\kappa}{2R_o^2}+\sigma\right)dz \\ &= 2\pi R_o L\left(\frac{\kappa}{2R_o^2}+\sigma\right). \end{aligned} \tag{E.8}$$

Using *Mathematica* [148], we find that when $\kappa = 10\ k_BT$, $\sigma = 0.32\ k_BT/nm^2$, $R_o = 8.71\ nm$, $L = 87.1\ nm$—all relevant parameters for the problem at hand—and $a = 0.16\ nm$, the energy difference $\Delta E = E_{pert} - E_0$ becomes negative near $q \approx 0.06\ nm^{-1}$ (See Fig. E.1b). For a cylinder of order 100 nm, this instability can lead to pinch-off. We must point out that for $\sigma R_o^2/\kappa > 1.6$, there is an instability at much smaller q, or much longer cylinders [149], such that this instability would not be relevant for endocytosis in yeast. For the relevant range of wavevectors, for $\sigma R_o^2/\kappa < 2.39$, the smooth cylinder is stable. Therefore, the ratio $\sigma R_o^2/\kappa$ needs to be large enough for the pearling instability to set in for endocytosis in yeast since surface tension favors spheres as opposed to cylinders. In other words, once the surface tension becomes large enough, the pearling instability sets in.

Bibliography

[1] Peter B Canham. The minimum energy of bending as a possible explanation of the biconcave shape of the human red blood cell. *Journal of Theoretical Biology*, 26(1):61–81, 1970.

[2] SA Safran. Statistical thermodynamics of surfaces, interfaces, and membranes (boulder, co, 2003.

[3] Wolfgang Helfrich. Elastic properties of lipid bilayers: theory and possible experiments. *Zeitschrift für Naturforschung C*, 28(11-12):693–703, 1973.

[4] Harvey Lodish. *Molecular cell biology*. Macmillan, 2008.

[5] Harvey T McMahon and Emmanuel Boucrot. Molecular mechanism and physiological functions of clathrin-mediated endocytosis. *Nature reviews Molecular cell biology*, 12(8):517–533, 2011.

[6] David Perrais and Christien J Merrifield. Dynamics of endocytic vesicle creation. *Developmental cell*, 9(5):581–592, 2005.

[7] Douglas R Boettner, Richard J Chi, and Sandra K Lemmon. Lessons from yeast for clathrin-mediated endocytosis. *Nature cell biology*, 14(1):2–10, 2012.

[8] Thomas D Pollard. Rate constants for the reactions of atp-and adp-actin with the ends of actin filaments. *The Journal of cell biology*, 103(6):2747–2754, 1986.

[9] Bruce Alberts, Alexander Johnson, Julian Lewis, Martin Raff, Keith Roberts, Peter Walter, et al. Cell junctions, cell adhesion, and the extracellular matrix. 2002.

[10] Fred C MacKintosh et al. *Soft condensed matter physics in molecular and cell biology*. CRC Press, 2006.

[11] Arshad Desai and Timothy J Mitchison. Microtubule polymerization dynamics. *Annual review of cell and developmental biology*, 13(1):83–117, 1997.

[12] Manuel L Cano, Douglas A Lauffenburger, and Sally H Zigmond. Kinetic analysis of f-actin depolymerization in polymorphonuclear leukocyte lysates indicates that chemoattractant stimulation increases actin filament number without altering the filament length distribution. *The Journal of cell biology*, 115(3):677–687, 1991.

[13] N Mücke, L Kreplak, R Kirmse, T Wedig, H Herrmann, U Aebi, and J Langowski. Assessing the flexibility of intermediate filaments by atomic force microscopy. *Journal of molecular biology*, 335(5):1241–1250, 2004.

[14] Toshiro Oda, Heiko Stegmann, Rasmus R Schröder, Keiichi Namba, and Yuichiro Maéda. Modeling of the f-actin structure. In *Regulatory Mechanisms of Striated Muscle Contraction*, pages 385–401. Springer, 2007.

[15] Shechao Feng and Pabitra N Sen. Percolation on elastic networks: new exponent and threshold. *Physical review letters*, 52(3):216, 1984.

[16] J Clerk Maxwell. L. on the calculation of the equilibrium and stiffness of frames. *The London, Edinburgh, and Dublin Philosophical Magazine and Journal of Science*, 27(182):294–299, 1864.

[17] DJ Jacobs and MF Thorpe. Generic rigidity percolation in two dimensions. *Physical Review E*, 53(4):3682, 1996.

[18] Shechao Feng, MF Thorpe, and E Garboczi. Effective-medium theory of percolation on central-force elastic networks. *Physical Review B*, 31(1):276, 1985.

[19] Lawrence M Schwartz, Shechao Feng, MF Thorpe, and Pabitra N Sen. Behavior of depleted elastic networks: Comparison of effective-medium and numerical calculations. *Physical Review B*, 32(7):4607, 1985.

[20] Moumita Das, DA Quint, and JM Schwarz. Redundancy and cooperativity in the mechanics of compositely crosslinked filamentous networks. *PloS one*, 7(5), 2012.

[21] Revathi Ananthakrishnan and Allen Ehrlicher. The forces behind cell movement. *International journal of biological sciences*, 3(5):303, 2007.

[22] Tatyana M Svitkina and Gary G Borisy. Arp2/3 complex and actin depolymerizing factor/cofilin in dendritic organization and treadmilling of actin filament array in lamellipodia. *The Journal of cell biology*, 145(5):1009–1026, 1999.

[23] Harvey F Lodish, Arnold Berk, S Lawrence Zipursky, Paul Matsudaira, David Baltimore, James Darnell, et al. *Molecular cell biology*, volume 4. Citeseer, 2000.

[24] Thomas E Schaus, Edwin W Taylor, and Gary G Borisy. Self-organization of actin filament orientation in the dendritic-nucleation/array-treadmilling model. *Proceedings of the National Academy of Sciences*, 104(17):7086–7091, 2007.

[25] David Razafsky and Didier Hodzic. Bringing kash under the sun: the many faces of nucleo-cytoskeletal connections. *The Journal of cell biology*, 186(4):461–472, 2009.

[26] Andrew J Maniotis, Christopher S Chen, and Donald E Ingber. Demonstration of mechanical connections between integrins, cytoskeletal filaments, and nucleoplasm that stabilize nuclear structure. *Proceedings of the National Academy of Sciences*, 94(3):849–854, 1997.

[27] Melissa Crisp, Qian Liu, Kyle Roux, JB Rattner, Catherine Shanahan, Brian Burke, Phillip D Stahl, and Didier Hodzic. Coupling of the nucleus and cytoplasm role of the linc complex. *The Journal of cell biology*, 172(1):41–53, 2006.

[28] Bruce Alberts, Alexander Johnson, Julian Lewis, Martin Raff, Keith Roberts, Peter Walter, et al. The cytoskeleton and cell behavior. 2002.

[29] John P Sadowski, Colby R Calvert, David Yu Zhang, Niles A Pierce, and Peng Yin. Developmental self-assembly of a dna tetrahedron. *ACS Nano*, 8(4):3251–3259, 2014.

[30] Shivendra Pandey, Margaret Ewing, Andrew Kunas, Nghi Nguyen, David H Gracias, and Govind Menon. Algorithmic design of self-folding polyhedra. *PNAS*, 108 (50):19885–19890, 2011.

[31] S Felton, M Tolley, E Demaine, D Rus, and R Wood. A method for building self-folding machines. *Science*, 345(6197):644–646, 2014.

[32] Gabriel Villar, Alexander D. Graham, and Hagan Bayley. A tissue-like printed material. *Science*, 340(6128):48–52, 2013.

[33] P. Poulin and J. Bibette. Adhesion of water droplets in organic solvent. *Langmuir*, 14(22):6341–6343, 1998.

[34] Kei Funakoshi, Hiroaki Suzuki, and Shoji Takeuchi. Lipid bilayer formation by contacting monolayers in a microfluidic device for membrane protein analysis. *Anal. Chem.*, 78(24):8169–8174, 2006.

[35] Noah Malmstadt, Michael A. Nash, Robert F. Purnell, and Jacob J. Schmidt. Automated formation of lipid-bilayer membranes in a microfluidic device. *Nano Lett.*, 6(9):1961–1965, 2006.

[36] Matthew A. Holden, David Needham, and Hagan Bayley. Functional bionetworks from nanoliter water droplets. *J. Am. Chem. Soc.*, 129(27):8650–8655, 2007.

[37] David R Nelson. Toward a tetravalent chemistry of colloids. *Nano Lett.*, 2(10): 1125–1129, 2002.

[38] Sharon C Glotzer and Michael J Solomon. Anisotropy of building blocks and their assembly into complex structures. *Nat. Mater.*, 6(8):557–562, 2007.

[39] Wanda Kukulski, Martin Schorb, Marko Kaksonen, and John AG Briggs. Plasma membrane reshaping during endocytosis is revealed by time-resolved electron tomography. *Cell*, 150(3):508–520, 2012.

[40] Marko Kaksonen, Yidi Sun, and David G Drubin. A pathway for association of receptors, adaptors, and actin during endocytic internalization. *Cell*, 115(4): 475–487, 2003.

[41] Marcus J Taylor, David Perrais, and Christien J Merrifield. A high precision survey of the molecular dynamics of mammalian clathrin-mediated endocytosis. *PLoS-Biology*, 9(3):581, 2011.

[42] Jian Liu, Marko Kaksonen, David G Drubin, and George Oster. Endocytic vesicle scission by lipid phase boundary forces. *Proceedings of the National Academy of Sciences*, 103(27):10277–10282, 2006.

[43] Agnieszka Collins, Anthony Warrington, Kenneth A Taylor, and Tatyana Svitkina. Structural organization of the actin cytoskeleton at sites of clathrin-mediated endocytosis. *Current Biology*, 21(14):1167–1175, 2011.

[44] Rajesh Arasada and Thomas D Pollard. Distinct roles for f-bar proteins cdc15p and bzz1p in actin polymerization at sites of endocytosis in fission yeast. *Current Biology*, 21(17):1450–1459, 2011.

[45] Olivia L Mooren, Brian J Galletta, and John A Cooper. Roles for actin assembly in endocytosis. *Annual review of biochemistry*, 81:661–686, 2012.

[46] Marko Kaksonen, Christopher P Toret, and David G Drubin. Harnessing actin dynamics for clathrin-mediated endocytosis. *Nature reviews Molecular cell biology*, 7(6):404–414, 2006.

[47] Jennifer J Baggett and Beverly Wendland. Clathrin function in yeast endocytosis. *Traffic*, 2(5):297–302, 2001.

[48] John C Dawson, John A Legg, and Laura M Machesky. Bar domain proteins: a role in tubulation, scission and actin assembly in clathrin-mediated endocytosis. *Trends in cell biology*, 16(10):493–498, 2006.

[49] T Kirchhausen, SC Harrison, and J Heuser. Configuration of clathrin trimers: evidence from electron microscopy. *Journal of ultrastructure and molecular structure research*, 94(3):199–208, 1986.

[50] Amanda Reider and Beverly Wendland. Endocytic adaptors–social networking at the plasma membrane. *Journal of cell science*, 124(10):1613–1622, 2011.

[51] Jian Liu, Yidi Sun, David G Drubin, and George F Oster. The mechanochemistry of endocytosis. *PLoS biology*, 7(9):2063, 2009.

[52] Anders E Carlsson and Philip V Bayly. Force generation by endocytic actin patches in budding yeast. *Biophysical journal*, 106(8):1596–1606, 2014.

[53] Soheil Aghamohammadzadeh and Kathryn R Ayscough. Differential requirements for actin during yeast and mammalian endocytosis. *Nature cell biology*, 11(8): 1039–1042, 2009.

[54] David Boal and David H Boal. *Mechanics of the Cell*. Cambridge University Press, 2012.

[55] Vladimir Sirotkin, Julien Berro, Keely Macmillan, Lindsey Zhao, and Thomas D Pollard. Quantitative analysis of the mechanism of endocytic actin patch assembly and disassembly in fission yeast. *Molecular biology of the cell*, 21(16):2894–2904, 2010.

[56] Julien Berro, Vladimir Sirotkin, and Thomas D Pollard. Mathematical modeling of endocytic actin patch kinetics in fission yeast: disassembly requires release of actin filament fragments. *Molecular biology of the cell*, 21(16):2905–2915, 2010.

[57] James B Moseley and Bruce L Goode. The yeast actin cytoskeleton: from cellular function to biochemical mechanism. *Microbiology and Molecular Biology Reviews*, 70(3):605–645, 2006.

[58] Benoît Sorre, Andrew Callan-Jones, John Manzi, Bruno Goud, Jacques Prost, Patricia Bassereau, and Aurélien Roux. Nature of curvature coupling of amphiphysin with membranes depends on its bound density. *Proceedings of the National Academy of Sciences*, 109(1):173–178, 2012.

[59] Rui Zhang and Frank LH Brown. Cytoskeleton mediated effective elastic properties of model red blood cell membranes. *The Journal of chemical physics*, 129(6): 065101, 2008.

[60] G Gompper and DM Kroll. Triangulated-surface models of fluctuating membranes. *Statistical Mechanics of Membranes and Surfaces*, 2, 2004.

[61] Kenneth A Brakke. The surface evolver. *Experimental mathematics*, 1(2):141–165, 1992.

[62] Vo A Kazakov, IK Kostov, and AA Migdal. Critical properties of randomly triangulated planar random surfaces. *Physics Letters B*, 157(4):295–300, 1985.

[63] A Billoire and F David. Scaling properties of randomly triangulated planar random surfaces: a numerical study. *Nuclear Physics B*, 275(4):617–640, 1986.

[64] G Gompper and DM Kroll. Statistical mechanics of membranes: freezing, undulations, and topology fluctuations. *Journal of Physics: Condensed Matter*, 12(8A): A29, 2000.

[65] T Kohyama, DM Kroll, and G Gompper. Budding of crystalline domains in fluid membranes. *Physical Review E*, 68(6):061905, 2003.

[66] Neeraj J Agrawal, Jonathan Nukpezah, and Ravi Radhakrishnan. Minimal mesoscale model for protein-mediated vesiculation in clathrin-dependent endocytosis. *PLoS Comput. Biol*, 6(9):e1000926, 2010.

[67] Marijn GJ Ford, Ian G Mills, Brian J Peter, Yvonne Vallis, Gerrit JK Praefcke, Philip R Evans, and Harvey T McMahon. Curvature of clathrin-coated pits driven by epsin. *Nature*, 419(6905):361–366, 2002.

[68] David P Siegel and MM Kozlov. The gaussian curvature elastic modulus of n-monomethylated dioleoylphosphatidylethanolamine: relevance to membrane fusion and lipid phase behavior. *Biophysical journal*, 87(1):366–374, 2004.

[69] Aurélien Roux, Damien Cuvelier, Pierre Nassoy, Jacques Prost, Patricia Bassereau, and Bruno Goud. Role of curvature and phase transition in lipid sorting and fission of membrane tubules. *The EMBO Journal*, 24(8):1537–1545, 2005.

[70] Tobias Baumgart, Samuel T Hess, and Watt W Webb. Imaging coexisting fluid domains in biomembrane models coupling curvature and line tension. *Nature*, 425 (6960):821–824, 2003.

[71] J-M Allain, Cornelis Storm, Aurelien Roux, M Ben Amar, and J-F Joanny. Fission of a multiphase membrane tube. *Physical review letters*, 93(15):158104, 2004.

[72] Tristan S Ursell, William S Klug, and Rob Phillips. Morphology and interaction between lipid domains. *Proceedings of the National Academy of Sciences*, 106(32): 13301–13306, 2009.

[73] WT Góźdź and G Gompper. Shape transformations of two-component membranes under weak tension. *EPL (Europhysics Letters)*, 55(4):587, 2001.

[74] Markus J Tamás, Kattie Luyten, F Chris W Sutherland, Agustin Hernandez, Jacobus Albertyn, Hadi Valadi, Hong Li, Bernard A Prior, Stephanus G Kilian, José Ramos, et al. Fps1p controls the accumulation and release of the compatible solute glycerol in yeast osmoregulation. *Molecular microbiology*, 31(4):1087–1104, 1999.

[75] David R Kovar and Thomas D Pollard. Insertional assembly of actin filament barbed ends in association with formins produces piconewton forces. *Proceedings of the National Academy of Sciences of the United States of America*, 101(41): 14725–14730, 2004.

[76] Evan Evans, Volkmar Heinrich, Florian Ludwig, and Wieslawa Rawicz. Dynamic tension spectroscopy and strength of biomembranes. *Biophysical journal*, 85(4): 2342–2350, 2003.

[77] Imre Derényi, Frank Jülicher, and Jacques Prost. Formation and interaction of membrane tubes. *Physical review letters*, 88(23):238101, 2002.

[78] Gerbrand Koster, Angelo Cacciuto, Imre Derényi, Daan Frenkel, and Marileen Dogterom. Force barriers for membrane tube formation. *Physical review letters*, 94(6):068101, 2005.

[79] G Gompper and DM Kroll. Driven transport of fluid vesicles through narrow pores. *Physical Review E*, 52(4):4198, 1995.

[80] Roshni Basu, Emilia Laura Munteanu, and Fred Chang. Role of turgor pressure in endocytosis in fission yeast. *Molecular biology of the cell*, 25(5):679–687, 2014.

[81] Yidi Sun, Adam C Martin, and David G Drubin. Endocytic internalization in budding yeast requires coordinated actin nucleation and myosin motor activity. *Developmental cell*, 11(1):33–46, 2006.

[82] JE Molloy, JE Burns, J Kendrick-Jones, RT Tregear, and DCS White. Movement and force produced by a single myosin head. *Nature*, 378(6553):209–212, 1995.

[83] Alex Mogilner and George Oster. Force generation by actin polymerization ii: the elastic ratchet and tethered filaments. *Biophysical journal*, 84(3):1591–1605, 2003.

[84] Laurent Blanchoin, Kurt J Amann, Henry N Higgs, Jean-Baptiste Marchand, Donald A Kaiser, and Thomas D Pollard. Direct observation of dendritic actin filament networks nucleated by arp2/3 complex and wasp/scar proteins. *Nature*, 404(6781):1007–1011, 2000.

[85] Roy Bar-Ziv and Elisha Moses. Instability and" pearling" states produced in tubular membranes by competition of curvature and tension. *Physical review letters*, 73(10):1392, 1994.

[86] Philip Nelson, Thomas Powers, and Udo Seifert. Dynamical theory of the pearling instability in cylindrical vesicles. *Physical review letters*, 74(17):3384, 1995.

[87] Roy Bar-Ziv, Tsvi Tlusty, Elisha Moses, Samuel A Safran, and Alexander Bershadsky. Pearling in cells: a clue to understanding cell shape. *Proceedings of the National Academy of Sciences*, 96(18):10140–10145, 1999.

[88] E Evans and W Rawicz. Entropy-driven tension and bending elasticity in condensed-fluid membranes. *Physical Review Letters*, 64(17):2094, 1990.

[89] Ilan Tsafrir, Dror Sagi, Tamar Arzi, Marie-Alice Guedeau-Boudeville, Vidar Frette, Daniel Kandel, and Joel Stavans. Pearling instabilities of membrane tubes with anchored polymers. *Physical review letters*, 86(6):1138, 2001.

[90] Rahul Chadda, Mark T Howes, Sarah J Plowman, John F Hancock, Robert G Parton, and Satyajit Mayor. Cholesterol-sensitive cdc42 activation regulates actin polymerization for endocytosis via the geec pathway. *Traffic*, 8(6):702–717, 2007.

[91] Philip N Dannhauser and Ernst J Ungewickell. Reconstitution of clathrin-coated bud and vesicle formation with minimal components. *Nature cell biology*, 14(6): 634–639, 2012.

[92] Robert J Mashl and Robijn F Bruinsma. Spontaneous-curvature theory of clathrin-coated membranes. *Biophysical journal*, 74(6):2862–2875, 1998.

[93] Sean X Sun and Denis Wirtz. Mechanics of enveloped virus entry into host cells. *Biophysical journal*, 90(1):L10–L12, 2006.

[94] Pierre-Gilles De Gennes. On a relation between percolation theory and the elasticity of gels. *Journal de Physique Lettres*, 37(1):1–2, 1976.

[95] Donald J Jacobs and Michael F Thorpe. Generic rigidity percolation: the pebble game. *Physical review letters*, 75(22):4051, 1995.

[96] C Moukarzel and Phillip M Duxbury. Stressed backbone and elasticity of random central-force systems. *Physical review letters*, 75(22):4055, 1995.

[97] MF Thorpe and Y Cai. Mechanical and vibrational properties of network structures. *Journal of Non-Crystalline Solids*, 114:19–24, 1989.

[98] Eugene M Terentjev. Liquid-crystalline elastomers. *Journal of Physics: Condensed Matter*, 11(24):R239, 1999.

[99] Paul Dalhaimer, Dennis E Discher, and Tom C Lubensky. Crosslinked actin networks show liquid crystal elastomer behaviour, including soft-mode elasticity. *Nature Physics*, 3(5):354–360, 2007.

[100] Junfei Geng, G Reydellet, Éric Clément, and RP Behringer. Greens function measurements of force transmission in 2d granular materials. *Physica D: Nonlinear Phenomena*, 182(3):274–303, 2003.

[101] C Goldenberg and I Goldhirsch. Force chains, microelasticity, and macroelasticity. *Physical review letters*, 89(8):084302, 2002.

[102] Matthias Otto, J-P Bouchaud, Philippe Claudin, and Joshua ES Socolar. Anisotropy in granular media: Classical elasticity and directed-force chain network. *Physical Review E*, 67(3):031302, 2003.

[103] Tatyana M Svitkina and Gary G Borisy. Arp2/3 complex and actin depolymerizing factor/cofilin in dendritic organization and treadmilling of actin filament array in lamellipodia. *The Journal of cell biology*, 145(5):1009–1026, 1999.

[104] Laurent Blanchoin, Kurt J Amann, Henry N Higgs, Jean-Baptiste Marchand, Donald A Kaiser, and Thomas D Pollard. Direct observation of dendritic actin filament networks nucleated by arp2/3 complex and wasp/scar proteins. *Nature*, 404(6781):1007–1011, 2000.

[105] S Roux and A Hansen. Critical behaviour of anisotropic'superelastic'central-force percolation. *Journal of Physics A: Mathematical and General*, 20(13):L879, 1987.

[106] J Wang and A Brooks Harris. Splay rigidity in the anisotropic superelastic network. *EPL (Europhysics Letters)*, 6(2):157, 1988.

[107] Jian Wang and A Brooks Harris. Central-force models which exhibit a splay-rigid phase. *Physical Review B*, 40(10):7256, 1989.

[108] Shlomo Alexander. Amorphous solids: their structure, lattice dynamics and elasticity. *Physics reports*, 296(2):65–236, 1998.

[109] EJ Garboczi and MF Thorpe. Effective-medium theory of percolation on central-force elastic networks. ii. further results. *Physical Review B*, 31(11):7276, 1985.

[110] William H Press, Saul A Teukolsky, William T Vetterling, and Brian P Flannery. Numerical recipes in c: the art of scientific computing. *Cambridge University Press, Cambridge, MA,*, 131:243–262, 1992.

[111] Martin Ostoja-Starzewski. Lattice models in micromechanics. *Applied Mechanics Reviews*, 55(1):35–60, 2002.

[112] F Behroozi. Theory of elasticity in two dimensions and its application to langmuir-blodgett films. *Langmuir*, 12(9):2289–2291, 1996.

[113] Scott Kirkpatrick. Percolation and conduction. *Reviews of modern physics*, 45(4): 574, 1973.

[114] Xiaoming Mao, Ning Xu, and TC Lubensky. Soft modes and elasticity of nearly isostatic lattices: Randomness and dissipation. *Physical review letters*, 104(8): 085504, 2010.

[115] Wouter G Ellenbroek and Xiaoming Mao. Rigidity percolation on the square lattice. *EPL (Europhysics Letters)*, 96(5):54002, 2011.

[116] Claus Heussinger and Erwin Frey. Stiff polymers, foams, and fiber networks. *Physical review letters*, 96(1):017802, 2006.

[117] Moumita Das, FC MacKintosh, and Alex J Levine. Effective medium theory of semiflexible filamentous networks. *Physical review letters*, 99(3):038101, 2007.

[118] Chase P Broedersz, Xiaoming Mao, Tom C Lubensky, and Frederick C MacKintosh. Criticality and isostaticity in fibre networks. *Nature Physics*, 7(12):983–988, 2011.

[119] Xiaoming Mao, Olaf Stenull, and Thomas C Lubensky. Effective-medium theory of a filamentous triangular lattice. *Physical Review E*, 87(4):042601, 2013.

[120] Haye Hinrichsen. Non-equilibrium critical phenomena and phase transitions into absorbing states. *Advances in physics*, 49(7):815–958, 2000.

[121] Andrew R Missel, Mo Bai, William S Klug, and Alex J Levine. Affine-nonaffine transition in networks of nematically ordered semiflexible polymers. *Physical Review E*, 82(4):041907, 2010.

[122] Martin Kiemes, Panayotis Benetatos, and Annette Zippelius. Orientational order and glassy states in networks of semiflexible polymers. *Physical Review E*, 83(2): 021905, 2011.

[123] David A Head and Daisuke Mizuno. Local mechanical response in semiflexible polymer networks subjected to an axisymmetric prestress. *Physical Review E*, 88 (2):022717, 2013.

[124] Adam J Engler, Shamik Sen, H Lee Sweeney, and Dennis E Discher. Matrix elasticity directs stem cell lineage specification. *Cell*, 126(4):677–689, 2006.

[125] Kristopher A Kilian, Branimir Bugarija, Bruce T Lahn, and Milan Mrksich. Geometric cues for directing the differentiation of mesenchymal stem cells. *Proceedings of the National Academy of Sciences*, 107(11):4872–4877, 2010.

[126] Marie Versaevel, Thomas Grevesse, Maryam Riaz, Joséphine Lantoine, and Sylvain Gabriele. Micropatterning hydroxy-paam hydrogels and sylgard 184 silicone elastomers with tunable elastic moduli. *Methods in cell biology*, 121:33–48, 2013.

[127] Jop Kind and Bas van Steensel. Genome–nuclear lamina interactions and gene regulation. *Current opinion in cell biology*, 22(3):320–325, 2010.

[128] Maria L Lombardi, Diana E Jaalouk, Catherine M Shanahan, Brian Burke, Kyle J Roux, and Jan Lammerding. The interaction between nesprins and sun proteins at the nuclear envelope is critical for force transmission between the nucleus and cytoskeleton. *Journal of Biological Chemistry*, 286(30):26743–26753, 2011.

[129] Philipp Isermann and Jan Lammerding. Nuclear mechanics and mechanotransduction in health and disease. *Current Biology*, 23(24):R1113–R1121, 2013.

[130] Yeh-Chuin Poh, Sergey P Shevtsov, Farhan Chowdhury, Douglas C Wu, Sungsoo Na, Miroslav Dundr, and Ning Wang. Dynamic force-induced direct dissociation of protein complexes in a nuclear body in living cells. *Nature communications*, 3: 866, 2012.

[131] M Wyart, H Liang, A Kabla, and L Mahadevan. Elasticity of floppy and stiff random networks. *Physical review letters*, 101(21):215501, 2008.

[132] Jun Young Chung, Hunter King, and L. Mahadevan. Evaporative microclimate driven hygrometers and hygromotors. *Europhys. Lett.*, 107(64002):1–6, 2014.

[133] Xi Chen, L. Mahadevan, Adam Driks, and Ozgur Sahin. Bacillus spores as building blocks for stimuli-responsive materials and nanogenerators. *Nat. Nanotechnol.*, 9: 137–141, 2014.

[134] Edoardo Sinibaldi, Alfredo Argiolas, Gian Luigi Puleo, and Barbara Mazzolai. Another lesson from plants: The forward osmosis-based actuator. *PLoS ONE*, 9 (7):e102461, 2014.

[135] C.B. Biezeno. Survey of papers on elasticity published in holland 19401946. *Adv. Appl. Mech.*, 1:105 – 170, 1948.

[136] William Humphrey, Andrew Dalke, and Klaus Schulten. VMD – Visual Molecular Dynamics. *J. Mol. Graphics*, 14:33–38, 1996.

[137] John Stone. Master's thesis, Computer Science Department, University of Missouri-Rolla, April 1998.

[138] Thomas W. Lion and Rosalind J. Allen. Osmosis with active solutes. *Europhys. Lett.*, 106(3):34003, 2014.

[139] Ramin Golestanian, Tanniemola B Liverpool, and Armand Ajdari. Propulsion of a molecular machine by asymmetric distribution of reaction products. *Phys. Rev. Lett.*, 94(22):220801, 2005.

[140] Jonathan R Howse, Richard AL Jones, Anthony J Ryan, Tim Gough, Reza Vafabakhsh, and Ramin Golestanian. Self-motile colloidal particles: from directed propulsion to random walk. *Phys. Rev. Lett.*, 99(4):048102, 2007.

[141] R Golestanian, TB Liverpool, and A Ajdari. Designing phoretic micro-and nano-swimmers. *New J. Phys.*, 9(5):126, 2007.

[142] Francesco Sciortino, Achille Giacometti, and Giorgio Pastore. Phase diagram of janus particles. *Phys. Rev. Lett.*, 103(23):237801, 2009.

[143] Romy Radunz, Daniel Rings, Klaus Kroy, and Frank Cichos. Hot brownian particles and photothermal correlation spectroscopy. *J. Phys. Chem. A*, 113(9):1674–1677, 2009.

[144] Laurent Joly, Samy Merabia, and J-L Barrat. Effective temperatures of a heated brownian particle. *Europhys. Lett.*, 94(5):50007, 2011.

[145] Runar Heggelien Refsns. A brief introduction to the conjugate gradient method. 1999.

[146] Nicholas Metropolis, Arianna W Rosenbluth, Marshall N Rosenbluth, Augusta H Teller, and Edward Teller. Equation of state calculations by fast computing machines. *The journal of chemical physics*, 21(6):1087–1092, 1953.

[147] Ross Raymond Middlemiss, John L Marks, and James R Smart. *Analytic geometry.* McGraw-Hill Companies, 1968.

[148] Mathematica Version. 8.0, wolfram research. *Inc., Champaign, IL*, 2010.

[149] TT Nguyen, A Gopal, KYC Lee, and TA Witten. Surface charge relaxation and the pearling instability of charged surfactant tubes. *Physical Review E*, 72(5): 051930, 2005.

VITA

Personal Information

Name of author: Tao Zhang

Place of birth: Anqing, Anhui, China

Date of birth: September 25, 1988

E-mail: tzhang13@syr.edu

Webpage: http://taozhang.info/

Mobile Phone: (315) 278-2871

Education

09/2010 – Present	**Syracuse University**
	Ph.D. candidate in Physics
09/2006 – 06/2010	**University of Science and Technology of China**
	B.S. in Physics

Employment

09/2010 – Present	**Syracuse University**
	Research Assistant: working with Prof. Jennifer Schwarz and Prof. Mark Bowick
	Teaching: undergraduate laboratory/recitation courses

Publications

T. Zhang, R. Sknepnek, M. J. Bowick, and J. M. Schwarz, "On the modeling of endocytosis in yeast", Biophys. J. 108:508-519 (2015)

T. Zhang, J. M. Schwarz, and Moumita Das, "Mechanics of anisotropic spring networks", Phys. Rev. E. 90, 062139 (2014)

T. Zhang, Duanduan Wan, J. M. Schwarz, and M. J. Bowick, "Shape-shifting droplet networks", arXiv: 1505.01108

Manuscripts in Preparation:

- T. Zhang and J. M. Schwarz, "Coupled biopolymer networks"

Awards

New York Complex Matter Workshop 2014 - “*Best Sound Bite Prize*”

Contributed Talks

APS March Meeting 2014	Tube formation in fluid membranes
	(Session L18: Vesicles and Membranes)
APS March Meeting 2013	On the modeling of endocytosis
	(Session N31: Membrane and Membrane Protein Interactions)
APS March Meeting 2012	The mechanics of anisotropic cytoskeletal networks
	(Session Z40: Biomechanics – Organismic Motion)